# Structural characterization of primary cilia using accelerated piezoelectrically driven STED nanoscopy

Bhavik Nathwani

Submitted in partial fulfillment of the
requirements for the degree
of Doctor of Philosophy
in the Graduate School of Arts and Sciences

COLUMBIA UNIVERSITY

2012

# Abstract

Structural characterization of primary cilia using accelerated piezoelectrically driven STED nanoscopy

Bhavik Nathwani

Primary cilia are non-motile, hair-like projections occurring on most mammalian cell types. They play essential roles in transduction of chemical and mechanical signals across the cell membrane. For example, primary cilia are able to transduce sonic hedgehog signals, necessary in embryonic development and adult stem cell functions. Recent work on primary cilia has demonstrated correlations between primary cilia morphology and its ability to sense/transduce signals. Several such studies have underscored the need for detailed study of morphology of primary cilia and structure-function mapping of its morphology with its ability to transduce signals. However, the size scale of the primary cilium makes it very challenging to extract biologically relevant morphometric features using conventional imaging techniques. The molecular architecture of the primary cilium is beyond the resolvability of conventional diffraction limited optical imaging techniques. Data from non-optical tools such as electron microscopy have been limited by the need for dehydration during sample prep. Advent of superresolution optical imaging approaches has only recently made it possible to probe primary cilia morphologically to study its structure in physiologically interesting environments.

Signaling pathways regulated by primary cilia are critical to embryo development and organogenesis. Therefore, it would be interesting to study primary cilia both in somatic (adult) cells while simultaneously comparing and

contrasting it with their occurrence on stem cells. Human induced pluripotent stem cell (hiPSC) reprogramming possesses enormous potential in stem cell research and disease modeling. Chemical and mechanical signaling has been implicated in maintenance of pluripotency of hiPSCs and their differentiation pathways toward various lineages, where primary cilia have been shown to play a critical role in mechano-chemical signaling across a wide spectrum of cell types. The functions of primary cilia in hiPSCs and their characteristic changes during the reprogramming process remain largely vague.

Therefore, in order to study primary cilia morphology on both somatic cells as well as hiPSCs, we developed a superresolution nanoscopy system using the stimulated emission depletion (STED) technique with novel accelerated piezoelectric control (apSTED). This improved STED system achieved a reduction in photobleaching rates from ~80% to ~10% while maintaining superresolution, ~50 nm at the focal plane for biological samples.

Subsequently, we focused on conducting comparative morphometric studies of primary cilia found on somatic cells and hiPSCs. Our work was the first to systematically demonstrate the existence of primary cilia on hiPSCs. Using quantitative PCR assays, we demonstrated high levels of expression of primary cilia signaling partners, such as Patched1, Smoothened, and members of Gli family. Comparative morphometric analysis revealed that the mean length of reprogrammed cells was shorter than those of parental human fibroblasts. Morphometric analyses revealed that reprogramming resulted in an increase in curvature of primary cilia from ~0.015 $\mu m^{-1}$ to 0.064 $\mu m^{-1}$, indicating an underlying ~4-fold decrease in their rigidity, and a decrease in length of primary cilia from ~2.38 μm to ~1.45 μm. Furthermore, reprogramming resulted in fewer primary cilia displaying either kinked or punctated geometries.

Custom-built software scripts were developed to extract and analyze superresolution apSTED imaging data collected on fibroblast primary cilia. Using apSTED, we were able to measure local variations in primary cilia curvature. A review of confocal data revealed that such variations in curvature were either completely missed or were significantly underestimated. We also utilized our technique to study macromolecular complexes within transition zone; a structure found at the base of primary cilia that plays a significant role in ciliogenesis and in maintaining structural integrity of primary cilia. Our data provides the first visualization of two important transition zone members, Tctn-2 and Cep290. We were able to demonstrate structural detail heretofore impenetrable to conventional imaging techniques. Furthermore, quantification of spatial distribution of these molecules, ~160 nm for Tctn-2 and ~180 nm for Cep290, provides evidence to indicate the relative positioning of these molecules within the transition zone. These studies highlight the advantages of using apSTED to study primary cilia and provide tools that could enable the deciphering of the architecture of the transition zone in primary cilia.

# Table of Contents

## List of Figures:

# Acknowledgement

I would like to take this opportunity to express my gratitude for the contributions of all the individuals who played an important role in the completion of my dissertation. Undoubtedly, I owe the largest debt of gratitude to my advisor Professor Jung-Chi Liao for showing me the path to doing insightful science while developing techniques making it possible to study the most exciting questions at the forefront of those sciences. Like most other things in life, the process of technology development or conducting scientific studies was full of difficult moments but through it all, he remained supportive, encouraging, and above all patient. His single-minded focus on the problem at hand and zeal to achieve excellence in research will serve as a guiding roadmap for me to chart my future scientific course. I would like to also thank Professor Gerard Ateshian for serving as the chair of my PhD thesis committee. Professor Ateshian's eye for detail, his meticulousness, will go with me at all my future endeavors. I would like to thank Professor James Hone for serving on my committee. The positive energy and can-do attitude that he radiated was greatly inspirational in bringing this work to fruition. I would like to gratefully acknowledge the roles of Professor Christopher Jacobs and Professor Kristin Myers for serving on my committee. Professor Jacobs provided the many resources and the primary cilia background on which the edifice of this work rests. Professor Myers drove home the message of the many advantages of utilizing engineering principles in elucidating vexing challenges in biology. Special thanks to Professor Rafael Yuste for his mentorship. He helped me with the transition from being a graduate student interested in myriad scientific topics to a scientist focused on answering a set of questions. A National Science Foundation Grant provided financial support for this work. Other funding sources included Nanoscale Science and Engineering Center (NSEC) at Columbia University and startup funds for the lab provided by Columbia University. I would like to express my gratitude towards Graduate School of Arts and Sciences at Columbia University for the award of *Interdisciplinary Science and Engineering Fellowship*. Furthermore, I am indebted to Sigma Xi for their award of a *Grant-in-aid-of-research*. The work would not have been possible without the generous support of all these agencies.

Special thanks to all my friends and colleagues at Columbia, including Tony Yang, Yuan Zhang, Christine Miller, Ed Bossange, Tucker Gillman, Perry Hampilos, Cindy Cai, Amy Lu, and all the other past and present members of the Liao lab. Not only were they extremely generous colleagues eager to help me out with scientific problems but also were very supportive and insightful in all administrative, social, and other non-scientific matters that arose during my tenure at Columbia. Robert Stark and Walter Khan at the machine shop helped me out with innumerable machining related situations. Office of mechanical engineering department at Columbia, Sandra Morris, Clarissa Marino, and Becca Chambers helped me with every administrative question that I ever had. My thanks to these individuals.

The limitations of my vocabulary prevent me from coherently expressing the debt of gratitude that I owe to my family; my parents, for instilling the thirst for knowledge that initiated me on the academic path, my wife and my brother for helping me make large strides on that path, and especially my son, whose arrival in this world precipitated the urgency of execution of this thesis project. I could not have asked for a more supportive and patient family, who stood by me during the highs and lows associated with this project. Many thanks.

# Abbreviations

| | |
|---|---|
| ACIII | Adenylyl Cyclase isoform III |
| STED | Stimulated Emission Depletion |
| IFT88 | Intraflagellar Transport protein 88 |
| Ac-Tub | Acetylated Tubulin |
| PBS | Phosphate Buffered Saline |
| Tctn2 | Tectin 2 |
| PBST | Phosphate Buffered Saline + Triton-X 100 |
| Hff1 | Human foreskin fibroblast cells |
| FBS | Fetal Bovine Serum |
| P/S | Penicillin-Streptomycin |
| PFA | Paraformaldehyde |
| iPSC | Induced Pluripotent Stem cells |
| hiPSC | Human Induced Pluripotent Stem cells |
| Shh | Sonic Hedgehog |
| Ac-Tub | Acetylated Tubulin |

# 1 Background and Motivation

## 1.1 Significance of primary cilia

Primary cilia are non-motile, solitary cellular projections playing essential mechanical and chemical sensory roles across a wide spectrum of cell types[1-3]. Primary cilia were first discovered in the year 1898[4]. For most of the previous century, they were considered vestigial[5]. However, recent studies have demonstrated that they serve as a central hub for the localization of receptors and signal transduction components that are involved in development, mechanotransduction, and stem cell functions[6]. For example, primary cilia are able to sense Sonic hedgehog (Shh) through Patched1 (Ptc1) localized at the cilia and accumulate Smoothened (Smo) leading to the activation of signaling[7]. This Shh signaling pathway is essential for embryonic development and adult stem cell functions[7,8]. Table 1 summarizes functions of primary cilia in a number of representative cell types.

Defective structures of primary cilia have been implicated in myriad disorders, broadly classified as 'ciliopathies'. Briefly, abnormalities in primary cilia development or function have been correlated with development of polycystic kidney disease (PKD)[9], Bardet-Biedl syndrome (BBS)[10], arthritis, osteoporosis[11], heart failure, cancer, and obesity[12]. Therefore, interest in studying primary cilia structure and in particular mapping the structure-function relationship has become a priority for the scientific community.

**Table 1. Primary cilia functions on different cell types**

| **Cell Type** | **Function** |
|---|---|
| Olfactory sensory neurons | As a part of the first step of olfaction, the odorant interacts with a G-protein coupled receptor (GPCR) on the surface of primary cilia producing the second messenger cyclic adenosine monophosphate (cAMP) within the cilium[13]. Elevated levels of cAMP opens a cyclic nucleotide-gated channel in the primary cilia, thereby, depolarizing the cell. |
| Rod and cone cells | Primary cilia on these cells have an expanded tip, called outer segment. Outer segments have opsin GPCRs on their surface, which respond to photons. When excited, these GPCRs hydrolyse cyclic guanosine monophosphate (cGMP); hence, closing the cGMP-gated channels[14]. |
| Kidney cells | Deflection of primary cilia resulting from fluid flow within the kidney results in extra cellular calcium dependent increase in intracellular calcium[15,16]. This response has been reported to be mediated by membrane bound proteins, polycystin 1, and polycystin 2[1]. |
| Chondrocytes | Stretch activated ion channel such as transient receptor potential cation channel subfamily V member 4 (TRPV4) localizes within primary cilia. TRPV4 have been shown to mediate osmotic pressure sensing[17,18]. Furthermore, deflection of primary cilia on bone cells results in a adenylyl cyclase 6, AC6, mediated decrease in cAMP[19]. |
| Fibroblasts | Primary cilia have been shown to align in the direction of cell migration[20]. Reorientation of primary cilia in the direction of cell migration has been shown to be an initiator in the process of wound healing[21]. |

Structurally, as shown in Figure 1-1, a primary cilium consists of a central axoneme containing nine circumferentially distributed microtubule doublets. The axoneme is attached at the base to the mother centriole, older of the two centrioles, and is enveloped by plasma membrane. Broadly, this structure is similar to motile cilia with one very significant difference. Unlike primary cilia, motile cilia have an additional pair of microtubule doublet at the center of the axoneme connected to the circumferentially distributed microtubule doublets through radial spokes. Their structures are commonly referred to as ‘9+0’ for primary cilia and ‘9+2’ for motile cilia, respectively.

At the base of primary cilia, a contiguous structure from the mother centriole, called the transition zone, provides necessary gating separating the molecular elements inside primary cilia from the surrounding cytosolic materials. Specifically, molecular complexes in the transition zone help differentiate between cargoes that can enter the primary cilia structure from the ones that cannot[22]. Studies have shown that Septin 2 (Sept 2) acts a diffusion barrier at the base of primary cilia[22]. Furthermore, the transition zone is populated by several proteins, which play varied roles in the process of ciliogenesis (formation of primary cilia), and maintaining its homeostatic functions, although the detailed mechanism remains elusive. These include Nephronophthisis (NPHP) 1, 4, and 8, which have been implicated to be significant players in nephronophthisis, a cystic kidney ciliopathy[23-25]. Axoneme components are delivered to the primary cilia using intraflagellar transport (IFT) proteins. Transition zone proteins in conjunction with transitional fibers are believed to recruit IFT proteins to the base of primary cilia through unknown mechanism[26-28]. Protein Cep290 localizes at the base of primary cilia and has been demonstrated to be a part of Meckel Syndrom (MKS) and Joubert Syndrome (JBTS) complexes[29,30]. Additionally, a transmembrane protein, TCTN2, has been found to be important for the structural integrity of the base of primary cilia and to play a role in MKS[31]. Together these studies reveal a dynamic environment at the base of the primary cilia consisting of proteins and protein complexes that are not only structurally important for ciliogenesis but play a significant role in maintaining functional homeostasis for primary cilia.

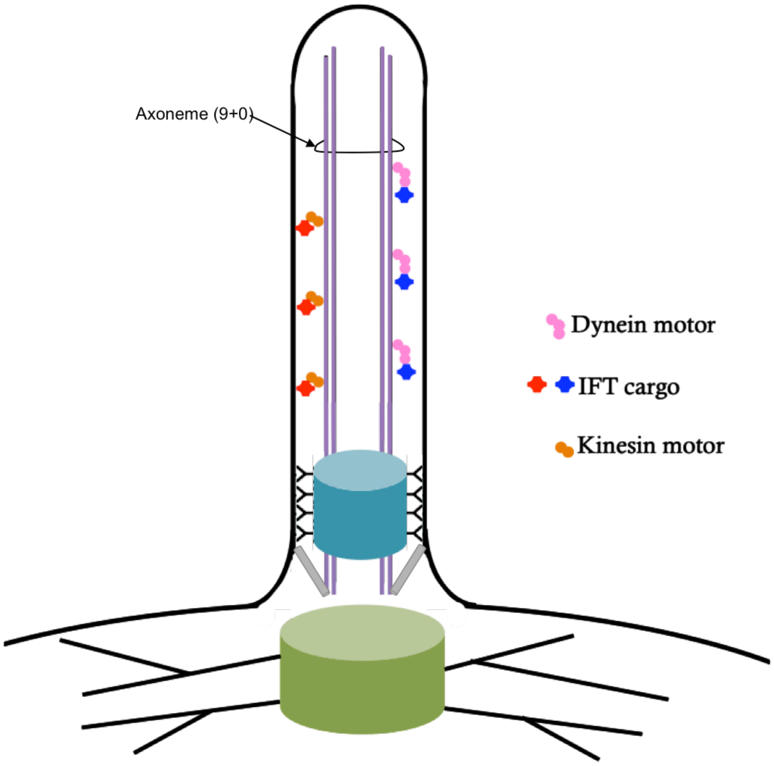

**Figure 1-1. Structure of primary cilia. Unlike motile cilia, primary cilia body consists of 9 microtubule doublets. Intraflagellar transport (IFT) rafts carry materials in and out of the primary cilia structure. Image adapted from Nature Reviews Molecular Cell Biology 12, 222. (2011)[32]**

## 1.2 Primary cilia in the context of cellular reprogramming

Cell reprogramming by expression of ectopic transcription factors has been able to convert somatic cells into induced pluripotent stem cells (iPSCs)[33-38]. Signaling pathways play important roles in generating iPSCs, where Wnt signaling promotes reprogramming[39] and de-activation of Shh pathways facilitates reprogramming[40]. Despite the importance of these pathways in iPSC reprogramming, the existence of primary cilia and their characteristics as well as potential roles in iPSCs remain unclear. As summarized in Figure 1-2, iPSCs are functionally equivalent to embryonic stem cells (ESCs), although minor differences between iPSCs and ESCs have also been reported[41,42]. Comparative studies of primary cilia and their corresponding signaling pathways between iPSCs and ESCs would provide a new test in the functional similarities and differences between these two pluripotent cell types.

A recent study demonstrated the presence of primary cilia on human ESCs (hESCs)[43]. Examining primary cilia in hESCs, the authors reported the existence and length characteristics of primary cilia in these cell lines. Furthermore, they showed the activities of molecules in the hedgehog signaling pathways, including the stimulation response of key pathway components Ptc1, Smo, Gli1, and Gli2. Studies have demonstrated that these Shh pathway elements dynamically communicated with each other on primary cilia to mediate the initiation of Shh signaling cascade[44]. Expression profiling showed that Ptc, Smo, Gli1, Gli2, and Gli3 were up-regulated in hESCs when compared with differentiated cells[45], demonstrating that Shh pathway was relatively more active in hESCs than in somatic cells.

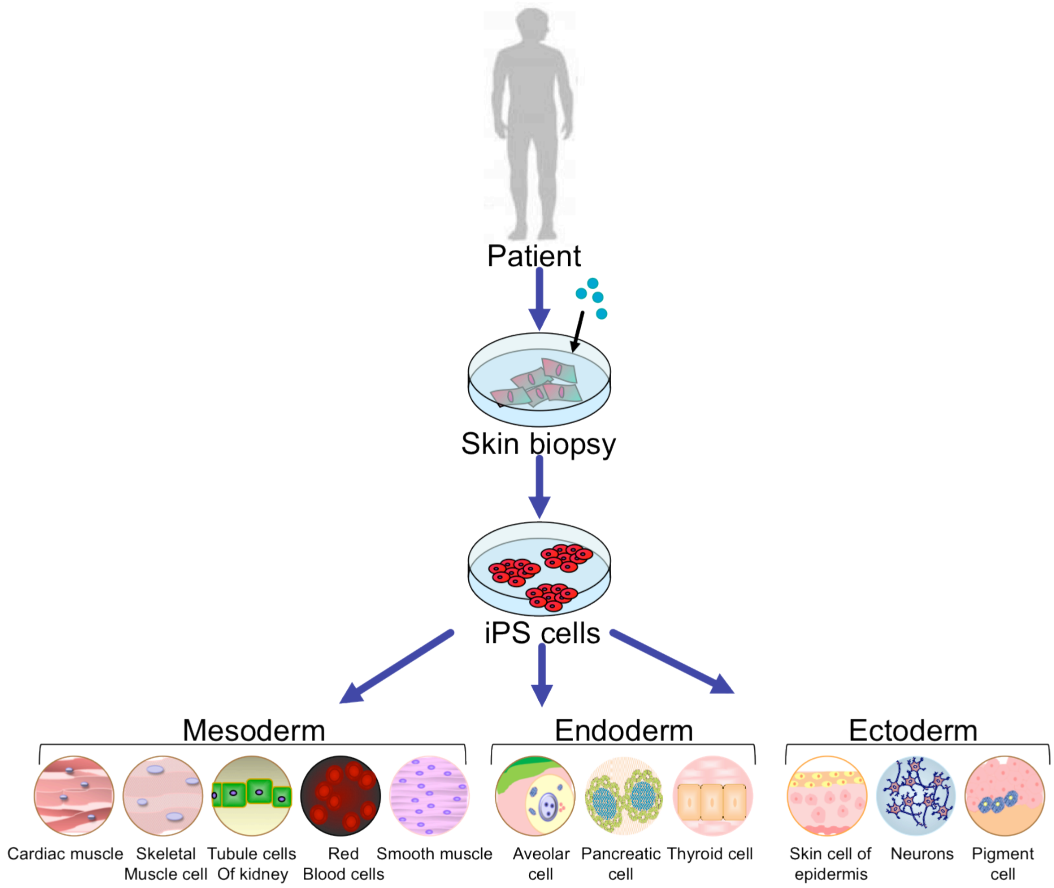

**Figure 1-2. Induced pluripotent stem cells (iPSCs) are derived by reprogramming somatic cells derived from adults, hence, circumventing all the moral and ethical dilemmas offered by embryonic stem cells (ESCs). Ectopic expression of transcription factors, OCT-4, SOX-2, Klf-4, and c-MYC in cells derived from skin biopsies resulted in generation of iPS cells. Being pluripotent, functionally equivalent to ESCs, they can differentiate into all cell types, providing a starting point for cell-based therapies and for drug development and for an improved understanding of pluripotency (Schematic adapted from SigmaAldrich.com and Nature 481, 295[46]).**

In addition to the length characteristics of primary cilia measured in ESCs, other characteristics of primary cilia morphology can also play important roles in their functions[6]. For example, modulation of mechanosensitivity in cells is believed to be mediated through changes occurring in primary cilia morphology. It is known that the length of primary cilia dictates their mechanical sensitivity[47-49]. Serum starvation is one way to increase the length of primary cilia[50]. Blocking $Ca^{2+}$ entry and increasing intracellular cAMP[48] as well as stress deprivation[49,51] have also been shown to increase the length of primary cilia. Conversely, cyclic loading has been demonstrated to decrease length of primary cilia[47,49]. Mechanical loading conditions have also been shown to influence other morphological parameters of a primary cilium such as its curvature[49], and categorizing the morphology of primary cilia has also been reported[52]. Bending of primary cilia has previously been associated with an increase in influx of calcium and suppression of cAMP[53]. On the other hand, under varying flow conditions, changes in degree of bending of primary cilia has been associated with differences in calcium measurements within kidney epithelial cells[54]. Taken together, these studies underscore the role of morphological characteristics of primary cilia and determining the transfer function for various signaling events. It is thus important to examine the effects of cell reprogramming on morphological characteristics of primary cilia to gain better understanding of potential signaling changes due to reprogramming.

In this study, we demonstrate the presence of primary cilia on human induced pluripotent stem cells (hiPSCs) through a combination of imaging based assays and quantitative PCR assays. We demonstrate the up-regulation of various signaling molecules associated with primary cilia. We performed morphometric analysis of primary cilia to examine the effects of reprogramming on various mechanical characteristics, including length, curvature, bending shape, and aggregated puncta. These mechanical studies of primary cilia for somatic cells and hiPSCs may shed light on the transition of mechanosensing landscape through the reprogramming process and provide a better understanding of the mechanical roles of primary cilia in hiPSCs.

## 1.3 Need for super-resolution microscopy

Because morphology of primary cilia governs the signaling ability of primary cilia, and specifically primary cilia on iPSCs, one should perform detailed morphological analysis of primary cilia on these cells. However, the 250-300 nm[12] resolution limit of conventional far-field optical imaging systems makes it impossible to study local changes in morphological parameters such as local variations in the curvature of primary cilia, given the size scale of primary cilia, ~200 nm in diameter. Electron microscopy can reach a much higher resolution, but it is limited by the special vacuum condition and extremely low imaging throughput. Usage of a high resolution far-field optical imaging system is thus necessary to address these gaps and to facilitate high-resolution study of primary cilia morphology.

## 1.4 A brief history of super-resolution microscopy

The resolution limit of light was first proposed by Ernst Abbe[55]. His law has been accepted to be a fundamental limit on microscopy since the end of 19th century. The law stated that objects closer than about half the wavelength of light being used to image them could not be distinguished as that was the smallest spot size allowed by diffraction when the light passes through any optical element such as an objective lens. It was quantified using the famous Abbe's equation:

$$\Delta x \approx \frac{\lambda}{2n \sin \alpha}$$

where, Δx=spatial resolution, λ=wavelength of light used, 2n sinα=numerical aperture of the microscope.

Techniques to overcome the diffraction barrier offered by Abbe's law have been developed in the past. Most notably, electron microscopy[56] and near field microscopy[57] techniques can circumvent this barrier. However, the following are the two major limitations of these techniques:

1. Low throughput
2. Fundamental incompatibility with live cell applications

Electron microscopy takes advantage of the extremely small wavelength of electron propagation to overcome the diffraction limit. However, it requires a vacuum environment to function and therefore is fundamentally not suitable for live cell applications. Furthermore, extensive sample preparation also limits the throughput of the technique. Near field microscopy relies on the proximity of the detection probe to the sample, to sidestep the diffraction barrier. However, given that the probe needs to be within nanometers of the sample, the technique is not useful in studying any phenomenon that occur at a reasonable distance from the surface. This limits its applicability in biological settings.

Recent developments in microscopy make it possible to circumvent the Abbe's law and perform super-resolution imaging. Stochastic super-resolution techniques such as PhotoActivated Localization Microscopy (PALM)[58], Fluorescence PhotoActivated Localization Microscopy (FPALM)[59], STochastic Optical Reconstruction Microscopy (STORM)[60], direct STORM (dSTORM)[61], targeted read-out techniques, such as, Stimulated Emission Depletion (STED)[62] microscopy, Ground State Depletion (GSD)[63] microscopy, Saturated Structured Illumination Microscopy (SSIM)[64], Point Accumulation for Imaging in Nanoscale Tomography (PAINT)[65], and myriad derivatives[66-70] of these techniques, have offered several alternatives recently to circumvent the Abbe's limit.

Stochastic techniques achieve super-resolution by turning ON/OFF a small subset of the total number of fluorophores available in the focal volume[71,72]. If the individual fluorophores that emit fluorescence photons are separated by more than an Abbe's distance, the coordinates of those fluorophores can be calculated with near arbitrary precision[73,74]. ON/OFF states of the fluorophores are achieved using either photoactivation[75] or photoswitching[76]. Because a random subset of fluorophores is activated per frame, several hundred to thousand frames are collected to produce an individual 'image'. Resolution of stochastic super-resolution techniques depends on the number of fluorophore emitted by individual fluorophore molecules. If a molecule emits s photons, the precision calculating the coordinates of its position using a stochastic technique, is given by[74]:

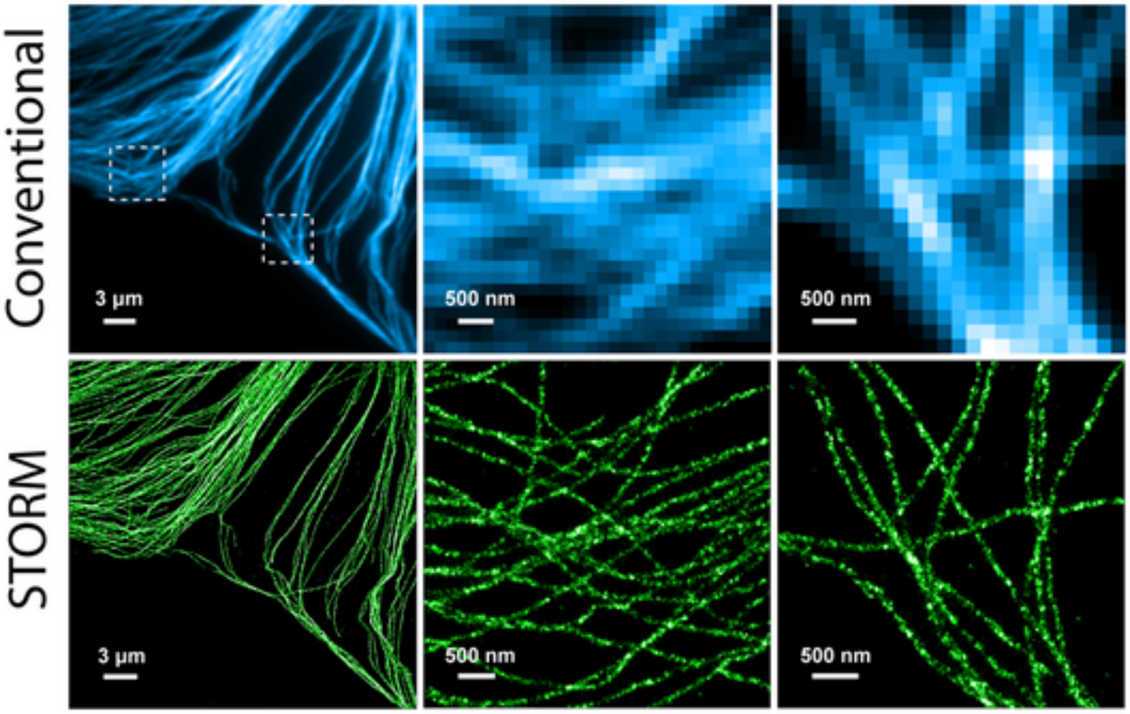

**Figure 1-3. Images demonstrating improvement in resolution achieved by STORM microscopy. Top panel shows conventional images of microtubules labeled on BS-C-1 cells. Bottom panel shows STORM images of the same regions underscoring the improvement in resolution achieved. Images adapted from Science 317, 1749-1753 (2007)[72]**

$$\sigma = \frac{\lambda}{2n\, sin\alpha\sqrt{s}}$$

Therefore, the brighter the fluorophore, the larger the s for the given fluorophore, and hence the better the resolution. Exploiting this principle, stochastic techniques, such as STORM, PALM, etc. have to-date been able to achieve <20 nm resolution in the focal plane[58,60,77]. Figure 1-3 and Figure 1-4 demonstrate representative image data sets collected using STORM and PALM respectively.

While PALM, STORM, and their derivatives depend on switching fluorophores ON/OFF stochastically, Point Accumulation for Imaging in Nanoscale Topography (PAINT)[78] depends on continuously targeting the imaging surface with fluorescent probes that are present in the solution. Each time a fluorophore binds to a surface molecule, it emits fluorescent photons (turns ON). Each time it dissociates from the surface or photobleaches, the fluorescence turns OFF. Therefore, the sample inherently fluoresces stochastically. Using algorithms similar to the ones described in the previous paragraph, the coordinates of these interactions are calculated providing a super-resolution view of the sample surface[79].

Amongst these techniques, STED has been demonstrated to be most suitable to studying biological questions. This stems from the fact that STED not only provides ~4-fold improvement in resolution, majority of the other super-resolution techniques enumerated in the previous paragraph also offer competing resolutions, it achieves this resolution based on photo-physical manipulation of fluorophores. This enables image acquisition rates of STED to be at par with conventional imaging technologies, making it the only technique offering spatial resolution superior to conventional imaging systems while not compromising with the temporal resolution.

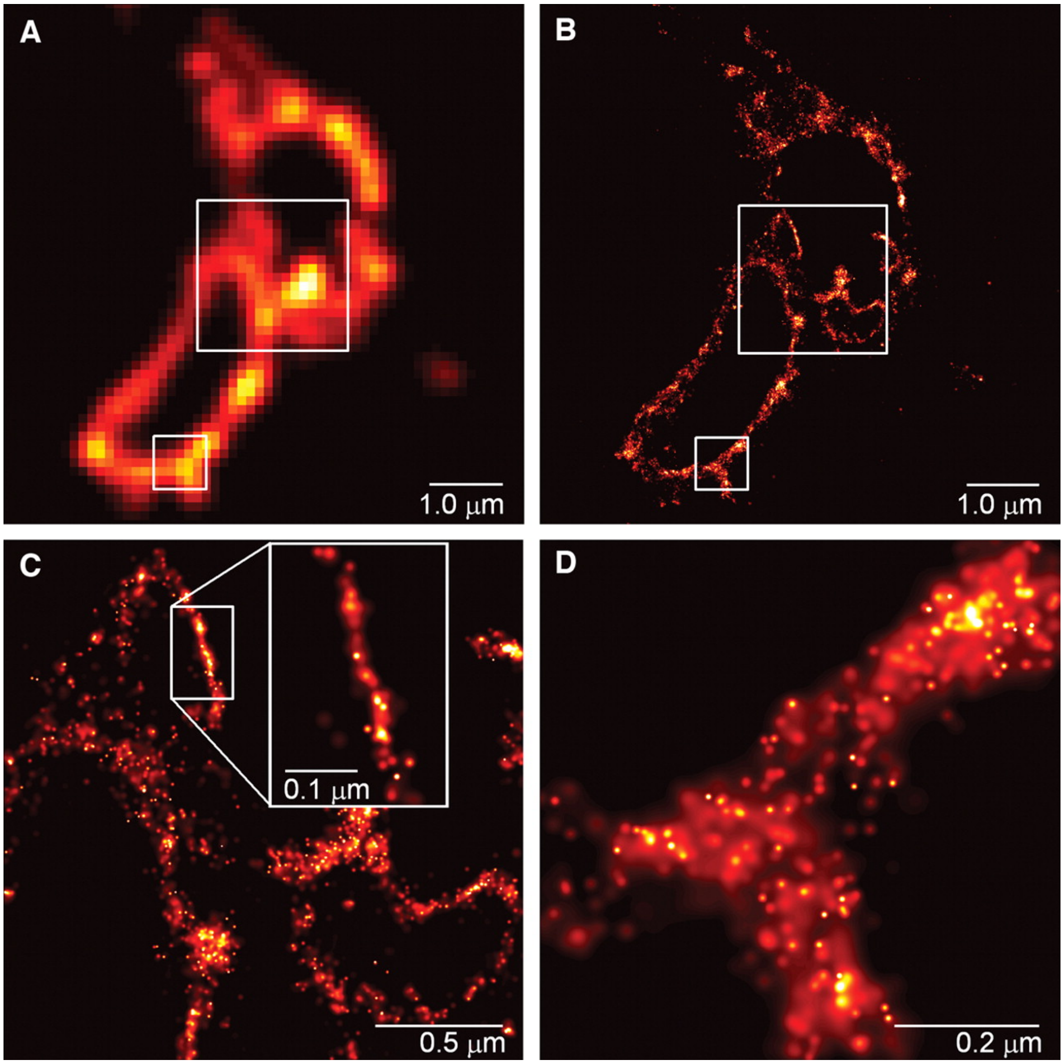

**Figure 1-4. Figure sequence demonstrating application of PALM microscopy. COS-7 cells expressing lysosomal transmembrane protein CD63 tagged with PA-FP Kaede were imaged using TIRF (A) and PALM (B). (C) and (D) are zoomed in versions of subregions of the PALM image underscoring the resolution improvement achieved by PALM. Image adapted from Science 313: 1642-1645 (2006)[58]**

## 1.5 Outline of this work

After briefly sketching out the background about the topics of interest in this work in chapter 1, chapter 2 will cover the details of implementation of super-resolution apSTED, a faster version of STED implemented by accelerating a piezoelectrically driven stage scanner, microscopy system. We will briefly touch upon the principle that governs STED microscopes. Further, we will discuss the various stages of development and validation of different parts of the system. We will discuss data that underscores the resolution improvement achieved by our STED system. We will also briefly touch upon the enhancements implemented to make apSTED more widely adaptable and useful for applications in various biological fields.

Chapter 3 details results of several imaging based studies that we undertook on primary cilia. Specifically, we setup assays to label and identify primary cilia structures. We report results of labeling components of the axonemal structure of primary cilia, components of transition zone, and basal body of primary cilia. We establish approaches that allow us to study primary cilia from three major perspectives, large scale mechanical structure of primary cilia, molecular structure of primary cilia, and components of primary cilia that participate in mediation of various signaling pathways.

While primary cilia have several important roles in fully differentiated lineage defined adult cells, more recent studies have highlighted their role in embryonic stem cell biology. In chapter 4, we report results of our studies on primary cilia on human induced pluripotent stem cells (hiPSCs). Using myriad imaging and biochemical assays, we are the first group to report the presence of primary cilia on hiPSCs. We performed a differential morphometric analysis of primary cilia on somatic (adult) cells vs hiPSCs. Our data show significant differences in morphology of primary cilia on these cell types, indicative of differences in signal sensing and modulation on hiPSCs performed by primary cilia. Work in chapter 4 appears in Nathwani et al., *Stem Cells and Development*, under review.

Chapter 5 extensively details results of imaging primary cilia using apSTED microscopy. Typically, biological samples scatter light more than clean calibration samples. Therefore, we focus our attention on the improvement in resolution achieved by STED on biologically interesting samples, a more stringent test than imaging traditional calibration samples. We also focus on several image-processing modules that we developed to extract quantifications from STED images. We utilize these scripts to analyze data collected using both confocal and STED microscopes to underscores the advances that can be achieved in studying primary cilia using STED as opposed to conventional imaging techniques. Specifically, we utilize the superior apSTED system to image several transition zone components, such as, TCTN2, and Cep290.

In chapter 6, we briefly summarize our results and recommend future steps to enhance this exciting technology even further. We believe with all the exciting developments happening in the field, STED has the potential to become an indispensable tool for all cutting-edge biology labs.

## References:

1. Nauli, S. M. *et al.* Polycystins 1 and 2 mediate mechanosensation in the primary cilium of kidney cells. *Nat Genet* **33**, 129–137 (2003).
2. Malone, A. *et al.* Primary cilia mediate mechanosensing in bone cells by a calcium-independent mechanism. *Proceedings of the National Academy of Sciences* **104**, 13325 (2007).
3. Benton, R., Sachse, S., Michnick, S. W. & Vosshall, L. B. Atypical membrane topology and heteromeric function of Drosophila odorant receptors in vivo. *PLoS Biol* **4**, e20 (2006).
4. Zimmermann, K. Beiträge zur Kenntniss einiger Drüsen und Epithelien. *Archiv f. mikrosk. Anatomie* **52**, 552–706 (1898).
5. Davenport, J. R. & Yoder, B. K. An incredible decade for the primary cilium: a look at a once-forgotten organelle. *Am J Renal Physiol* **289**, F1159–F1169 (2005).
6. Hoey, D. A., Downs, M. E. & Jacobs, C. R. The mechanics of the primary cilium: An intricate structure with complex function. *J Biomech* (2011).doi:10.1016/j.jbiomech.2011.08.008
7. Rohatgi, R., Milenkovic, L. & Scott, M. P. Patched1 regulates hedgehog signaling at the primary cilium. *Science* **317**, 372–376 (2007).
8. Ingham, P. W., Nakano, Y. & Seger, C. Mechanisms and functions of Hedgehog signalling across the metazoa. *Nat. Rev. Genet.* **12**, 393–406 (2011).

9. Veland, I. R., Awan, A., Pedersen, L. B., Yoder, B. K. & Christensen, S. O. R. T. Primary Cilia and Signaling Pathways in Mammalian Development, Health and Disease. *Cell Physiol Biochem* **111**, p39–p53 (2009).
10. Ansley, S. J. *et al.* Basal body dysfunction is a likely cause of pleiotropic Bardet–Biedl syndrome. *Nature Cell Biology* **425**, 628–633 (2003).
11. Badano, J. L., Mitsuma, N., Beales, P. L. & Katsanis, N. The Ciliopathies: An Emerging Class of Human Genetic Disorders. *Annu. Rev. Genom. Human Genet.* **7**, 125–148 (2006).
12. Adams, M., Smith, U. M., Logan, C. V. & Johnson, C. A. Recent advances in the molecular pathology, cell biology and genetics of ciliopathies. *Journal of Medical Genetics* **45**, 257–267 (2008).
13. I Boekhoff, E. T. J. S. H. B. Rapid activation of alternative second messenger pathways in olfactory cilia from rats by different odorants. *The EMBO Journal* **9**, 2453 (1990).
14. Calvert, P. D., Strissel, K. J., Schiesser, W. E., Pugh, E. N., Jr & Arshavsky, V. Y. Light-driven translocation of signaling proteins in vertebrate photoreceptors. *Trends in cell biology* **16**, 560–568 (2006).
15. Praetorius, H. A. & Spring, K. R. Bending the MDCK Cell Primary Cilium Increases Intracellular Calcium. *Archiv f. mikrosk. Anatomie* **184**, 71–79 (2001).
16. Praetorius, H. A. & Spring, K. R. Removal of the MDCK Cell Primary Cilium Abolishes Flow Sensing. *Archiv f. mikrosk. Anatomie* **191**, 69–76 (2003).
17. Gradilone, S. A. *et al.* Cholangiocyte cilia express TRPV4 and detect

changes in luminal tonicity inducing bicarbonate secretion. *Proc Natl Acad Sci USA* **104**, 19138–19143 (2007).

18. Phan, M. N. *et al.* Functional characterization of TRPV4 as an osmotically sensitive ion channel in porcine articular chondrocytes. *Arthritis Rheum* **60**, 3028–3037 (2009).
19. Kwon, R. Y., Temiyasathit, S., Tummala, P., Quah, C. C. & Jacobs, C. R. Primary cilium-dependent mechanosensing is mediated by adenylyl cyclase 6 and cyclic AMP in bone cells. *FASEB J.* **24**, 2859–2868 (2010).
20. Albrecht-Buehler, G. Phagokinetic tracks of 3T3 cells: Parallels between the orientation of track segments and of cellular structures which contain actin or tubulin. *Cell* **12**, 333–339 (1977).
21. Schneider, L. *et al.* Directional Cell Migration and Chemotaxis in Wound Healing Response to PDGF-AA are Coordinated by the Primary Cilium in Fibroblasts. *Cell Physiol Biochem* **25**, 279–292 (2010).
22. Hu, Q. *et al.* A Septin Diffusion Barrier at the Base of the Primary Cilium Maintains Ciliary Membrane Protein Distribution. *Science* **329**, 436–439 (2010).
23. Williams, C. L., Winkelbauer, M. E., Schafer, J. C., Michaud, E. J. & Yoder, B. K. Functional Redundancy of the B9 Proteins and Nephrocystins in Caenorhabditis elegans Ciliogenesis. *Molecular Biology of the Cell* **19**, 2154–2168 (2008).
24. Fliegauf, M. Nephrocystin Specifically Localizes to the Transition Zone of Renal and Respiratory Cilia and Photoreceptor Connecting Cilia. *Journal of*

*the American Society of Nephrology* **17**, 2424–2433 (2006).

25. Jiang, S. T. *et al.* Targeted disruption of Nphp1 causes male infertility due to defects in the later steps of sperm morphogenesis in mice. *Hum. Mol. Genet.* **17**, 3368–3379 (2008).
26. Zhao, C. & Malicki, J. Nephrocystins and MKS proteins interact with IFT particle and facilitate transport of selected ciliary cargos. *Nature* **30**, 2532–2544 (2011).
27. Ishikawa, H., Kubo, A., Tsukita, S. & Tsukita, S. Odf2-deficient mother centrioles lack distal/subdistal appendages and the ability to generate primary cilia. *Nature Cell Biology* **7**, 517–524 (2005).
28. Singla, V., Romaguera-Ros, M., García-Verdugo, J. M. & Reiter, J. F. Ofd1, a Human Disease Gene, Regulates the Length and Distal Structure of Centrioles. *Trends in cell biology* **18**, 410–424 (2010).
29. Garcia-Gonzalo, F. R. *et al.* A transition zone complex regulates mammalian ciliogenesis and ciliary membrane composition. *Nat Genet* **43**, 776–784 (2011).
30. Sang, L. *et al.* Mapping the NPHP-JBTS-MKS protein network reveals ciliopathy disease genes and pathways. *Cell* **145**, 513–528 (2011).
31. Shaheen, R. *et al.* A TCTN2 mutation defines a novel Meckel Gruber syndrome locus. *Hum. Mutat.* **32**, 573–578 (2011).
32. Ishikawa, H. & Marshall, W. F. Ciliogenesis: building the cell's antenna. *Nat Rev Mol Cell Biol* **12**, 222–234 (2011).
33. Takahashi, K. & Yamanaka, S. Induction of pluripotent stem cells from

mouse embryonic and adult fibroblast cultures by defined factors. *Cell* **126**, 663–676 (2006).

34. Wernig, M. *et al.* In vitro reprogramming of fibroblasts into a pluripotent ES-cell-like state. *Nature* **448**, 318–324 (2007).
35. Stadtfeld, M., Nagaya, M., Utikal, J., Weir, G. & Hochedlinger, K. Induced Pluripotent Stem Cells Generated Without Viral Integration. *Science* **322**, 945–949 (2008).
36. Takahashi, K. *et al.* Induction of pluripotent stem cells from adult human fibroblasts by defined factors. *Cell* **131**, 861–872 (2007).
37. Okita, K., Ichisaka, T. & Yamanaka, S. Generation of germline-competent induced pluripotent stem cells. *Nature* **448**, 313–317 (2007).
38. Yu, J. *et al.* Induced Pluripotent Stem Cell Lines Derived from Human Somatic Cells. *Science* **318**, 1917–1920 (2007).
39. Li, W. *et al.* Generation of rat and human induced pluripotent stem cells by combining genetic reprogramming and chemical inhibitors. *Cell Stem Cell* **4**, 16–19 (2009).
40. Dimos, J. T. *et al.* Induced Pluripotent Stem Cells Generated from Patients with ALS Can Be Differentiated into Motor Neurons. *Science* **321**, 1218–1221 (2008).
41. Stadtfeld, M. *et al.* Aberrant silencing of imprinted genes on chromosome 12qF1 in mouse induced pluripotent stem cells. *Nature* **465**, 175–181 (2010).
42. Lister, R. *et al.* Hotspots of aberrant epigenomic reprogramming in human

induced pluripotent stem cells. *Nature* **471**, 68–73 (2011).

43. Kiprilov, E. *et al.* Human embryonic stem cells in culture possess primary cilia with hedgehog signaling machinery. *The Journal of Cell Biology* **180**, 897 (2008).
44. Chih, B. *et al.* A ciliopathy complex at the transition zone protects the cilia as a privileged membrane domain. *Nature Cell Biology* **14**, 61–72 (2012).
45. Rho, J.-Y. *et al.* Transcriptional profiling of the developmentally important signalling pathways in human embryonic stem cells. *Hum. Reprod.* **21**, 405–412 (2006).
46. Robinton, D. A. & Daley, G. Q. The promise of induced pluripotent stem cells in research and therapy. *Nature* **481**, 295–305 (2012).
47. Resnick, A. ScienceDirect - Biophysical Journal : Force-Response Considerations in Ciliary Mechanosensation. *Biophys J* (2007).
48. Besschetnova, T. Y. *et al.* Identification of signaling pathways regulating primary cilium length and flow-mediated adaptation. *Curr. Biol.* **20**, 182–187 (2010).
49. Gardner, K., Arnoczky, S. P. & Lavagnino, M. Effect of in vitro stress-deprivation and cyclic loading on the length of tendon cell cilia in situ. *J. Orthop. Res.* **29**, 582–587 (2011).
50. Schneider, L. *et al.* PDGFRalphaalpha signaling is regulated through the primary cilium in fibroblasts. *Curr. Biol.* **15**, 1861–1866 (2005).
51. McGlashan, S. R. *et al.* Mechanical loading modulates chondrocyte primary cilia incidence and length. *Cell. Biol. Int.* **34**, 441–446 (2010).

52. Lavagnino, M., Arnoczky, S. P. & Gardner, K. In situ deflection of tendon cell-cilia in response to tensile loading: an in vitro study. *J. Orthop. Res.* **29**, 925–930 (2011).

53. Masyuk, A. I. *et al.* Cholangiocyte Cilia Detect Changes in Luminal Fluid Flow and Transmit Them Into Intracellular Ca2+ and cAMP Signaling. *Trends in cell biology* **131**, 911–920 (2006).

54. Rydholm, S. *et al.* Mechanical properties of primary cilia regulate the response to fluid flow. (2010).

55. Abbe, E. Beiträge zur Theorie des Mikroskops und der mikroskopischen Wahrnehmung. *Archiv f. mikrosk. Anatomie* **9**, 413–418 (1873).

56. Erni, R., Rossell, M., Kisielowski, C. & Dahmen, U. Atomic-Resolution Imaging with a Sub-50-pm Electron Probe. *Phys. Rev. Lett.* **102**, 096101 (2009).

57. Oshikane, Y. *et al.* Observation of nanostructure by scanning near-field optical microscope with small sphere probe. *Science and Technology of Advanced Materials* **8**, 181–185 (2007).

58. Betzig, E. *et al.* Imaging intracellular fluorescent proteins at nanometer resolution. *Science* **313**, 1642 (2006).

59. Hess, S., Girirajan, T. & Mason, M. Ultra-high resolution imaging by fluorescence photoactivation localization microscopy. *Biophys J* **91**, 4258–4272 (2006).

60. Rust, M., Bates, M. & Zhuang, X. Sub-diffraction-limit imaging by stochastic optical reconstruction microscopy (STORM). *Nat Methods* **3**, 793–796

(2006).

61. Heilemann, M. *et al.* Subdiffraction-resolution fluorescence imaging with conventional fluorescent probes. *Angewandte Chemie (International ed in English)* **47**, 6172–6176 (2008).

62. Dyba, M., Egner, A. & Hell, S. Fluorescence microscopy with diffraction resolution barrier broken by stimulated emission. *Proceedings of the …* (2000).

63. Hein, B., Jakobs, S., Eggeling, C. & Hell, S. Fluorescence nanoscopy by ground-state depletion and single-molecule return. *Nat Methods* (2008).

64. Gustafsson, M. G. L. Nonlinear structured-illumination microscopy: Wide-field fluorescence imaging with theoretically unlimited resolution. *Proc Natl Acad Sci USA* **102**, 13081–13086 (2005).

65. Sharonov, A. & Hochstrasser, R. M. Wide-field subdiffraction imaging by accumulated binding of diffusing probes. *Proc Natl Acad Sci USA* **103**, 18911–18916 (2006).

66. Harke, B., Medda, R. & Hell, S. STED microscopy with continuous wave beams. *Nat Methods* (2007).

67. Huang, B., Jones, S. & Brandenburg, B. Whole-cell 3D STORM reveals interactions between cellular structures with nanometer-scale resolution. *Nat Methods* (2008).

68. Lauterbach, M., Kamin, D., Jahn, R. & Hell, S. Video-rate far-field optical nanoscopy dissects synaptic vesicle movement. *Science* (2008).

69. Shtengel, G. *et al.* Interferometric fluorescent super-resolution microscopy

resolves 3D cellular ultrastructure. *Proc Natl Acad Sci USA* **106**, 3125–3130 (2009).

70. Planchon, T. A. *et al.* Rapid three-dimensional isotropic imaging of living cells using Bessel beam plane illumination. *Nat Methods* **8**, 417–423 (2011).
71. Shroff, H., Galbraith, C. G., Galbraith, J. A. & Betzig, E. Live-cell photoactivated localization microscopy of nanoscale adhesion dynamics. *Nat Methods* **5**, 417–423 (2008).
72. Bates, M., Huang, B. & Dempsey, G. Multicolor super-resolution imaging with photo-switchable fluorescent probes. *Science* (2007).
73. Betzig, E. Proposed method for molecular optical imaging. *Optics letters* **20**, 237 (1995).
74. Thompson, R. E., Larson, D. R. & Webb, W. W. Precise nanometer localization analysis for individual fluorescent probes. *Biophys J* **82**, 2775–2783 (2002).
75. Shroff, H. *et al.* Dual-color superresolution imaging of genetically expressed probes within individual adhesion complexes. *Proc Natl Acad Sci USA* **104**, 20308–20313 (2007).
76. Xu, K., Babcock, H. P. & Zhuang, X. Dual-objective STORM reveals three-dimensional filament organization in the actin cytoskeleton. *Nat Methods* (2012).doi:10.1038/nmeth.1841
77. Fölling, J. *et al.* Photochromic Rhodamines Provide Nanoscopy with Optical Sectioning. *Angew. Chem. Int. Ed.* **46**, 6266–6270 (2007).

78. Sharonov, A. & Hochstrasser, R. M. Wide-field subdiffraction imaging by accumulated binding of diffusing probes. *Proc Natl Acad Sci USA* **103**, 18911–18916 (2006).

79. Giannone, G. *et al.* Dynamic Superresolution Imaging of Endogenous Proteins on Living Cells at Ultra-High Density. *Trends in cell biology* **99**, 1303–1310 (2010).

# 2 Development of super-resolution imaging system – apSTED nanoscopy

Typically, cell biology problems have been studied using far-field optical microscopy systems. There are several advantages to this approach. Specifically, widely applicable protein labeling strategies have been perfected over the years. Utilizing these strategies, it is possible to fluorescently label biomolecules with minimal to no interference with the functioning of those molecules. Recent development of fluorescent proteins has also rendered the challenge of specificity superfluous. Furthermore, flurophores are available across the visible spectrum and it has become increasingly easier to perform multi-model, multi-color fluorescence based assays to study multiple processes simultaneously. This coupled with the commercial availability and ease of operation of the fluorescence microscope makes optical microscopy a tool of choice for biology. However, as discussed in detail in chapter 1, we have reached an inflection point in the field where current problems in biology are challenging the resolution limits of these microscopes and are no longer readily amenable to conventional imaging tools. Here, we report the development of a super-resolution apSTED nanoscopy system, or **a**ccelerated **p**iezoelectric stage scanning STED nanoscopy, that allows us to circumvent the challenge of diffraction-limited resolution and enables studies of biomolecules at previously unprecedented resolution.

## 2.1 Principle of STED microscopy

Identifying spectrally separated, different colored, fluorophores is not challenged by Abbe’s barrier i.e. fluorophores of different colors can be discerned at arbitrary closeness in spatial dimensions. Similarly, Abbe’s law also does not prevent calculation of coordinate of a light emitting molecule with arbitrary precision, a fact exploited remarkably well in stochastic super-resolution imaging systems. Along similar lines, it is possible to sidestep Abbe’s barrier physically if the densely packed fluorophores are forced to emit sequentially instead of all at once. This fact forms the backbone of the STED principle.

**Figure 2-1. Principle of STED microscopy. A red shifted toroid shaped depletion beam is super-imposed on a diffraction limited excitation spot size. The photophysical dynamics of the fluorophore resulting from exposure to these two pulses results in fluorescence being generated from the central zero of the toroid providing super-resolved fluorescence spot. This super-resolved spot is scanned across a sample to generate image pixels.**

STED works by transiently switching off fluorophores in the outer rim of diffraction limited fluorescence excitation spot. To achieve this, typically, a diffraction-limited spot of excitation laser beam is overlapped with a toroid shaped spot of a red-shifted laser beam, called depletion beam. This scheme is demonstrated by a schematic in Figure 2-1. The depletion beam deexcites the fluorophores from excited energy state to ground state through the well understood process of stimulated emission. Thus, effectively only the fluorophores in the toroid center are excited, thereby decreasing the effective point spread function and achieving super-resolution. Studies have demonstrated the effectiveness of STED at studying nano-scale phenomena, including the study of biological problems at the cellular level.

While diffraction governs both the laser lines, the effective reduction is point spread function is what enables the user to sidestep the Abbe barrier. The governing equation[1] quantifying the resolution of the system, modified Abbe's equation, is:

$$\Delta x \approx \frac{\lambda}{2n \sin \alpha \sqrt{1 + \frac{I}{I_s}}}$$

Where, I=intensity of the depletion laser, $I_s$=laser intensity to deplete 50% of the fluorophores

## 2.2 Implementation of STED system

At the Liao lab, we implemented a continuous wave (CW) STED nanoscopy system based on a previously reported design[2]. Using a diode-pumped solid state (DPSS) 491 nm laser line (Calypso 25, Cobolt Ab) as an excitation source and a 1000 mW, 592 nm fiber laser line (VFL-P-1000-592, MPB Communications Inc.) as a depletion source, we implemented the system following the schematic shown in Figure 2-2. The two laser lines were coupled into their respective single mode polarization maintaining fibers (p3-488pm-fc-2, Thorlabs) to clean and filter the pulses. A vortex phase mask (VPP1, RPC Photonics) introducing helical phase ramp of $\exp(i\varphi)$ with $0 < \varphi < 2\pi$ was used to sculpt the depletion beam into a toroid shape. The lasers were merged using dichroic mirrors (Semrock) and subsequently focused at an equi-focal plane using an oil immersion objective lens (Olympus UPLSAPO100x-1.4 NA). The sample was placed on a 3-axis piezoelectric stage scanner (Nano-PDQ375HS, Mad City Labs Inc). Fluorescence being an Omni-directional phenomenon, signal was collected using the same objective lens. Subsequently, both the laser lines were separated from the signal using dichroics (Semrock). Signals were cleaned using a 532/22 band-pass filter (Semrock). After filtering, the signal was coupled to a multi-mode fiber (M31L05, Thorlabs) with a core diameter of 80% of the back projected airy disk to achieve confocalization of the signal. In accordance with the brightness of the sample, a photo-multiplier tube, PMT, (MP963, PerkinElmer Optoelectronics) or an avalanche photo-diode, APD, (SPCM-AQR-15, PerkinElmer Optoelectronics) was used as a detector.

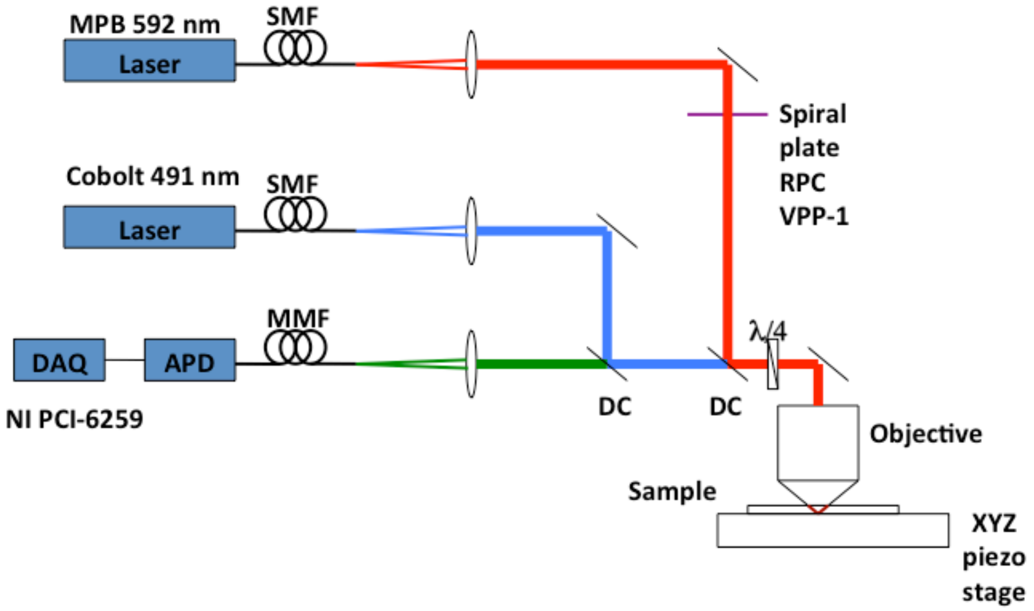

**Figure 2-2. Schematic of the STED setup implemented at Liao lab. 491 and 592 nm laser lines were used as excitation and depletion sources respectively. The depletion laser was passed through a 2pi phase retardation plate before coupling it into a confocal imaging path collinear with the excitation laser. An avalanche photodiode was used as the detection source of choice. Laser focusing and signal collection was done through a 100x 1.4 NA Olympus objective lens. Sample was scanned using an XYZ piezoelectrically driven stage**

### 2.2.1 Excitation Coupling

The excitation coupling is shown in **Figure 2-3**, with the following components:

A. A 491 nm, 25 mW, excitation laser source (Calypso 25, Cobolt Ab). This laser was used as an excitation source for STED imaging and also enabled confocal imaging

B. Mounted achromatic half wave plate (AHWP05M-630, Thorlabs)

C. Precision linear polarizer (10LP-Vis-B, Newport Corporation). A combination of half wave plate and a polarizer act as an adjustable optical attenuator.

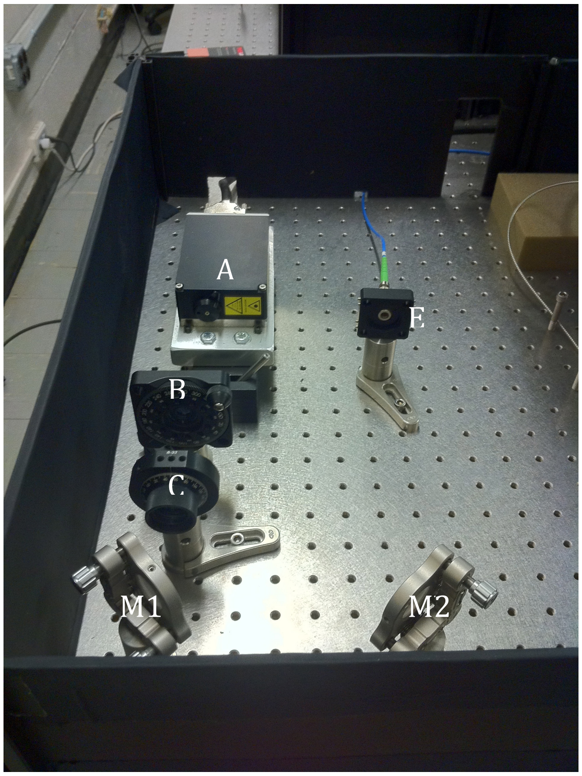

**Figure 2-3. Coupling excitation laser into a single mode polarization maintaining fiber.**

D. Mirrors M1 (10D20BD.1, Newport Corporation) and M2. The two mirrors enable the coupling of the laser into the single mode polarization maintaining fiber.

E. Collimator (F280APC-A, Thorlabs). Used to focus the collimated laser beam into the optical fiber.

F. Single mode polarization maintaining fiber (P3-488PM-FC-2, Thorlabs). Enables the decoupling of the laser source from the rest of the optical setup. Enables high fidelity coupling of the laser to be carried over to the main optical path of the system. All fibers used in this setup were FC/APC cut, in order to reduce the amount of back reflection from the fiber.

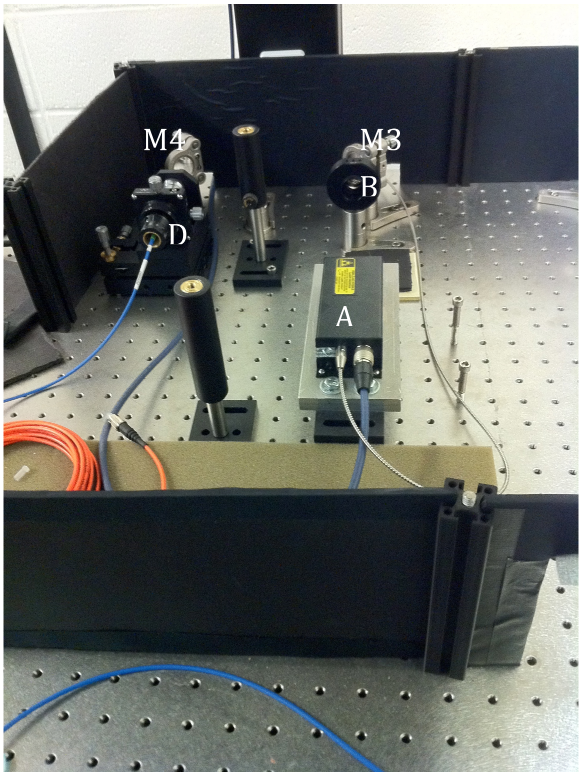

**Figure 2-4. Coupling the depletion laser into a single mode polarization maintaining fiber.**

### 2.2.2 Depletion Coupling

The depletion coupling is shown in Figure 2-4, with the following components:

A. A 592 nm, 1 W, depletion laser source (VFL-P-1000-592, MPB Communications Inc.). This source was used to achieve stimulated emission of the fluorophores in the focal volume.

B. Polarizer. Used to clean the laser beam and to prepare it to be launched into an optical fiber.
C. Mirrors M3 and M4. Are used to afford the necessary degrees of freedom in order to be able to couple the laser beam into the fiber.
D. Optical fiber coupler (F91-c1, Newport Corporation). Contains an xyz stage that can hold the optical fiber and an objective lens to focus the laser beam into the fiber.

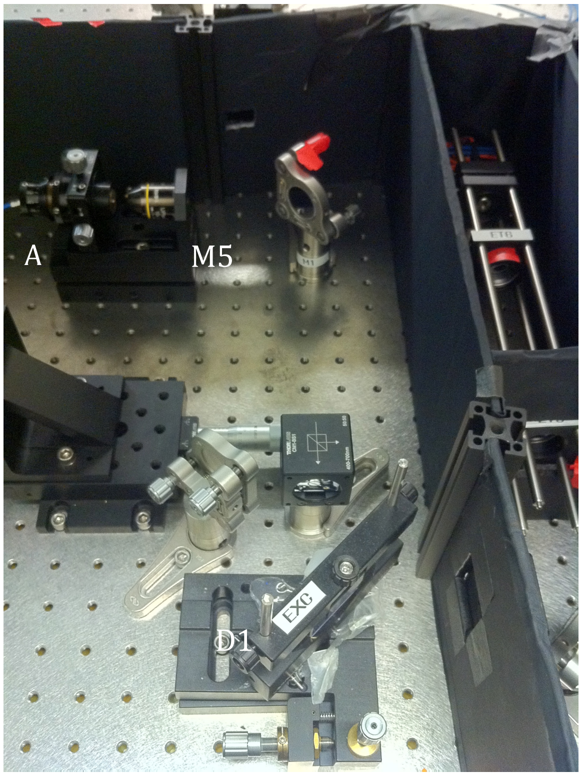

**Figure 2-5. Excitation out-coupler launching the laser onto a dichroic mirror that would couple it into the main optical path.**

### 2.2.3 Excitation fiber launch

The excitation fiber launch is shown in Figure 2-5, with the following components:

A. Optical fiber out-coupler that launches the excitation laser beam.

B. Mirror M5. Used to steer the beam into the main optical path through the dichroic mirror.

C. Dichroic D1. It reflects the excitation laser wavelength while allowing light of longer wavelengths to pass through. As a consequence, it couples the excitation laser into the main (common) optical path by reflecting it and couples the fluorescent signal onto the detection pathway by allowing it to pass through.

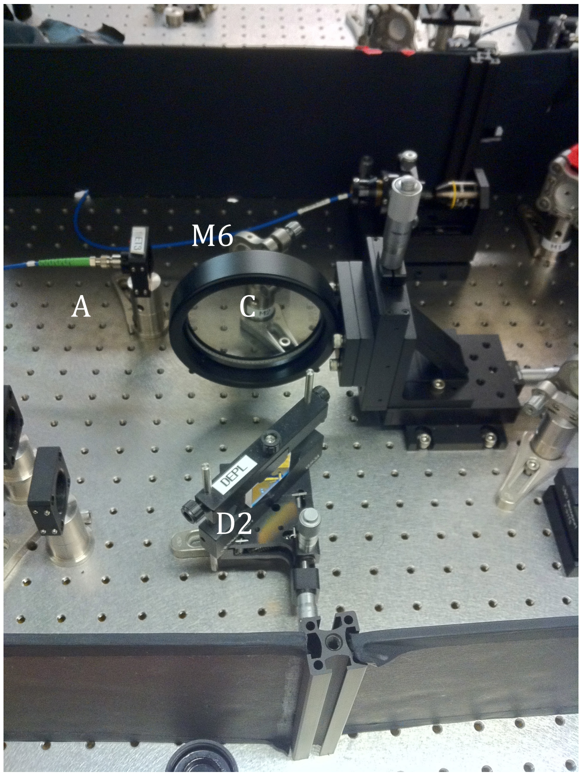

**Figure 2-6. Collimator launches the depletion laser onto a dichroic passing through a phase retardation plate that engineers the beam wave-front to produce a toroid at the plane-of-focus. The dichroic couples the engineered depletion laser beam onto the common optical path.**

### 2.2.4 Depletion fiber launch

Figure 2-6 shows depletion fiber launch, with the following components:

A. Depletion laser is launched at the other end of the fiber using a collimator. The collimator converts the focused depletion laser beam to a collimated state again.

B. Mirror M6. This mirror reflects the depletion laser on to a dichroic, which will subsequently couple the laser in to the main optical path.

C. Vortex phase plate (VPP-1, RPC Photonics Inc.). The vortex phase plate introduces 2-pi phase retardation on the depletion laser, which results in generation of a donut at the plane of focus of this laser.

D. Dichroic D2. Couples the depletion laser into the main optical path by reflecting it. It also allows the fluorescent signal to pass through.

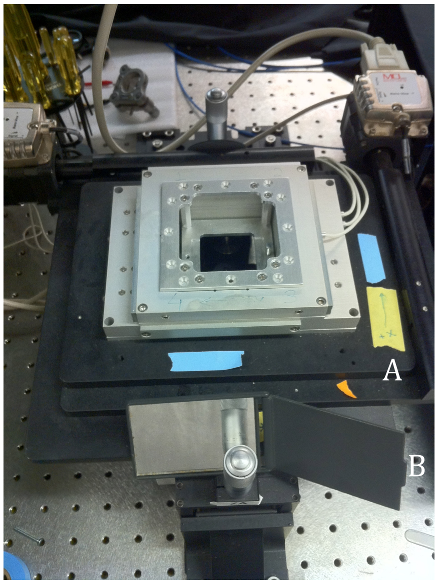

**Figure 2-7. A combination stage combining the high-speed - small range nanoscan stage with a low speed – large range microscan stage. The sample holder is placed in the central void in the nanoscan stage.**

### 2.2.5 Sample Stage

Figure 2-7 shows the setup of the sample stage, with the following components:

A. The NanoPDQ 375HS from Mad City labs was used as a sample stage. It provides a 75 um range in XY and a 50 um range in Z. It includes position sensors for absolute position measurement and sub-nanometer resolution.

B. It was used in conjunction with a motorized stepper motor driven microstage (Microstage-20E, Mad City Labs). The microstage affords a maximum range of 1” contingent on the objective lens placement. It has a two-axis stepper motor enabling a minimum step size of 95 nm in XY direction. It has a step repeatability of 50 nm. It is fitted with linear encoders with a resolution of 20 nm.

### 2.2.6 Detection pathway

Figure 2-8 shows the detection pathway setup, with the following components:

A. Fluorescent signal being omni-directional is collected using the same objective and is allowed to pass through the main optical path encountering the dichroics D1 and D2 on their way. Passing through the dirchroics enables the laser signal to get filtered out. Furthermore, to ensure high quality filtering and noise reduction of the signal, a band pass fluorescent filter (ET535/50m, Chroma Technologies) is placed in the detection pathway.

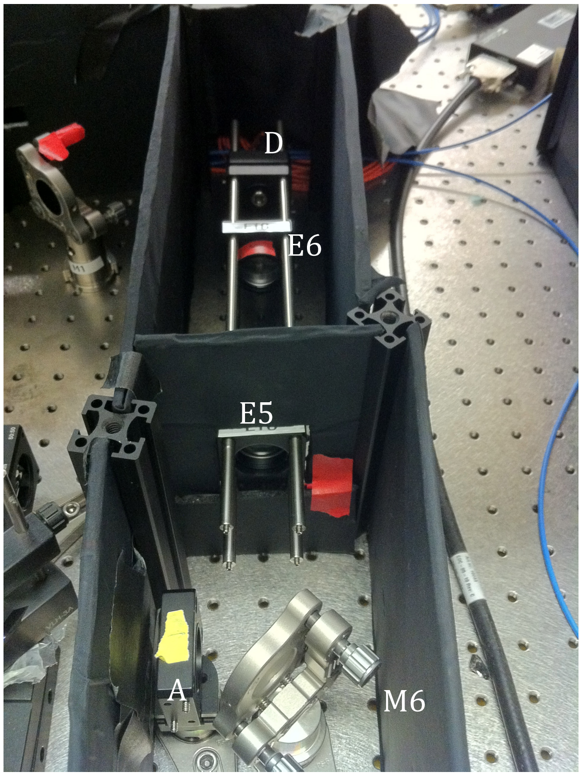

**Figure 2-8. Detection pathway consisting of a fluorescent filter that removes noise photons, improving the signal-to-noise ratio, followed by a 45° mirror that couples the signal onto a telescope that images the mirror onto a multimode detection optical fiber. A collimator focuses the signal in to the detection fiber.**

B. Mirror M6 couples the filtered fluorescent signal onto the optical detection path.
C. A telescope, consisting of achromatic doublets E5 (AC254-150-A-ML, Thorlabs) and E6, images the mirror on to a collimator.
D. A collimator couples the fluorescent photons onto the multi-mode detection fiber (M31L05, Thorlabs). In addition to carrying the signal to the detector, the fiber also acts as a pinhole effectively confocalizing the

signal. Therefore, when the system is operated with the depletion laser turned off, it's a high-end confocal microscope. Whereas, when the depletion laser is turned ON in addition to the excitation source, it's a STED imaging system.

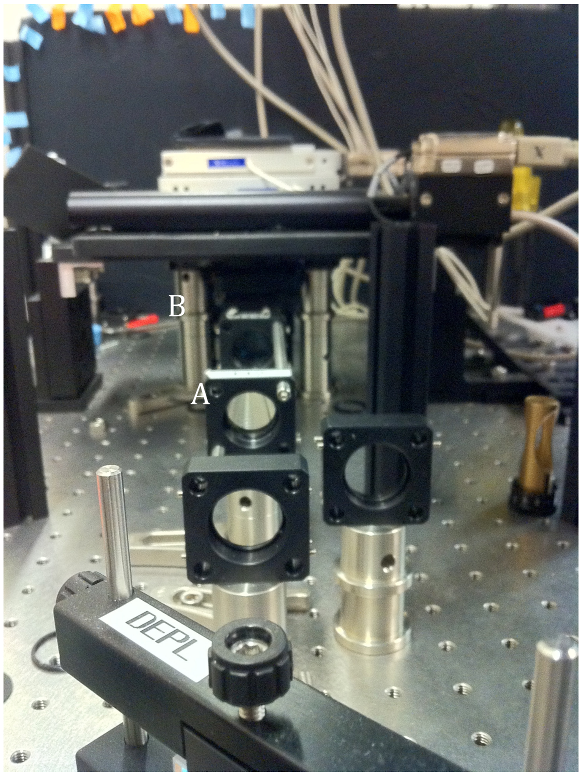

**Figure 2-9. A telescope to image the two lasers onto a 45° mirror that couples the two lasers on the objective lens**

E. The detection fiber collects the fluorescent signal and in turn delivers it to one of the two detectors that it is connected to at any given time, a PMT or an APD.

### 2.2.7 Main optical path

Figure 2-9 shows the main optical path combining both the lasers and also carrying the fluorescence signal. It is constituted of the following components:

A. Both the excitation and the depletion lasers get combined into a common beam after being reflected by their respective dichroics.

B. A telescope lens pair image the combined laser beam at the back aperture of the objective lens

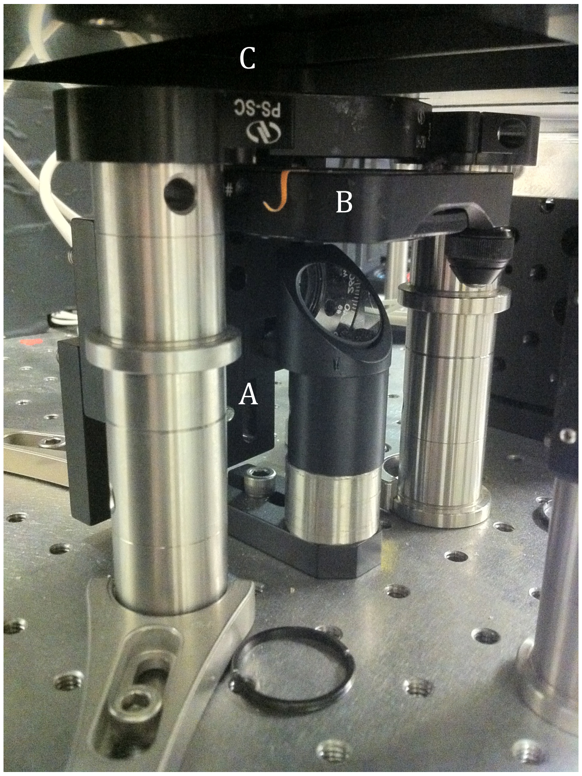

**Figure 2-10. Coupling the lasers in to the objective lens through a quarter wave-plate. Quarter wave plates enable conversion of linearly polarized light to circular polarization, ensuring all fluorophores irrespective of the orientation of their dipole would interact with the lasers.**

### 2.2.8 Coupling the lasers into the objective

Figure 2-10 shows the setup that couples the two lasers into the objective. It consists of the following components:

A. A 45° mirror changes the direction of propagation of the two lasers to be parallel with the vertical axis

B. A quarter wave plate transforms the linearly polarized laser beams into circularly polarized versions. Circular polarization ensures homogeneous laser fluorophore interaction irrespective of the orientation of the fluorophore dipole.

C. A 100x 1.4 NA objective lens focuses the lasers on to the sample plane.

D. Fluorescence being an omni-directional phenomenon, the same objective collects fluorescence signal and passes it on to the common optical path after reflecting off of the 45° mirror shown above.

## 2.3 Vibration Analysis

In order to validate the immunity of the optical system to low frequency vibrations, a damping analysis protocol was developed. Briefly, a sub-resolution gold particle sample was imaged using the excitation laser. Once found, the laser was parked at the center of the particle and the detector was initiated to collect data. Data was sampled at 5 microsecond intervals. The maximum amount of time that the data was collected for was 20 min (data not shown). Figure 2-11shows a typical plot of the data collected. It is a trace of the photon count acquired by the detector as a function of time. As the plot reveals, and is subsequently quantified in Figure 2-12, the photon count followed a normal distribution. This indicates the relative stability of the optical setup and its immunity to low frequency vibrations, such as, those caused by people walking in the corridors outside the lab.

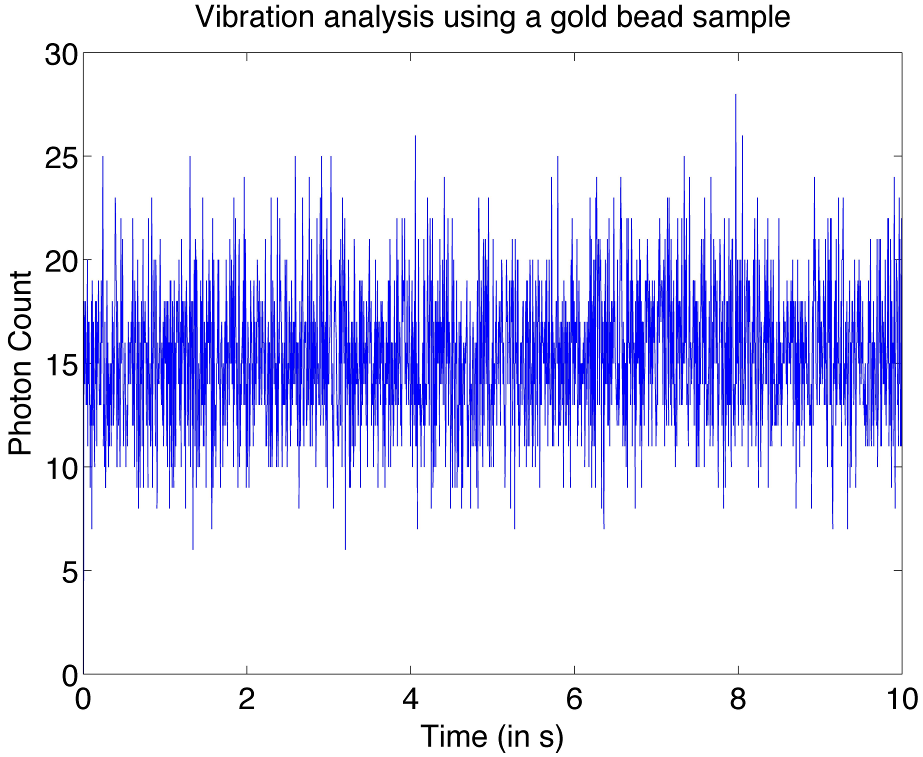

**Figure 2-11. Vibration analysis was carried out to validate immunity to low frequency vibrations. Laser was on the center coordinate of the particle and the detector was poled every 5 microseconds for a total of 10 seconds. The data suggests high degree of immunity to low frequency perturbations like pedestrians walking outside the lab, etc.**

To validate this result, we did a positive control. While the detector was still collecting photons, we tapped on the optical setup, deliberately introducing noise in the system. The detector picked up the noise signal. A spike in the photon following the tapping on the optical table was positive data confirming the validity of our previous test.

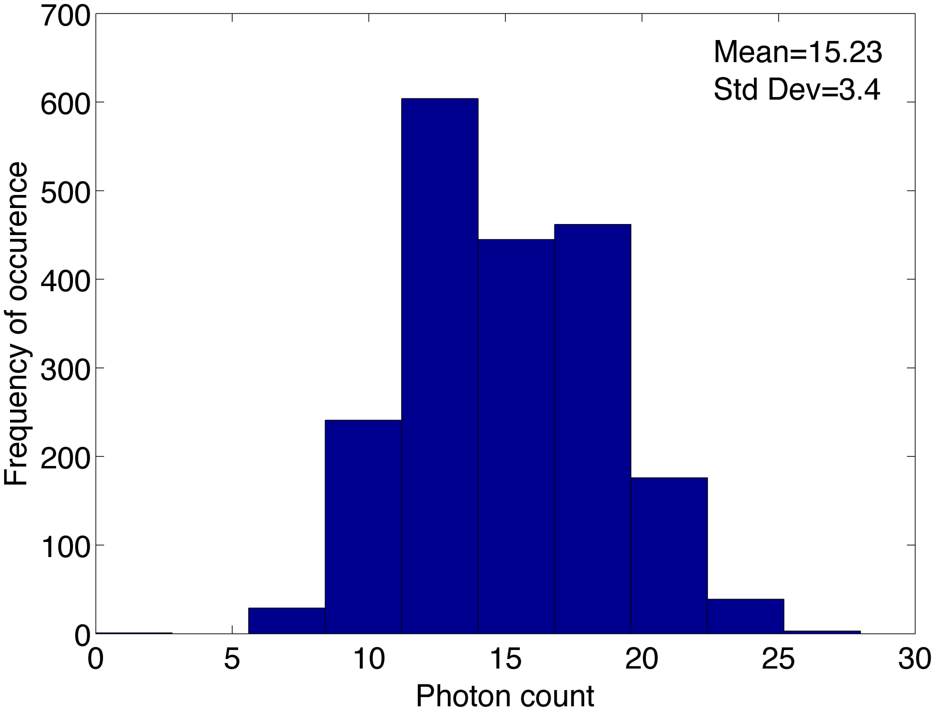

**Figure 2-12. Frequency analysis of the vibration data. Small standard deviation is indicative of high level of immunity to low frequency noise.**

## 2.4 Development of the scanning protocol

Instrumentation and control algorithms were deployed in Labview. Image reconstruction and processing were carried out through a combination of scripts developed in Labview, Matlab, and ImageJ. Raw data for confocal and STED images were compared with each other to validate the superior resolution afforded by the STED system. To achieve coarse control of the placement of the sample, the nanostage, NanoPDQ, was integrated with a microstage (MadCity Labs Inc). Various scanning protocols were employed at different stages of development of the system, to validate different aspects of the system performance.

#### 2.4.1.1 Raster scan for the Nano-stage

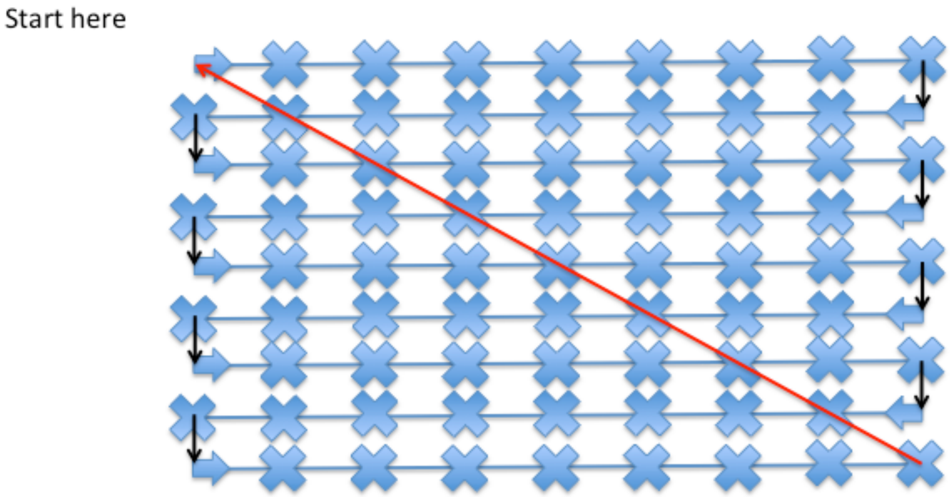

**Figure 2-13. Schematic representing development of a raster scan strategy to scan a sample on STED system. Typically, the stage starts at the origin, the point labeled, “Start here”. It moves through a horizontal line, the length of which has been assigned by the user, length of the area to be scanned. It stops at intermediate distances, pixel size, and the detector collects photons each time the stage stops. At the end of the line, it moves one “step”, y-dimension of pixel size. It repeats this process (width of the area to be scanned/y-dimension of pixel size) to collect data across the raster grid. Subsequently, an image reconstruction algorithm parses this data to reconstruct an image based on photon counts collected.**

While the micro-stage would enable coarse positioning of the sample, NanoPDQ would offer the necessary flexibility to actually image the sample. Therefore, we first implemented a conventional raster scan algorithm on the NanoPDQ as shown in Figure 2-13. Briefly, the stage were given a matrix of positions, it would stop at each position, shown by blue crosses on the scanning path schematic, it was allowed a brief settling time, the detector would collect the signal at that position, the stage would move to the next position, and the process would repeat until the stage had visited each position assigned to it by the position matrix. Black arrows on the schematic signify motion of the stage in the y direction. An important thing to note is the fact that given the relatively large time difference between each step in the y direction, motion in y axis, referred to as minor axis from now on, was not rate limiting. To increase the scanning speed of the stage, we would need to focus on improving velocity in the x direction, "major axis". The step size of the NanoPDQ, pixel size of the image, while programmable, was sub-100 nm to generate confocal data. We expected confocal resolution of ~250 nm. Therefore, sub-100 nm pixel size would satisfy the Nyquist's sampling criteria. Once the system had been validated and was ready to be used for STED imaging, the pixel size was always dictated by STED resolution. Typically, we achieved ~50 nm resolution on STED, therefore, we used 25 nm pixel size (unless mentioned otherwise for specific image datasets). To ensure appropriate comparison between confocal and STED data, both image frames were collected using the same pixel size. For faster scanning, other scanning geometries were also implemented (discussed in the apSTED section).

#### 2.4.1.2 Raster scan for the micro-stage

For the micro-stage, the scanning configuration was similar to the one used with NanoPDQ with the following differences. As in the case with the nanostage, the microstage was also given a matrix of positions, as shown in Figure 2-14. However, the minimum step size for the micro stage was 50 microns. The range of the nanoscan was 50 microns in xy axes. Therefore, the minimum step size required on the microstage was 50 microns. Furthermore, the microstage polls the nanostage for a hand-shake signal. Each time the nanostage finishes a scan; the microstage would move to its next position. Unlike the nanostage scans, patterns used for microstage scanning were always rectangular.

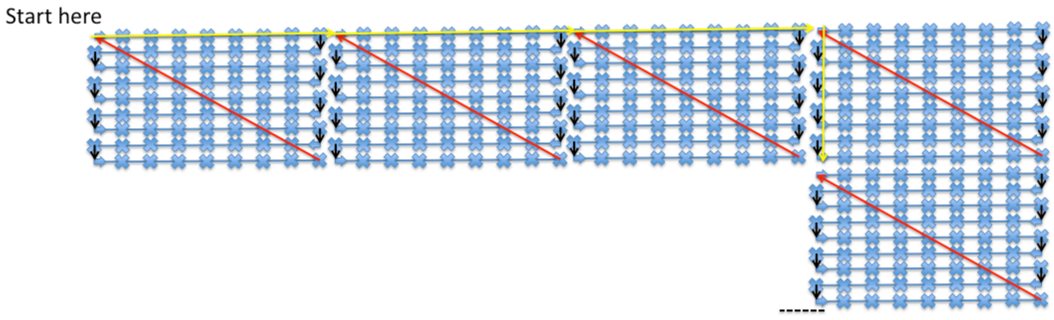

**Figure 2-14. Microstage and nanostage have been programmed using multiple hand-shake signaling protocol. Once the nanostage finishes a scan (shown in blue), it goes back to its original (0,0) position. After it reaches the origin, it relays a hand-shake signal to the microstage enabling it to move one 'step' (of predetermined dimension >50 microns). Repeating this over a large area allows the system to reconstruct larger area image.**

## 2.5 System validation for STED

Coarse alignment of the system was achieved by utilizing pinholes at different points of the system. 1 micron pinholes were placed at different spots in the optical paths and the lasers turned on sequentially. In an event of misalignment, the laser would not pass through a specific pinhole and the absence of laser at any of the checkpoints provided the identification of a problem spot. Beyond the common optical path, there wasn't enough physical space to ensure alignment. To circumvent this shortcoming, we adapted an alignment protocol (based on a discussion with Hell lab). Specifically, we developed a ~20 inch long alignment tool, Figure 2-15, made with pinholes placed at the two ends of the tool. We removed the objective lens and screwed the alignment tool in lieu of the objective at the objective holder. Given the length of the alignment tool and the size of the two pinholes used, the lasers would pass through the tool only if it were aligned reasonably well and was collimated. Therefore, a passage through both the pinholes of the alignment tool and presence on the other side of the tool on a "screen" was considered positive proof for high degree of coarse alignment.

Following coarse alignment of the two lasers, to achieve alignment with a high degree of accuracy, we scanned sub-resolution (~80 nm) gold particle samples using both lasers sequentially. Samples were prepared using the following protocol:

1. ~4.5 g PVA 4-88 was dissolved in water
2. Stirring and heating to ~50 C was used to increase the efficiency of dissolution and also to improve the speed significantly
3. Gold colloids (80 nm, British Biocell) were sonicated for 10 min
4. 20 uL of gold colloid was pipetted into an eppendorf cup and diluted with 200 uL of PVA solution
5. 100 uL of solution in (4) was dispersed onto a coverslip and spincoated at 4000 rpm for 30 sec. Spincoating ensured a uniform film of particles

6. Sample was allowed to dry in a dessicator overnight
7. Subsequently the coverslip was mounted with immersion oil onto a microscope slide and was glued using nailpolish

**Figure 2-15. Alignment tool for coarse alignment of the system. The alignment tool is ~20 inches in length. Small diameter pinholes are placed at either ends of the pinhole. It is placed in place of the objective lens and the lasers are allowed to pass through the two pinholes to confirm optimal alignment.**

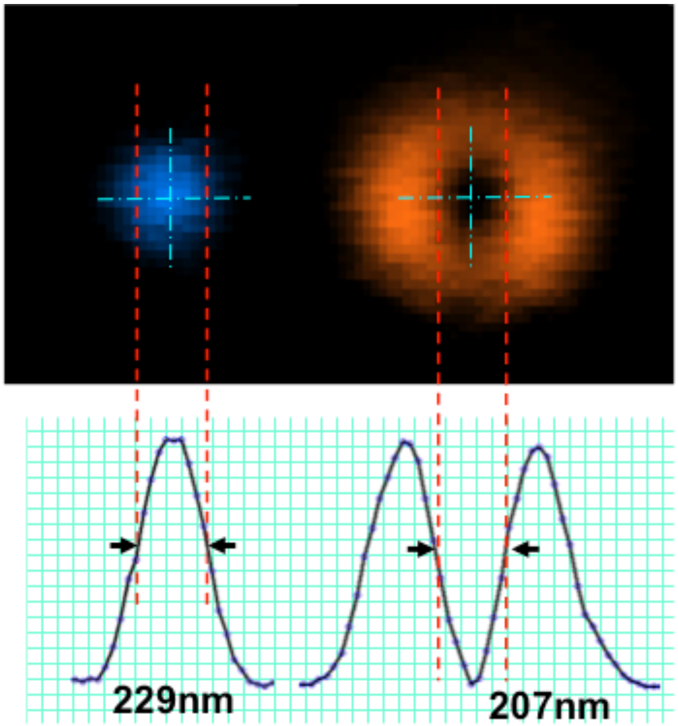

**Figure 2-16. Images of sub-diffraction gold beads (~80 nm) using both lasers sequentially. Line profiles of the center of the images indicate the dimensions measured using both lasers. System was aligned to achieve super-imposition of the centroids of the two images**

Gold beads were imaged in a reflection mode setting i.e. the fluorescence filters were removed from the detection pathway. The target was to image the gold beads using the excitation laser as shown on the left in Figure 2-16. Subsequently, image the same bead using the toroid shaped depletion beam, as shown in the right panel of Figure 2-16, and implement the necessary optical alignment adjustments to superimpose the center of the 'donut' with the center of the excitation bead scan. This would ensure alignment of the two lasers with a high degree of accuracy.

### 2.5.1 Toroid engineering

One of the primary determinants of the quality of the toroid is the polarization of the depletion laser beam. Initial scans revealed that the toroids were imperfect at the focal plane. Vortex phase masks essentially function by inducing destructive interference at the center of the donut and constructive interference on the outer periphery. However, the efficiency of this phenomenon depends on circular polarization of the laser beam. To ensure high degree of circular polarization, we included a quarter wave plate right underneath our objective lens. Furthermore, using the donut scans as a feedback, we manipulated the orientation of the quarter wave plate to improve the “circularity” of the beam polarization. We also included half wave plates at the output of the laser beams to ensure near “perfect” linear polarization of the laser before it hit the quarter wave plate placed at the back aperture of the objective lens.

Scanning sub-diffraction gold beads was used as a feedback to evaluate the quality of the torus. To improve the shape and energy distribution across the toroid shape, the centering of the laser was adjusted on the phase plate.

The fluorophore best suited for the laser wavelengths that we had selected was Oregon Green 488. Therefore, in order to quantify the resolution of STED, we prepared a sample by immobilizing Oregon Green 488 on a cover glass with thickness ~170 micron. Sample was prepared using the following protocol:

1. Sonicate the fluorophore sample for 15 min. Dilute antibody in PBS (~1:10000)
2. Sonicate again for 15 min
3. Clean a cover slip with ethanol
4. Coat the coverslip with poly-L-lysine for 10 min
5. Wash off the cover slip and blow dry using air or nitrogen
6. Pipette a drop (~20 uL) of the solution on the coveslip
7. Allow the fluorophores to attach to the surface (~15 min)
8. Repeat the wash and dry cycle as (5)
9. Add a drop of TDE (~20 uL), press cover slip on microscope slide and seal with nail polish

Subsequently, we imaged the sample both under a confocal mode and a STED mode. A typical set of images is shown in Figure 2-17. The improvement in resolution can be better appreciated from the inset, zoomed-in version, of the images. Particles that appear as clusters on the confocal scan can clearly be differentiated on the STED image. A comparison of full-width-at-half-maximum of intensity profiles of a single particle, shown in Figure 2-17(B), reveals the resolution achieved by STED to be ~50 nm, a >4-fold improvement over that achieved by confocal, ~230 nm.

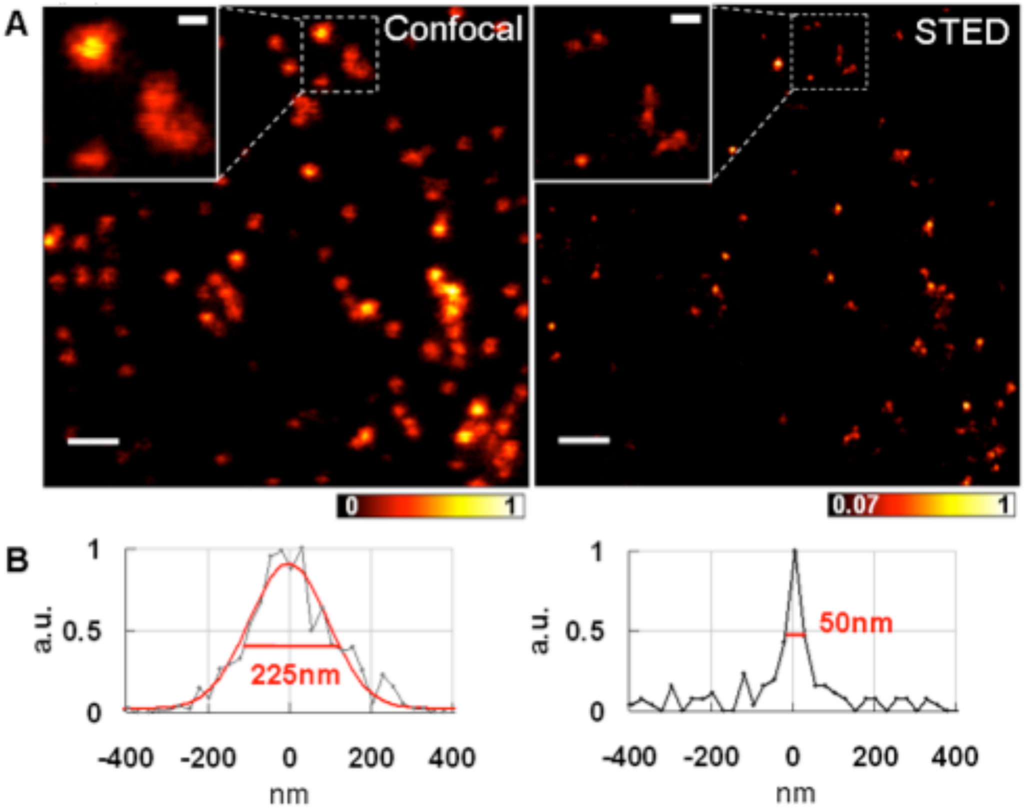

**Figure 2-17. Side by side comparison of confocal and STED image data from a calibration sample. Samples were prepared by immobilizing Oregon green 488 on glass coverslips. Line scans reveal improvement in resolution from ~230 nm to ~50 nm, >4-fold improvement.**

## 2.6 apSTED Microscopy

While a STED system does afford a superior resolution compared to conventional imaging systems, it achieves this using a high-powered depletion laser source. This translates into a need for shorter pixel dwell times in order to avoid severe photobleaching and phototoxicity to cells under study. Several techniques have been proposed in the past to increase the scanning speed of fluorescence microscopes. While each of these strategies has its own set of pros and cons, we endeavored to build a system of our own, affording us the maximal flexibility and access to on-the-fly changes to the scanning algorithms.

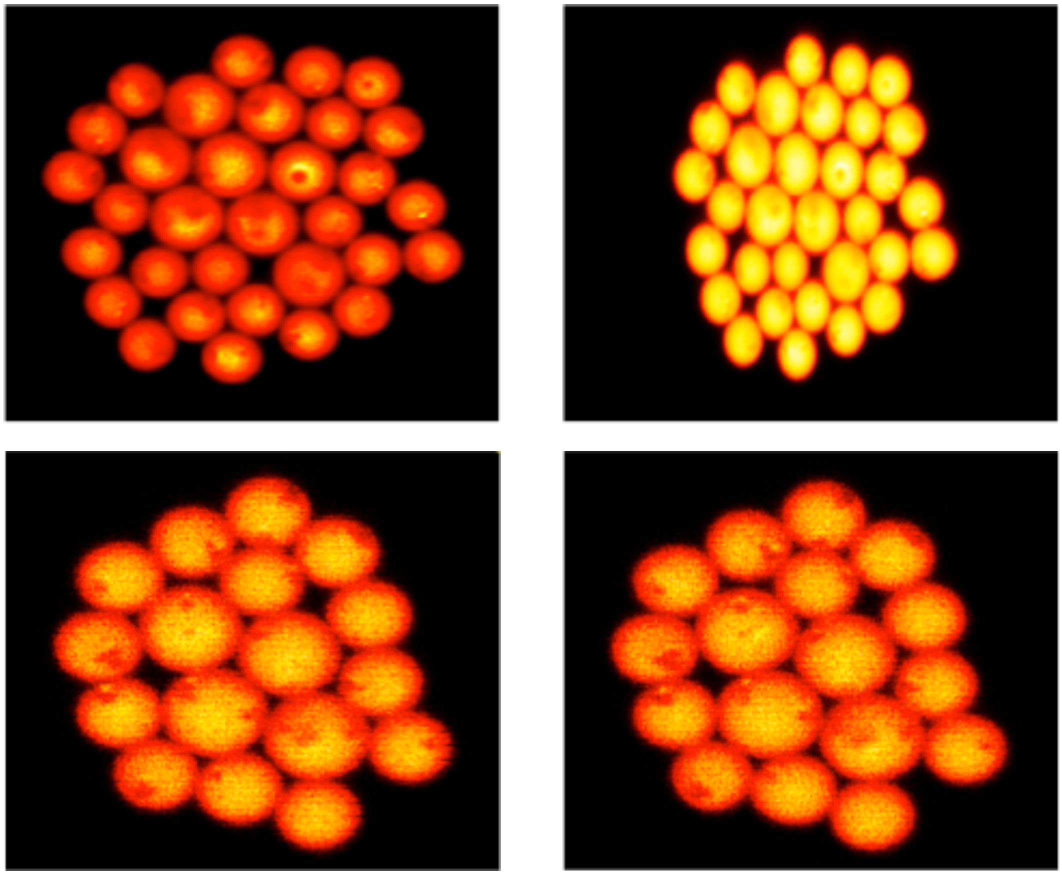

**Figure 2-18. Comparison of fluorescence bead calibration sample without and with accelerated piezoelectrically driven stage motion for STED. Left image was taken using slow scanning frequency ~170 Hz. The right image was collected at high frequency ~10KHz and the image was distorted. (B) Demonstration of the advantage of apSTED. Left is slow scan and right image was collected at ~10 KHz with no appreciable difference between the two images.**

To circumvent the challenge of photobleaching at the sample due to high depletion laser intensities, a fast scanning strategy was implemented by accelerating the piezoelectrically driven sample stage at super-optimum operating frequencies. Accelerating the stage, however, introduced system lag. This translated into images with shifts between subsequent scan lines as shown in Figure 2-18. To overcome this shortcoming, various scanning algorithm improvements (accelerations) were implemented (described in subsequent sections). Utilizing this strategy, ~10-fold increase in scanning speed for the STED system was achieved. Being accelerated through piezoelectric drive, we called the system apSTED. Resolution achieved using apSTED was similar to the resolution achieved through conventional STED, ~50 nm. However, the photobleaching rate, ~10%, was significantly better than the ~80% photobleaching rate on conventional STED system.

### 2.6.1 Sinusoidal scan algorithm

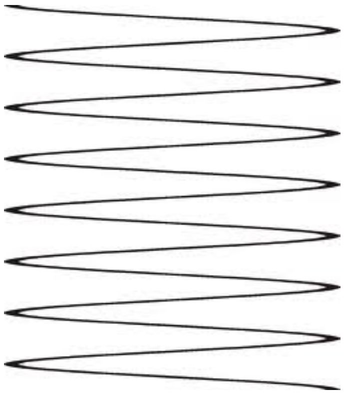

**Figure 2-19. Variation on the scanning algorithm. To avoid system lag in responding to command, we modified our rectangular scanning algorithm to a sinusoidal scan.**

In order to increase the scanning speed of the stage, we needed to enable smooth, linear motion of the stage at high speed. Detailed analysis revealed that the increased speed would have the most detrimental effects on the stage's performance at the end points of a scan line because of the abrupt change in direction that it experienced at the two ends. Therefore, to avoid this, as shown in Figure 2-19, we adapted our algorithm to use a sinusoidal scanning protocol in lieu of the rectangular protocol preferred by conventional STED implementations.

### 2.6.2 Uni-directional data collection

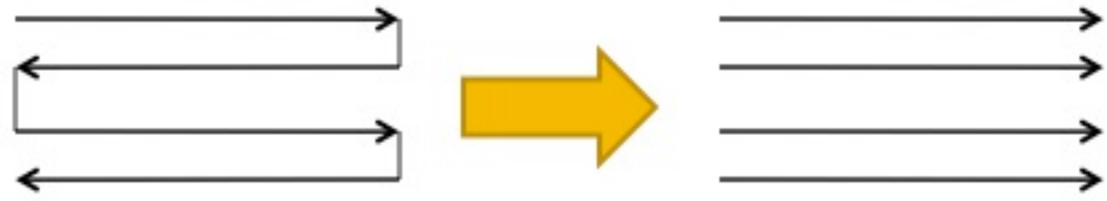

**Figure 2-20. A unidirectional scanning strategy as opposed to the initially implemented bidirectional scanning, circumvented the non-linearity in motion that the stage suffered at the end-points of a scan line while changing direction of motion.**

An analysis of the stage response corresponding to the command signal underscored the linearity of the stage moving forward following the sinusoidal curve. However, the stage response on its journey on the "back" path was not linear. Broadly, this was because the piezoelectrically stage was driven by voltages. Therefore, the forward motion was governed by a signal that went from 0 to full voltage (full voltage varied by the range of the scan area). The stage had to turn around after reaching the end of the scan line (maximum voltage), and travel “back” in the other direction. This turn around event introduced phase lag in the stage, which resulted in a non-linearity in its motion in the “back” direction. To circumvent this shortcoming, and to quicken the stage motion further, as demonstrated by a schematic in Figure 2-20, we decided to record data only during the “forward” motion of the stage, and during the “back” motion just change the applied voltage to zero, enabling fast stage motion in the “back direction”. This allowed us to increase the scanning speed significantly.

### 2.6.3 Time based detection in lieu of position based detection

While sinusoidal scans enabled an increase in scanning speed, it was still not able to mitigate the photobleaching challenge completely. To improve the scanning efficiency further, we chose time-based detection in lieu of position-based detection. As described in the previous sections, our raster scanning strategy was based on the stage stopping at several intermediate points on a scan line and the detector collecting data once the stage had reached steady state position i.e. all the transients had died down. However, the settling time for the stage would offer a bottleneck to increasing the scanning speed. Therefore, we updated the scanning algorithm to enable the stage to move to the end of the scan line at high speed. Instead of collecting position-encoded data, we implemented time-encoding data protocol. Data was collected at several time points while the stage moved from one end to the other on its scan line and the data was subsequently assigned to specific spatial coordinates based on its time coordinate with respect to the beginning of the scan line. This enabled us to collect data at high speed without stopping the stage at any point in its travel.

Taken together, all the improvements reported in the previous three sections resulted in a scanning speed improvement of >~10-fold. We went from about 170 digitizations with a basic raster scanning algorithm to ~10,000 digitizations once all these upgrades were implemented. This enabled us to largely side step the issue of photobleaching, which fell from ~80% to ~10% enabling us to perform meaningful biological imaging studies.

## References:

1. Hell, S. Strategy for far-field optical imaging and writing without diffraction limit. *Physics Letters A* (2004).
2. Harke, B., Medda, R. & Hell, S. STED microscopy with continuous wave beams. *Nat Methods* (2007).

# 3 Structural and Functional Basis of Primary Cilia

Despite it’s discovery in 1898, primary cilium had been considered a vestigial organ until recently. However, more recent work has identified its role in maintenance of several critical homeostatic functions in mammalian biology, cellular signaling, as a sensor for various cell types, and a mediator of myriad chemo-mechanical signaling pathways.

Of particular interest is to note the role of primary cilia structure. Typically, the morphology of primary cilia, and changes occurring in its morphology, has been correlated with its ability to mediate different signaling pathways. Specifically, a decrease in length of primary cilium has been correlated with a reduction in sodium currents. McGlashan et al. showed that the length of primary cilia decreases in response to an overloading of chondrocytes[1]. Their study further demonstrated an increase in primary cilia length corresponding to deprivation of this stress on chondrocytes. Resnick et al. reported a 60% decrease in epithelial sodium channel (ENaC) current corresponding to a 30% decrease in primary cilia length under shaking induced fluid flow conditions[2].

## 3.1 Imaging primary cilia

The first step to developing imaging based assays to study primary cilia was to setup a protocol to label various elements of primary cilia. As a first step, we adapted an immunolabeling protocol proposed previously. Specifically, we used Hoechst labeling to identify the nuclei of the cells. Furthermore, we labeled acetylated tubulin (Ac-Tub) to identify the axonemal structure of primary cilia. An important factor to consider is the fact that, while it is concentrated higher in the axoneme of primary cilia, Ac-Tub is not exclusive to primary cilia. It labels other cyto-skeletal structures of the cells as well. Therefore, for definitive identification of primary cilia, we also labeled pericentrin, a molecule expressed at high levels in centrosome. Given that the basal body of primary cilia originates from the mother centriole, a localization of Ac-Tub with pericentrin was considered positive identification of primary cilia. Figure 1 shows a typical data set collected using this protocol.

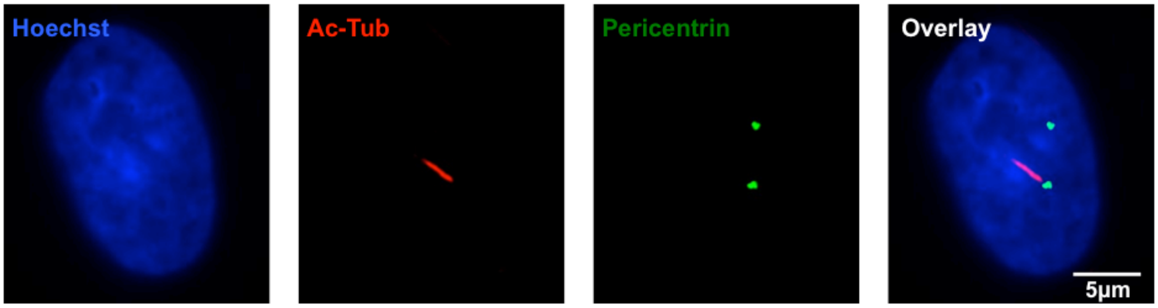

**Figure 3-1. Immunostaining assay to identify primary cilia on Human Foreskin Fibroblast (HFF-1) cells. Hoechst staining (blue) was used to identify nuclei of the cells. Ac-Tub (red) labeling identified the axonemal structure of primary cilia. Pericentrin (green) labeled the centrioles of the cells. Close vicinity localization of Ac-Tub to pericentrin was considered positive identification of primary cilia.**

### 3.1.1 Experimental protocol

#### 3.1.1.1 Cell culture

1. Human foreskin fibroblast (Hff-1) cells were cultured on #1.5 glass cover slips, at a seeding density of 150,000 cells, using Dubelco’s Minimum Essential Media (DMEM) supplemented with 15% Fetal Bovine Serum

(FBS), 1.5% Hepes buffer, 1.2% Penicillin-Streptomycin and 1.2% 2mM L-glutamine at 37 C and 5% CO2.

2. The above stated media recipe was called serum-enriched media for Hff-1 cells
3. Serum-deprived media was prepared following the recipe mentioned above with the exception of FBS.
4. Once the culture reached ~95% confluence, media on the culture was changed to serum-deprived state.

#### *3.1.1.2 Fixation/immunostaining*

1. After serum deprivation either for 24 or 48 hours, cells were perfusion-fixed using 5% Paraformaldehyde (PFA) for 12 minutes.
2. Samples were then washed twice with Phosphate Buffer Saline (PBS)
3. PBS washes were followed up with permeabilization with 0.2% PBS-Triton (PBST) for 10 min.
4. After permeabilization, samples were blocked using 10 % normal donkey serum, at room temperature for 1 hour.
5. Cells were incubated with primary antibodies; mouse monoclonal antibody to Acetylated Tubulin (Ac-Tub) (ab24610, Abcam) diluted 1:2000 and rabbit polyclonal antibody to pericentrin (ab4448, Abcam) in the blocking solution overnight at 4 C
6. Next day, cover slips were washed with PBST (3x) before being incubated with donkey anti-mouse Alexa Fluor 568 secondary (Invitrogen) and

donkey anti-rabbit Alexa Fluor 488 antibodies diluted in the same blocking solution at room temperature for an hour

7. Post secondary antibody incubation, the samples were washed with PBST (3x)
8. Subsequently, samples were incubated with Hoechst, 1:100 dilution in PBS, for 10 min to label the nuclei of the cells
9. Hoechst staining was followed by PBS washes (3x)

#### *3.1.1.3 Imaging*

1. Sample cover slips were mounted on glass slides using, non-fluorescent and fast drying nail polish, as a sealant.
2. Samples were imaged through the coverslip using a 100x, 1.4 NA objective (Olympus) on an inverted epi-fluorescence microscope (IX-81, Olympus)
3. Hoechst channel was imaged using EX: 387/11 and EM: 447/60 filter set (DAPI-1160A-OMF-ZERO, Semrock Inc.) coupled with a dichroic DM: 409 (Semrock Inc.)
4. Pericentrin channel was imaged using EX: 500/24 and EM: 542/27 filter set (YFP-2427A-OMF-CUST-ZERO, Semrock Inc.) coupled with a dichroic DM: 520 (Semrock Inc.)
5. Ac-Tub channel was imaged using EX: 562/40 and EM: 624/40 filter set (TXRED-4040B-OMF-CUST-ZERO, Semrock Inc.) coupled with a dichroic DM: 601 (Semrock Inc.)

6. Images were collected using a CCD camera (C8484-05C, Hamamatsu) with a 1344 x 1024 sensor chip and a 6.45 $\mu m^2$ cell size.
7. Images were collected from individual channels before data from these channels were merged to generate overlays.
8. The plane of focus for individual channels, corresponding to the nucleus, axoneme of primary cilia and basal body of the primary cilium, were observed to be slightly different from each other.
9. In order to prevent double counting of cells, if the focal plane varied by >10μm, those primary cilia were not considered for analysis.

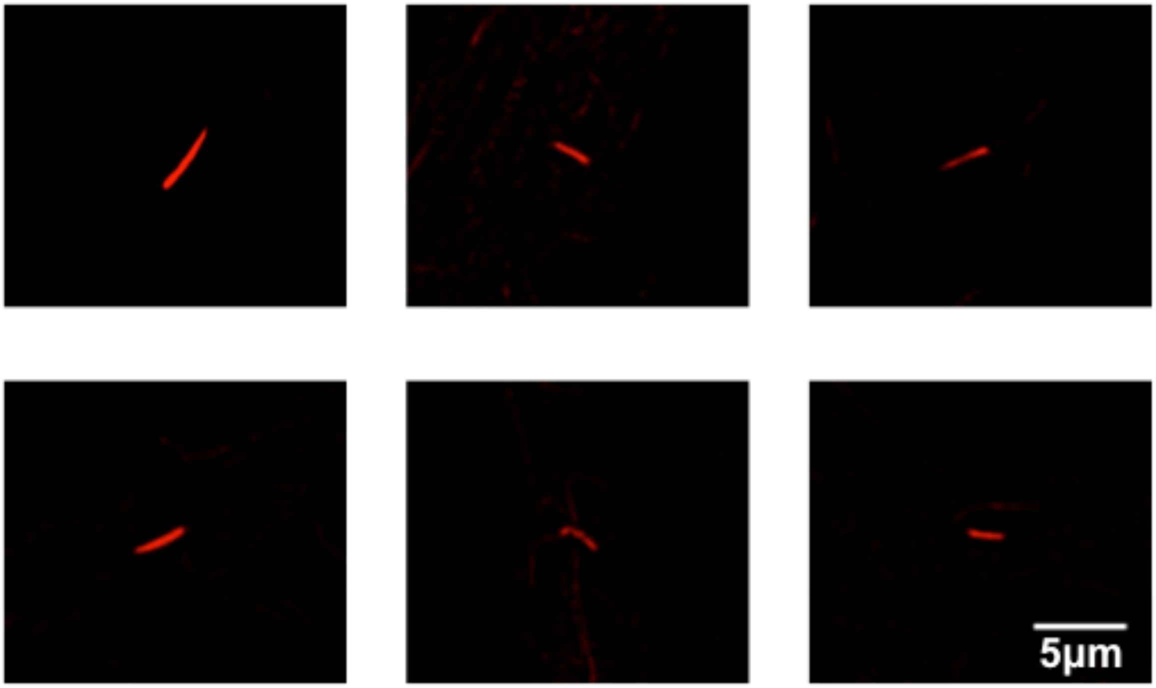

**Figure 3-2. For morphometric analyses, primary cilia images were extracted from the multi-dimensional image data sets. Thresholding was used to clean the image data set. Shown in the figure are a few representative**

**primary cilia images that were collected from 24 hour serum deprived Hff-1 cells for further analysis.**

#### *3.1.1.4 Image processing*

1. Images were imported into imageJ
2. Images were thresholded <5% to improve the signal-to-noise ratio (SNR).
3. Image overlays were generated in imageJ
4. Length of primary cilia were measured using a built in imageJ length measurement tool

## 3.2 Validating the functional state of primary cilia

One of the most significant tasks of primary cilia is to mediate myriad signaling pathways[3]. Amongst the different pathways mediated by primary cilia, hedgehog is one of the more critical pathways[4]. Sonic hedgehog (Shh), one of three prominent members of the hedgehog family, is one of the better-studied ligands of the family. Its importance is underscored by the role it plays in organogenesis[1,5], including in the growth of digits of the limb and the organization of the brain. In adults, it has been shown to contribute to cell division and differentiation of adult stem cells[2,6], and in development of certain types of cancers[3,7-11]. The downstream effect of Shh signaling is the activation of transcription factor family, Gli, which in turn coordinates tissue patterning. The interaction of Shh with Gli is mediated through a pair of transmembrane proteins, Smoothened (Smo) and Patched (Ptc). In the absence of signaling, Smo is maintained in an inactive state by Ptc. Furthermore, Gli also remains repressed. Conversely, in the presence of signaling, Ptc in unable to suppress Smo, which in turn produced Gli activators, which are responsible for the optimal execution of Hh signaling pathway. Details of this pathway have been reported in detail in this review[4,12]. Recent studies have established a prominent role for primary cilia in the mediation of this pathway[12,13]. Specifically, Shh receptors have been shown to localize at the base of primary cilia. In the absence of Shh, according to models proposed by several studies, Smo is present on intracellular vesicles and Gli proteins processed in their repressive forms at the tip of primary cilia. In response to Shh signaling, Ptc is pushed out of the primary cilia structure, therefore, no longer prohibiting the entry of Smo. Subsequently, Smo enters primary cilia and interacts with the Gli protein machinery to activate Gli. Gli activators are believed to subsequently leave the cilium and enter the nucleus to coordinate the activation of Hh-dependent genes[12].

In order to validate the functional state of primary cilia, we undertook a study involving stimulation of primary cilia. Specifically, we used SAG, a potent Smoothened (Smo) agonist to simulate the activation of the Shh signaling pathway.

### 3.2.1 Validation of presence of ptc on primary cilia

1. To validate the presence of primary cilia, cell cultures were prepared as described in the previous section.
2. A modified immunostaining protocol was used to label ptc and ac-tub on cells

3. Briefly, after serum deprivation either for 24 or 48 hours, cells were perfusion-fixed using 5% Paraformaldehyde (PFA) for 12 minutes.
4. Samples were then washed thrice with Phosphate Buffer Saline (PBS)
5. Cells were incubated in -20°C methanol for 5 minutes and subsequently washed with PBS (3x)
6. PBS washes were followed up with permeabilization with 0.2% PBS-Triton (PBST) for 10 min.
7. After permeabilization, samples were blocked using PBST containing 2% Bovine Serum Albumin (BSA) and 1% normal donkey serum, at room temperature for 1 hour.
8. Cells were incubated with primary antibodies; mouse monoclonal antibody to Acetylated Tubulin (Ac-Tub) (ab24610, Abcam) diluted 1:2000 and rabbit polyclonal antibody to patched1 (sc-9016, Santa Cruz Biotechnology Inc.) in the blocking solution overnight at 4 C
9. Next day, cover slips were washed with PBST (3x) before being incubated with donkey anti-mouse Alexa Fluor 568 secondary (Invitrogen) and donkey anti-rabbit Alexa Fluor 488 antibodies diluted 1:2000 in the same blocking solution at room temperature for an hour
10. Post secondary antibody incubation, the samples were washed with PBST (3x)
11. Samples were imaged as described in the previous section

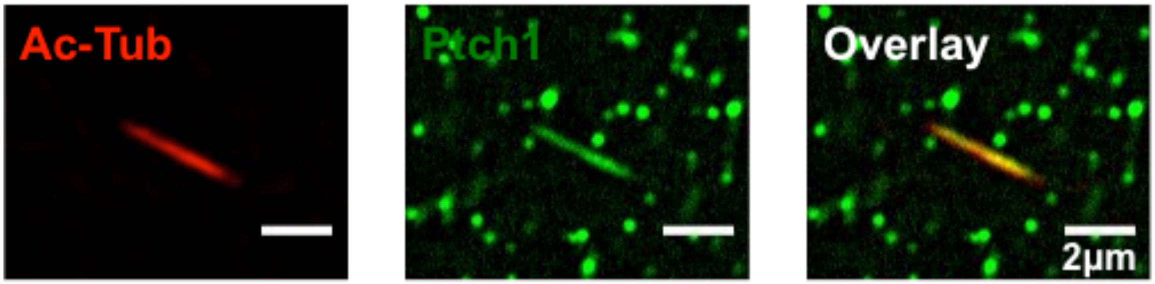

**Figure 3-3. Hff1 cells were labeled for Ac-Tub and Ptch1. Samples were imaged under 100x magnification. This is a representative set of images. As demonstrated, Ptch1 stain seemed to completely overlap Ac-Tub, implying the presence of Ptch1 in the primary cilia structure.**

As shown in figure 3-3, our data indicate almost perfect overlap in Ptch1 and Ac-Tub images. Confirmation of overlap in these two channels was consistent with studies reporting the presence of Ptch1 inside the primary cilia structure.

To confirm the functional state, next we repeated the experiment following essentially the same protocol with a few changes. Before fixing cells, we stimulated them using 1 μM SAG, a small molecule Smo agonist. Stimulating the cells with SAG for 4 hours resulted in a complete removal of Ptch from the primary cilia body confirming the functional status of primary cilia.

### 3.2.2 Smo in the context of primary cilia

Functional primary cilia mediate the Shh signaling pathway as described in the previous section. As a more stringent validation of the functional status of primary cilia and their ability to mediate the said pathway, we also studied the localization of Smo inside the axonemal structure of primary cilia. Briefly, we cultured and fixed Hff1 cell samples as described in 3.1.1.1 and 3.1.1.2. Donkey anti-rabbit antibody against Smo (sc-13943, Santa Cruz Biotechnologies Inc.) and donkey anti-mouse antibody against Ac-Tub were used to label the cells following the same immunostaining protocol. When the cells were not exposed to SAG, control experiment, we found no localization between Smo and Ac-Tub., as shown in figure 3-4.

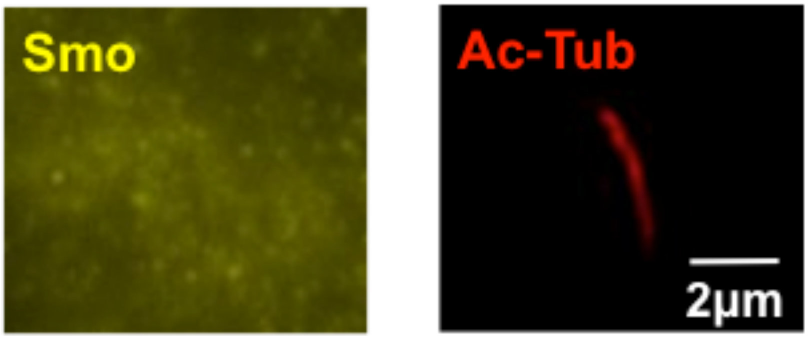

**Figure 3-4. Hff-1 cells stained for Smo and Ac-Tub. Cells were imaged in their nascent state, no SAG stimulation. Our data suggests, in absence of SAG stimulation i.e. in absence of activation of Shh pathway, Smo is unable to enter the axonemal structure of primary cilia. Together with data shown in figure 3-3, this data confirms the canonical model of homeostatically functional primary cilia, i.e. if the Shh pathway is not stimulated, Ptch1 is localized inside the axonemal structure of primary cilia, which prevents the entry of Smo in, therefore, inhibiting the downstream effectors of Shh signaling pathway.**

Stimulation of Hff-1 cells with SAG for a period of 4 hours, however, resulted in entry of Smo into the axonemal structure of primary cilia. As shown by a representative image data set in figure 3-5, Smo localized well with Ac-Tub on Hff-1 cells stimulated with SAG for 4 hours. Taken together with the Ptc data, this set of experiments underscores the functional status of primary cilia on Hff-1 cells. It also provides validation for the proposed model of primary cilia functionality, which states that when the Shh signaling pathway is activated Ptc is pushed out from the primary cilia and Smo is pushed in. In addition to this imaging based study, we also undertook a biochemical study to determine expression levels of various players participating in Shh mediation pathway. Results of that study are reported as a part of chapter 4 in this document.

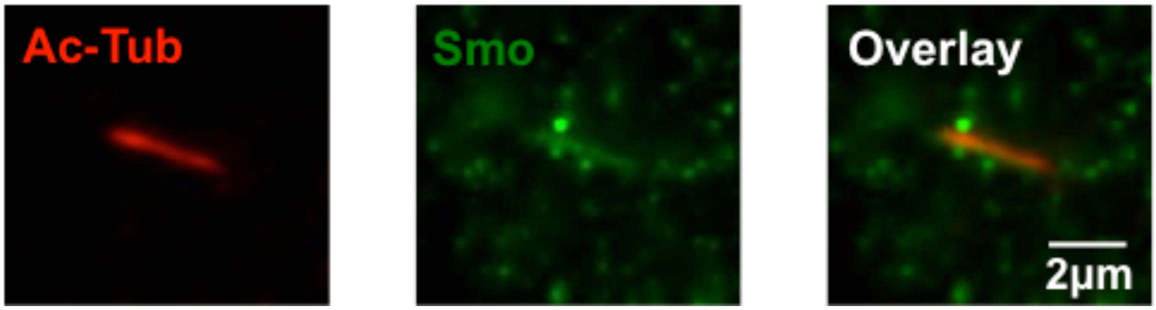

**Figure 3-5. After 4 hours of SAG stimulation, labeling Hff-1 cells with Ac-Tub and Smo reveals almost perfect localization of both. This result is indicative of the homeostatic functional status of primary cilia on Hff-1 cells.**

## 3.3 Transition zone

One of the most prominent structural elements of a primary cilium is the transition zone. Briefly, recalling the structure of primary cilia, it originates from the mother centriole, the older of the two centrioles in the cell. The process of ciliogenesis begins with the attachment of a vesicle to the distal end of the basal body. Centriolar distal appendages provide the necessary anchoring to the vesicle to dock onto the basal body. In the context of primary cilia, these centriolar distal appendages are also sometimes referred to as transition fibers. Subsequent to docking of the vesicle, a bud emerges from the basal body. The tip of the bud elongates to give rise to the axoneme of primary cilia. However, the base of the bud remains structurally different from the tip and goes on to form "transition zone". Details of these structures are more thoroughly reviewed in this study[12]. Structurally, transition zone appears to be one of the most significant components of primary cilia. This is a result of the fact that there is no protein synthesis inside primary cilia. Therefore, material going in and out of the primary cilium is the only mechanism that would ensure structural integrity and functional viability of primary cilia. However, the outer membrane of primary cilia is contiguous with the plasma membrane of the cell. Therefore, transition zone provides the physical site of discriminating against cytosolic proteins and allowing only proteins associated with structure/function of primary cilia to enter the ciliary body.

Given that the morphology of primary cilia structure governs its signal transduction function, it is necessary to elucidate the structural components of primary cilia. Studying the transition zone would provide first order information regarding material going in and out of primary cilia. Therefore, we initiated a project to study various transition zone components of primary cilia.

Abnormalities in the structure of primary cilia have been correlated with several tissue-development disorders. Such abnormalities are broadly classified as ciliopathies[14]. Nephronophthisis (NPHP), Joubert Syndrome (JS), and Meckel-Gruber Syndrome (MKS) are three such ciliopathies. These ciliopathies result in devastating effects on the quality of life of an individual[15-17]. Systematic study[18] of various components of primary cilia has revealed a family of molecules, NPHP, to play a critical role in these ciliopathies. In certain cell types[18-21], NPHP has been shown to localize exclusively at the transition zone.

### 3.3.1 NPHP4 in the context of Hff1 cells

NPHP4 has been identified as an important member of the NPHP family. We undertook an immunostaining study to observe NPHP4 at the transition zone of primary cilia. We followed the cell culture and fixation protocols as described in 3.1.1.1 and 3.1.1.2. Furthermore, we followed the immunostaining protocol as described in 3.1.1.3 with the following exception. We used rabbit polyclonal antibody against NPHP4 (13812-1-AP) in conjunction with the mouse monoclonal antibody against Ac-Tub described previously. Imaging was carried out using an Olympus IX-81 following the same protocol as described previously. Given the location of transition zone at the base of primary cilia, intuitively, we anticipated the presence of NPHP4 at one of the two ends of primary cilia. However, counter-intuitive to expectations, our data suggests that in addition to the transition zone, NPHP4 leaks into the axonemal structure of primary cilia on Hff1 cells. Repeating the experiment with different dilutions of antibodies, or depriving the cells of serum for times ranging from 24-48 hours, did not have any effect on the qualitative nature of the data. Absolute brightness of the images, a measure of the number of fluorophores labeling the cilium structure, changed with changes in the dilution of antibodies. But qualitatively the data remained similar.

While there is strong evidence to underscore the role of NPHP4 at the transition zone of primary cilia, we are unaware of any previous studies reporting a functional role of NPHP4 in the axonemal structure of primary cilia. While our data is exciting, and repeatable, given the counter-intuitiveness of results, we are doing follow up work to elucidate completely the implications of this finding. It remains to be seen if the leaking of NPHP4 in the axonemal structure of primary cilia on Hff1 cells plays a functional role or if some previously unseen molecular structural defect at the transition zone unwittingly allows the entry of NPHP4 inside.

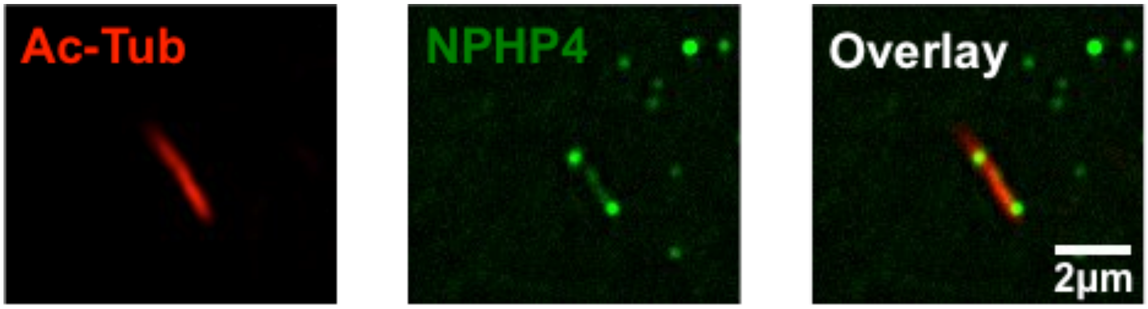

**Figure 3-6. Hff1 cells were immunostained with antibodies against Ac-Tub and NPHP4. Consistent with previously suggested models, NPHP4 does localize at the base of primary cilia i.e. localizes at the transition zone.**

**Additionally, our data suggests, small amounts of NPHP4 “leaks” into the axonemal structure of primary cilia.**

### 3.3.2 TCTN2 and Cep290 – potential targets for apSTED

Tectonic proteins have very recently been identified as an important and integral part of primary cilia transition zone[22]. Tectonic family proteins are evolutionarily conserved and have been identified to be transmembrane. Functionally, they have been identified to be necessary for the full activation of the Hh signaling pathway. While precise location of members of the tectonic family is as yet unclear, it has been hypothesized that tectonic-1 (TCTN-1) may be found on the extracellular end of the ciliary necklace. This hypothesis is supported by the fact that it interacts with transmembrane protein while at the same time has signal peptides. Tectonic-2 and 3 (TCTN-2 and TCTN-3), on the other hand, have been hypothesized to be transmembrane elements by themselves. Amongst these, TCTN2 has been shown to be an important player in the landscape of MKS[23].

Our lab undertook an imaging based study of Tctn2. Cell sample preparation followed a protocol described in the previous sections. For immunostaining Tctn2, we used mouse monoclonal antibody to Tctn2 (ab119091, Abcam). Rabbit polyclonal antibody against pericentrin was used to label pericentrin on the same sample. As shown in figure 3-7, while one can infer the location of Tctn2 to be around the transition zone region, it is hard to decipher any structural information of Tctn2 due to the resolution limitation. With transition zone proteins such as Tctn2, one is not only interested in the structural detail of the molecule itself but is also interested in the complex dynamic interaction between Tctn2 and other members of the transition zone protein complex. This would not be possible with the resolution limited conventional imaging systems and would need a super-resolution approach to study, such as apSTED microscopy.

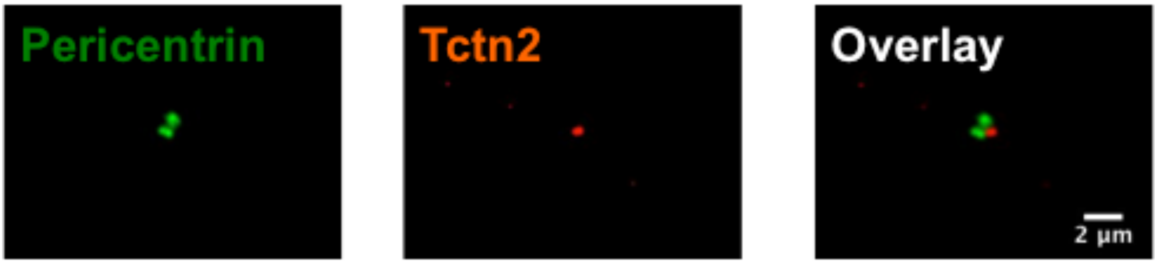

**Figure 3-7. Hff1 cells were labeled for pericentrin and Tctn2. Tctn 2 is a member of the Tectonic family, a transmembrane protein, demonstrated to play a role in ciliopathies such as MKS. The vicinity of TCTN2 to pericentrin on the overaly image on the right underscores the transition zone localization of Tctn2.**

Another integral part of transition zone protein complex is Cep290. Cep290 enables the localization of MKS-JBTS proteins at the transition zone and hence is an important player in maintaining homeostasis of primary cilia. Furthermore, they have been shown to be important in the formation of Y links, links that connect the microtubule doublets of primary cilia axoneme to the plasma membrane of primary cilia. Taken together, data suggests both a structural and functional role for Cep290 in maintenance of normal primary cilia function.

Our lab conducted an imaging based assay to study Cep290. Following the previously described protocol, we labeled Cep290 using rabbit polyclonal antibody to Cep290 (ab84870, Abcam). Imaging these samples under 100x epi-fluorescence revealed Cep290 to localize at the base of primary cilia. This was consistent with data reported by other studies. However, the resolution of this microscope was neither high enough to elucidate fine structural detail of Cep290 structure nor high enough to undertake co-localization studies between Cep290 and other members of the transition zone protein complex. In order to enable such studies, we undertook high-resolution apSTED study of Cep290 (results reported in chapter 5).

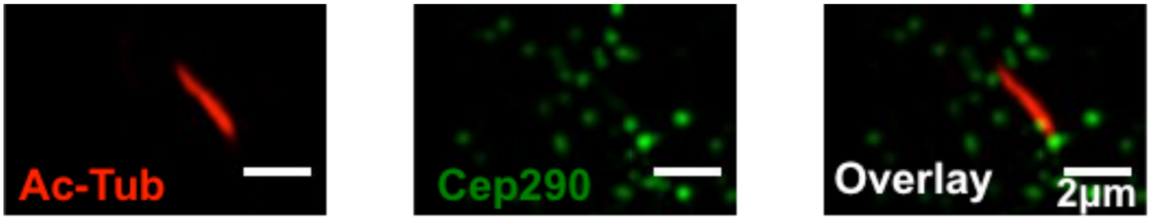

**Figure 3-8. Ac-Tub and Cep290 were labeled on Hff1 cells. As highlighted in the overlay image, Cep290 localized at the base of primary cilia. However, the structural detail of Cep290 was beyond the scope of the resolution of the microscope used to collect this dataset.**

In summary, we setup imaging based assays to study several aspects of primary cilia, such as their mesoscale structure, relative localizations of different molecular components of primary cilia structures, and molecules participating in mediation of signaling pathways. While we got some very exciting and insightful results, we also came across aspects of primary cilia that were beyond the scope of the resolution limit of conventional epi-fluorescence imaging. We revisited some of the aspects described here using our custom-built apSTED nanoscope. Results of those studies are reported in chapter 5.

## Reference:

1. McGlashan, S. R. *et al.* Mechanical loading modulates chondrocyte primary cilia incidence and length. *Cell. Biol. Int.* **34**, 441–446 (2010).
2. Resnick, A. ScienceDirect - Biophysical Journal : Force-Response Considerations in Ciliary Mechanosensation. *Biophys J* (2007).
3. Ko, H. W. The primary cilium as a multiple cellular signaling scaffold in development and disease. *BMB Rep* **45**, 427–432 (2012).
4. Ingham, P. W. & McMahon, A. P. Hedgehog signaling in animal development: paradigms and principles. *Genes & Development* **15**, 3059–3087 (2001).
5. Affolter, M., Zeller, R. & Caussinus, E. Tissue remodelling through branching morphogenesis. *Nat Rev Mol Cell Biol* **10**, 831–842 (2009).
6. Li, X.-J. *et al.* Coordination of sonic hedgehog and Wnt signaling determines ventral and dorsal telencephalic neuron types from human embryonic stem cells. *Development* **136**, 4055–4063 (2009).
7. Sanchez, P. Inhibition of prostate cancer proliferation by interference with SONIC HEDGEHOG-GLI1 signaling. *Proc Natl Acad Sci USA* **101**, 12561–12566 (2004).
8. Roessler, E. *et al.* Mutations in the human Sonic Hedgehog gene cause

holoprosencephaly. *Nat Methods* **14**, 357–360 (1996).

9. Romer, J. & Curran, T. Targeting Medulloblastoma: Small-Molecule Inhibitors of the Sonic Hedgehog Pathway as Potential Cancer Therapeutics. *cancerres.aacrjournals.org*

10. Thayer, S. P. *et al.* Hedgehog is an early and late mediator of pancreatic cancer tumorigenesis. *Nature Cell Biology* **425**, 851–856 (2003).

11. Bailey, J. M., Singh, P. K. & Hollingsworth, M. A. Cancer metastasis facilitated by developmental pathways: Sonic hedgehog, Notch, and bone morphogenic proteins. *J. Cell. Biochem.* **102**, 829–839 (2007).

12. Singla, V. & Reiter, J. The primary cilium as the cell's antenna: signaling at a sensory organelle. *Science* **313**, 629 (2006).

13. Rohatgi, R., Milenkovic, L. & Scott, M. P. Patched1 regulates hedgehog signaling at the primary cilium. *Science* **317**, 372–376 (2007).

14. Badano, J. L., Mitsuma, N., Beales, P. L. & Katsanis, N. The Ciliopathies: An Emerging Class of Human Genetic Disorders. *Annu. Rev. Genom. Human Genet.* **7**, 125–148 (2006).

15. Saraiva, J. M. & Baraitser, M. Joubert syndrome: A review. *Am. J. Med. Genet.* **43**, 726–731 (1992).

16. Hildebrandt, F. & Zhou, W. Nephronophthisis-associated ciliopathies. *J. Am. Soc. Nephrol.* **18**, 1855–1871 (2007).

17. Alexiev, B. A., Lin, X., Sun, C.-C. & Brenner, D. S. Meckel-Gruber Syndrome: Pathologic Manifestations, Minimal Diagnostic Criteria, and Differential Diagnosis. *archivesofpathology.org*

18. Sang, L. *et al.* Mapping the NPHP-JBTS-MKS protein network reveals ciliopathy disease genes and pathways. *Cell* **145**, 513–528 (2011).
19. Williams, C. L. *et al.* MKS and NPHP modules cooperate to establish basal body/transition zone membrane associations and ciliary gate function during ciliogenesis. *The Journal of Cell Biology* **192**, 1023–1041 (2011).
20. Jiang, S. T. *et al.* Targeted disruption of Nphp1 causes male infertility due to defects in the later steps of sperm morphogenesis in mice. *Hum. Mol. Genet.* **17**, 3368–3379 (2008).
21. Garcia-Gonzalo, F. R. F. & Reiter, J. F. J. Scoring a backstage pass: Mechanisms of ciliogenesis and ciliary access. *The Journal of Cell Biology* **197**, 697–709 (2012).
22. Reiter, J. F. Tectonic, a novel regulator of the Hedgehog pathway required for both activation and inhibition. *Genes & Development* **20**, 22–27 (2006).
23. Shaheen, R. *et al.* A TCTN2 mutation defines a novel Meckel Gruber syndrome locus. *Hum. Mutat.* **32**, 573–578 (2011).

# 4 Effects of cell reprogramming on the characteristics of primary cilia

One of the most significant primary cilia functions is the mediation of cellular signaling pathways[1]. Of particular note is the mediation of sonic hedgehog[2] and Wnt[1] signaling pathways. Both of these pathways have previously been shown to be important in maintaining tissue homeostasis in stem cells[3].

Recent work on embryonic stem cells (ESCs) documented the presence of primary cilia on ESCs[4]. While ESCs promise to be one of the most important tools in understanding developmental biology and providing an avenue to explore the possibility of cell replacement therapy, they have been plagued by ethical, political, moral, and technical challenges. Development of induced pluripotent stem cell (iPS) technology[5] has enabled the circumvention of these challenges. Briefly, ectopic expression of transcription factors OCT4, Sox2, Klf4, and c-Myc, on somatic (adult) cells results in induction of embryonic stem-like state in these cells. The resulting cell line, induced pluripotent stem cell (iPSC), has been shown to be phenotypically remarkably similar to embryonic stem cells[5-7]. Minor genetic variations have more recently been reported[8]. However, iPSCs pass the stringent of functional tests, such as tetraploid complementation assay[9], underscoring their pluripotent state and their complementary applications in stem cell biology.

Maintenance of pluripotency and controlling the process of differentiation could be considered two of the biggest scientific challenges to applications of stem cell biology. Given the role of primary cilia in mediation of signaling pathways believed to play significant roles in this context, we endeavored to study primary cilia in the context of iPSCs. A complete lack of prior work in the field compelled us to start with setting up assays to verify the presence of primary cilia on iPSCs. We undertook systematic studies to validate the presence of primary cilia, and to confirm its functional status. Furthermore, we undertook differential morphometric analyses comparing primary cilia structures on iPSCs with those on their somatic cell counterparts. Our results show significant morphological differences between these two classes of primary cilia underscoring the underlying differences in mediation of cellular signaling pathways.

## 4.1 Primary cilia are present on reprogrammed human iPSCs

Immunostaining of acetylated tubulin (ac-tub) and pericentrin was first conducted to examine the existence of primary cilia. Briefly, primary human fibroblasts (from New York Stem Cell Foundation (NYSCF)) were maintained in a 37°C humidified incubator at 5% $CO_2$ in 10% Hyclone fetal bovine serum and DMEM with 1% HEPES. Cells were passaged with Trypsin. hiPSCs were reprogrammed from the abovementioned human fibroblasts by NYSCF using lentiviral vectors of Oct4, Sox2, Klf4, and cMyc. This cell line was validated using immunostaining against pluripotency markers such as Sox2, Oct4, and Nanog, performing a teratoma assay on NSG mice, and through qPCR confirmation of expression of stem cell genes and silencing of viral transgenes by NYSCF[10]. These hiPSCs were maintained in our lab in a 37°C humidified incubator at 5% $CO_2$ on mouse feeder layer in 15% serum replacement and KO DMEM

(Invitrogen) with 1% non-essential amino acid, 1.0 mM L-glutamine, 0.1 mM β-mercaptoethanol, and 8 ng/mL bFGF. To passage the cells, undifferentiated colonies were cut into small pieces by microdissection. The pieces were transferred to a plate coated with 0.1% gelatin and fresh mouse feeder layer.

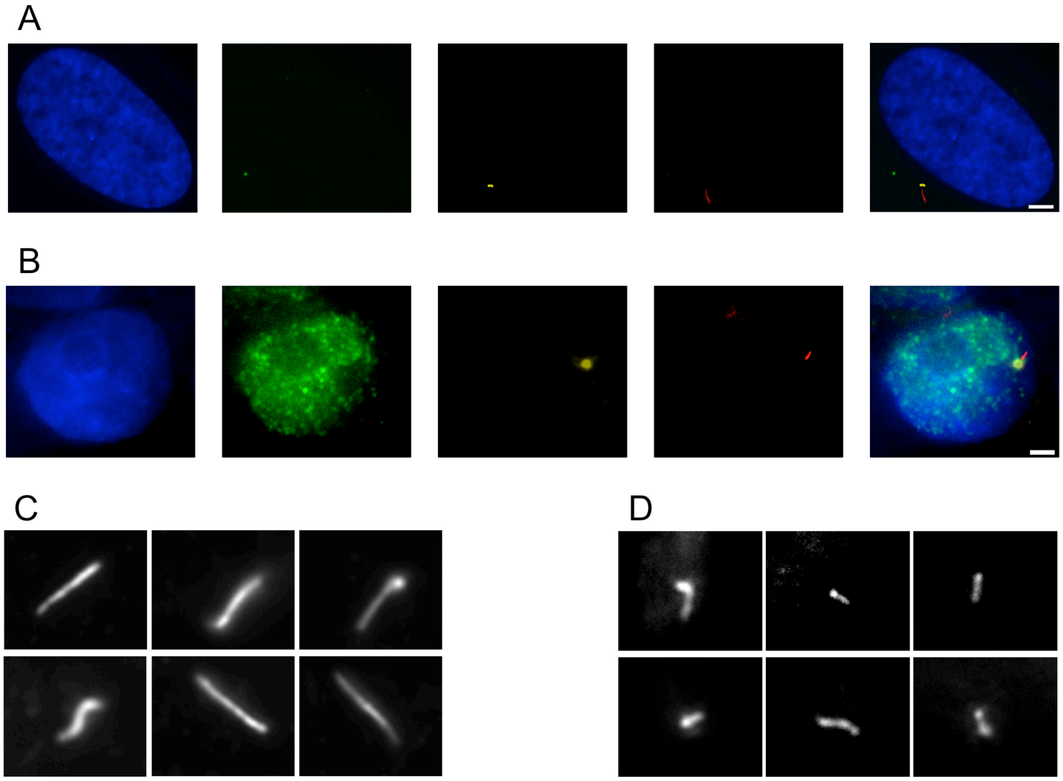

**Figure 4-1. Immunofluorescence imaging revealed different morphological characteristics of primary cilia between human fibroblasts and reprogrammed hiPSCs. (A) Characterization of primary cilia on human fibroblast cells. Differentiated cells were identified through nuclear localization with Hoechst (blue) and an absence of Nanog (dark in the second panel). Localization of ac-tub (red) and pericentrin (yellow) confirmed the presence of primary cilia. An overlay displaying the position of primary cilia relative to the nuclei (scale bar: 5 μm) (B) Characterization**

**of primary cilia on hiPSCs. Cells were identified by nuclear localization of Hoechst (blue). The pluripotent state of the cells was validated by expression of Nanog (green). Localization of ac-tub (red) and pericentrin (yellow) confirms the presence of primary cilia (scale bar: 2 μm) (C) Sample images of primary cilia of human fibroblasts and (D) sample images of primary cilia of hiPSCs for morphometric analysis.**

hiPSCs were cultured on a feeder-coated plate with KO-DMEM media containing 15% knockout serum replacement for 2 days to reach ~100% confluence. These hiPSCs were either fixed right after or cultured for additional 24 hours without serum replacement before fixing. In addition to the labeling of ac-tub and pericentrin, Nanog was also labeled to confirm the pluripotency of cells and Hoechst was used to identify nuclei. The following protocol was followed to stain these cells:

Cell samples were transferred to glass bottom plates (Mattek) on which they were stained and imaged. Cells were washed in PBS and fixed with 4% paraformaldehyde. Cells were permeabilized with 0.2% Triton-X in PBS for 10 minutes and blocked in a 10% serum solution for 1 hour. The primary antibodies used were mouse anti-acetylated a-tubulin (Abcam, 1:1500), rabbit anti-pericentrin (Abcam, 1:1000), and goat anti-Nanog (R&D Systems, 1:800). Primary antibodies were diluted in 10% serum and incubated at $4^{o}$C overnight. Cells were then washed three times with 0.2% Triton-X in PBS solution. The secondary antibodies used were anti-rabbit Alexa Flour 488, anti-mouse Alexa Flour 588, and anti-goat Alexa Flour 647. Fixed human fibroblasts and hiPSCs samples were imaged using a motorized inverted microscope (IX-81, Olympus America) mounted with a low-noise CCD camera (C8484, Hamamatsu).

Images were typically collected using a 100x oil immersion (UPLSAPO100x-1.4 NA, Olympus) lens with exposure time of 500 ms. Different color channel images were collected sequentially. Given the 3D structure of hiPSC colonies, z-focus of the microscope was changed slightly to collect information from different color channels. In order to avoid double counting primary cilia from cells stacked on top of each other, images collected with a difference in z-focus >10μm amongst different color channels were ignored. Images were imported to MATLAB. Custom-built scripts were developed to false color images from different color channels and to combine data from various channels. Individual images were thresholded using a MATLAB script. Typically, the threshold was placed at 5-10%.

The immunostaining results showed that Nanog-positive hiPSCs indeed possessed primary cilia (Figure 3b), with ac-tub (red) representing the axoneme part and pericentrin (yellow) representing the basal body. To study the effects of reprogramming on primary cilia, we also labeled the parental human fibroblasts with the same set of antibodies. These fibroblasts were grown in DMEM media containing 10% fetal bovine serum (FBS) for 2 days to ~100% confluence, followed by either immediate fixation or serum starvation for 24 hours before fixing them. Comparison of human fibroblasts and hiPSCs illustrated that both cell lines possessed primary cilia, while Nanog was absent in fibroblasts but present in hiPSCs, as expected in terms of pluripotency (Figures 3A and 3B). To find whether there were any different characteristics of primary cilia between these two cell lines, we have imaged a significant number of primary cilia in each of these cell lines to sample their morphological features (Figures 3C and 3D).

## 4.2 Serum starvation induced ciliogenesis in hiPSCs without affecting the expression of pluripotency markers

Serum starvation is known to promote ciliogenesis in somatic cells, so we aimed to use starvation to increase the percentage of cells possessing primary cilia. The only concern was that starvation might also affect the pluripotency of hiPSCs when cells were not grown in the preferred ESC media. We conducted Nanog immunostaining of hiPSCs before and after 24-hour serum starvation and the results showed negligible effect of serum deprivation on the pluripotency of hiPSCs. Cells after 24-hour serum deprivation were still strongly Nanog positive in terms of immunofluorescence signals.

To corroborate our imaging data, we also performed quantitative reverse-transcriptase polymerase chain reaction (qRT-PCR) to examine mRNA expression levels. Both culture conditions utilized during imaging assays, cultures with media enriched with serum and cultures grown for 24 hours in serum-deprived conditions, were included on qRT-PCR studies. Briefly, total RNA was extracted with the RNeasy Mini kit (Qiagen) and 1 μg of total RNA was converted to cDNA using the QuantiTect Reverse Transcription Kit (Qiagen). Gene expression was assayed by quantitative real-time PCR using SYBR green reagents (Applied Biosystems). The primer sequences are listed:

NANOG F 5-ACAACTGGCCGAAGAATAGCA-3; R 5-GGTTCCCAGTCGGGTTCAC-3

CRIPTO F 5-CGGAACTGTGAGCACGATGT-3; R 5-GGGCAGCCAGGTGTCATG-3

GAPDH F 5-GCACCGTCAAGGCTGAGAAC-3; R 5-AGGGATCTCGCTCCTGGAA-3

UBC F 5-ATTTGGGTCGCGGTTCTTG-3; R 5-TGCCTTGACATTCTCGATGGT-3

B2M F 5-TGCTGTCTCCATGTTTGATGTATCT-3; R 5-TCTCTGCTCCCCACCTCTAAGT

SHH F 5-CCTCGCTGCTGGTATGCTCGGGAC T; R 5-CTCTGAGTCATCAGCCTGTCCGCTC

PTCH1 F 5-GCACTACTTCAGAGACTGGCTTC; R 5-AGAAAGGGAACTGGGCATACTC

SMO F 5-ACCCCGGGCTGCTGAGTGAGAAG; R 5-TGGGCCCAGGCAGAGGAGACATC

GLI1 F 5-GCCGTGTAAAGCTCCAGTGAACACA; R 5-TCCCACTTTGAGAGGCCCATAGCAAG

GLI2 F 5-TGGCCGCTTCAGATGACAGATGTT G; R 5-CGTTAGCCGAATGTCAGCCGTGAAG

Ubiquitin C (UBC) was used as the endogenous reference in the hiPSC and fibroblast cells lines. Each sample was run in triplicate. The log-linear phase of amplification was monitored to obtain threshold cycle values. The comparative threshold method was used to determine levels of expression. Briefly, the number of cycles required to for the fluorescent signal to cross the threshold (i.e. exceed background level of fluorescence) is defined as the cycle threshold (CT) in PCR parlance. CT levels are inversely proportional to the level of nucleic acid material present in the sample, i.e. if a specific gene is expressed at a high level in a specific cell type, it will require fewer cycles to reach the threshold level and therefore, lower is it's CT value and vice versa. Experiments were carried out in triplicates and mean CT values (CT mean) were used for quantifications. Exponent of negative CT value on 2 was used as quantification for mRNA level in a given sample. Exponent of negative standard error of mean of CT values on 2 were used as SE for the given analyses.

Our data shows expression levels of pluripotency markers, Nanog and Cripto, in hiPSCs to be $>10^3$ times those in corresponding fibroblast cell line (Figure 4A). Furthermore, when cells were cultured 24 hours in serum deprived media conditions, there was negligible effect on expression levels of pluripotency markers. This data validated the use of serum deprivation as an experimental condition in the context of pluripotent cells. While serum deprivation has been extensively used as an experimental condition to study primary cilia in myriad cell lines, we established the validity of this approach for use with hiPSCs by confirming its negligible effects on expression levels of pluripotency markers.

While serum condition had no appreciable effect on pluripotency, it had a significant effect on the percentage of cells with presence of primary cilia (Figure

5). The percentage of hiPSCs cultured with normal serum levels containing primary cilia was ~19%, whereas, the percentage of hiPSCs cultured in serum deprived conditions for 24 hours was as high as ~32%. In contrast, the percentage of fibroblast cells cultured with normal serum levels containing primary cilia was ~23%, whereas, the percentage of fibroblast cells cultured in serum deprived conditions for 24 hours was as high as ~53%, with the percentage rising to ~80% when cultured in serum deprived conditions for 48 hours (data not shown). Our data suggests that the percentage of cells containing primary cilia in hiPSCs is inherently smaller than the percentage of their parental somatic cells containing primary cilia.

## 4.3 Hedgehog signaling pathways were active in hiPSCs

To test whether Shh pathways were functional or not in the primary cilia of reprogrammed cells, we conducted RT-PCR to establish the expression levels of hedgehog signaling pathway molecules in fibroblasts and reprogrammed hiPSCs, including Shh, Smo, Ptch1, Gli1, and Gli2. Consistent with the results found in hESCs[11] expression levels of Smo, Ptch1, Gli1 and Gli2 were higher in reprogrammed cells ($p<0.001$) as compared to fibroblasts (Figure 4b). Specifically, Gli1 was expressed ~80-fold higher in hiPSCs than in parental human fibroblasts, and Ptch1 was expressed ~25-fold higher in hiPSCs compared to fibroblasts. Expression levels of Shh did not change as a result of reprogramming (null-hypothesis not rejected – two-sample t-test). This result indicated that molecules in Shh pathways were active in hiPSCs, potentially demonstrating functional states of primary cilia in reprogrammed cells.

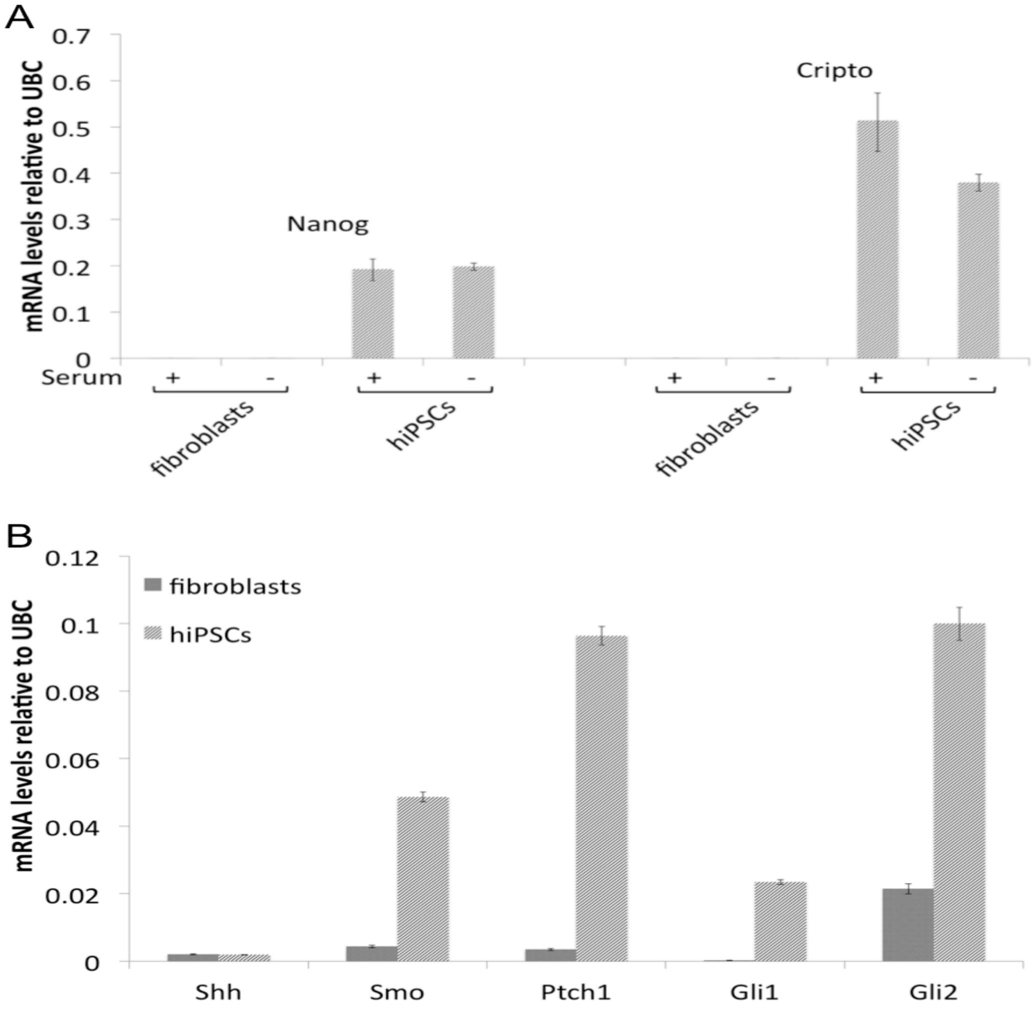

**Figure 4-2. Expression profiling of pluripotency markers and elements in Shh signaling pathways for human fibroblasts and reprogrammed hiPSCs. (A) Expression levels of pluripotency genes for human fibroblasts and reprogrammed hiPSCs in two different serum conditions. High expression levels of pluripotency markers Nanog and Cripto were observed for reprogrammed cells. 24-hour serum starvation (shown as '-') had little effect on the expression levels of Nanog and Cripto, where the expression levels of hiPSCs were consistently $>10^3$ times higher than corresponding levels of the parental fibroblasts both in serum enriched and serum**

**starved conditions. (B) Expression levels of hedgehog signaling pathway molecules in human fibroblasts and hiPSCs. Expression levels of Smo, Ptch1, Gli1, and Gli2 showed ~$10^1$-$10^2$ times higher than those in the corresponding parental fibroblasts. Ubiquitin C (UBC) was used as the reference gene.**

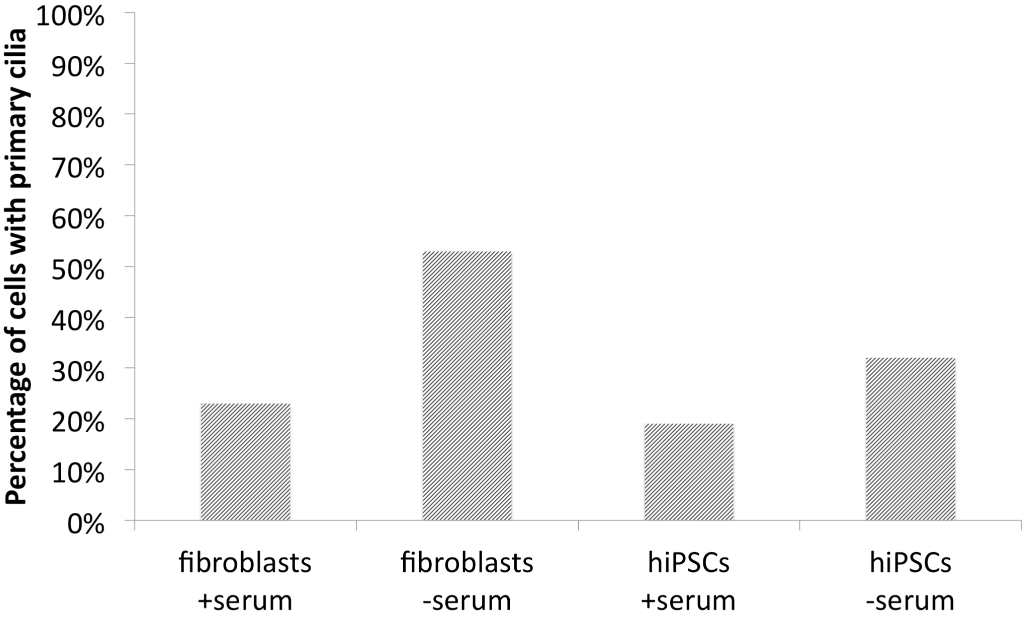

**Figure 4-3. Effect of reprogramming and culture conditions on the populations of primary cilia. Reprogramming resulted in a decrease in percentage of cells displaying primary cilia morphology, from ~23% to ~19%. Serum starvation for 24 hours resulted in an increase in primary cilia population, to ~53% for fibroblast cells and ~32% for reprogrammed hiPSCs. Regardless of the culture conditions, reprogrammed cells consistently displayed a lower population of primary cilia.**

## 4.4 Reprogramming resulted in a decrease in the length of primary cilia

Assured our reprogrammed cells possessed primary cilia, we examined the similarities and differences in mechanical characteristics between human fibroblasts and reprogrammed hiPSCs. Specifically we utilized home built scripts in imageJ to measure the length characteristic of primary cilia. Reprogramming fibroblasts resulted in a decrease in the length of primary cilia both with and without serum deprivation (Figure 6). The mean length of primary cilia found on fibroblast cells decreased from ~2.2 microns to ~1.1 microns after reprogramming when cultured with serum ($p<0.001$), and from ~2.6 microns to ~1.45 microns when cultured in serum starved condition. These measurements suggested that primary cilia may be inherently shorter in reprogrammed hiPSCs than their counterparts in somatic cells from which they were derived from. Shorter primary cilia may impact the chemo-mechanical sensing capabilities of hiPSCs[12,13].

## 4.5 Reprogramming altered morphological characteristics of primary cilia

In addition to the length, we have also examined the reprogramming effects on other structural characteristics of primary cilia. Based on the classification of bending shapes used for primary cilia[14], we have categorized them into two different sets: straight ones, where the cilia had negligible bend along the axoneme axis, and kinked ones, where at least one abrupt curvature change was observed. An example of a kinked primary cilium is shown in (Figure

7 inset). We have also observed certain bright spots, or puncta, of ac-tub signals along axonemes, where cells before and after reprogramming seemed to possess different populations of puncta. Though it is still unclear the physical compositions of these puncta, a statistical analysis of the presence of these puncta would be important and were conducted in this study.

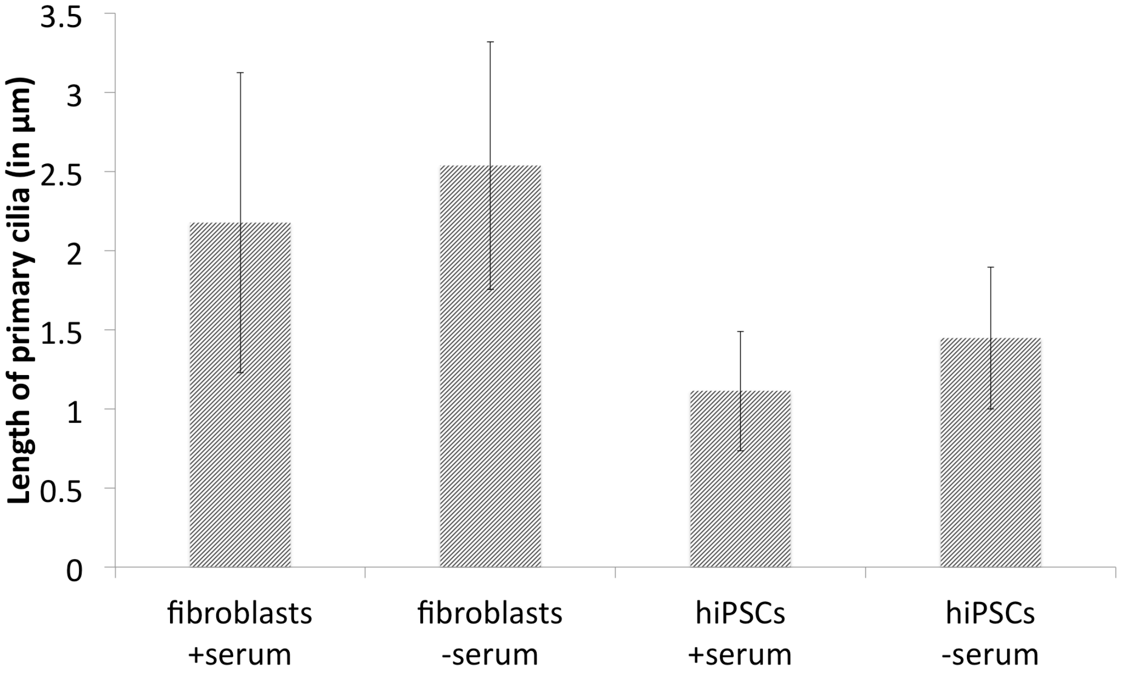

**Figure 4-4. Effect of reprogramming and culture conditions on the length of primary cilia. The length of primary cilia decreases as a result of reprogramming. Under serum enriched conditions, the mean length decreased from ~2.15 microns to ~1.1 microns after reprogramming, whereas under serum starved culture conditions, mean length decreased from ~2.38 microns to ~1.45 microns ($p<0.001$) after reprogramming.**

The percentage of primary cilia displaying kinked geometries (Figure 7) in conventionally grown fibroblasts, with serum, was ~40%. While serum deprivation increases the percentage of primary cilia with kink geometry to ~60%, reprogramming resulted in a decrease in percentage of primary cilia with kink geometries. 30% of primary cilia on reprogrammed hiPSCs displayed kink geometry when cultured in conventional culture conditions, with serum, as opposed to 40% when cultured in serum-starved conditions for 24 hours.

We quantified punctations along the axonemes of primary cilia. To analyze the spatial distribution of puncta, “tips” and “bases” of primary cilia were defined. The end of primary cilia proximal to pericentrin was defined as the primary cilium’s bases and the distal end was defined as tips. We found puncta to be randomly distributed across tips, bases, and even the rest of the axoneme structure. This data suggested punctations to be independent of the orientation of primary cilia.

We analyzed the population of punctations on primary cilia for both cell types across different serum conditions (Figure 8). When cultured in serum enriched conditions, ~67% of primary cilia found on fibroblasts were punctated as opposed to ~44% in the case of hiPSCs. On the other hand, when cultured in serum deprived conditions, ~80% of primary cilia found both on fibroblasts and hiPSCs were punctated. These results suggested that serum conditions could change the percentage of primary cilia possessing puncta, while the difference between fibroblasts and hiPSCs was negligible.

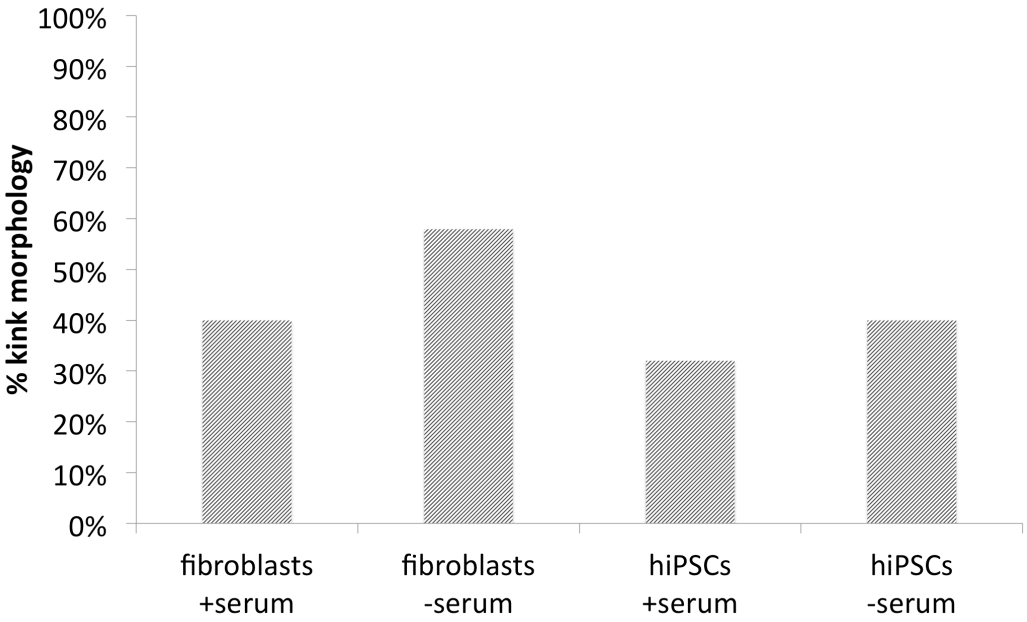

**Figure 4-5. Effect of reprogramming on kinks (sharp bends) of primary cilia. Regardless of the culture condition, a lesser percentage of primary cilia on hiPSCs displayed "kink" morphology. Under regular culture conditions, ~32% of hiPSC primary cilia displayed "kink" morphology as opposed to ~43% in fibroblasts. Under serum starved culture conditions, ~41% of primary cilia on hiPSCs displayed "kink" morphology as opposed to ~55% in fibroblast cells.**

## 4.6 Reprogramming resulted in increase in curvature of primary cilia

Next, we analyzed the curvature of primary cilia on both cell types. To measure the curvature of primary cilia, coordinates for the two end-points as well as for the mid-point of each primary cilium were recorded. A MATLAB script was developed to fit a circle through these three points and the inverse of the radius of the circular fit was considered the curvature of the primary cilium. In order, to find a circular fit, Newton-Pratt least squares were utilized.

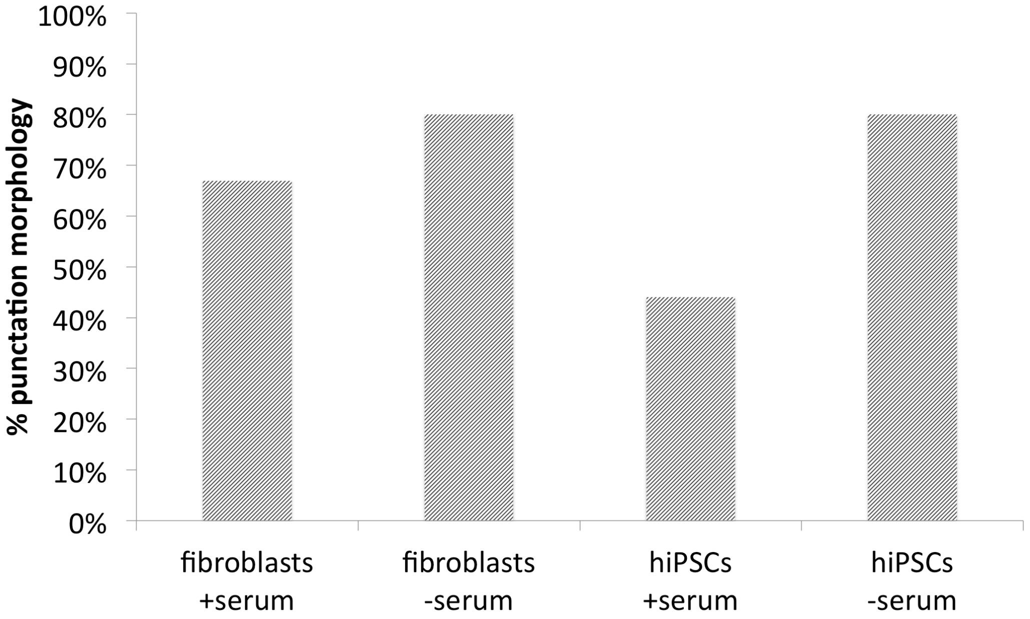

**Figure 4-6. Effect of reprogramming on the populations of primary cilia possessing punctated aggregates of ac-tub. Reprogramming resulted in a slight decrease in the percentage of primary cilia displaying punctated morphology.**

Our analysis revealed that reprogramming resulted in an increase in curvature of primary cilia from ~0.01 $\mu m^{-1}$ to ~0.047 $\mu m^{-1}$ ($p<0.02$) when cultured in serum enriched conditions, and from ~0.016 $\mu m^{-1}$ to 0.063 $\mu m^{-1}$ ($p<0.01$) when cultured in serum starved conditions (Figure 9). Using a beam model for the obtained curvatures assuming the same diameter for primary cilia of both cell lines, we estimated that reprogramming changed Young's modulus by up to ~5-fold.

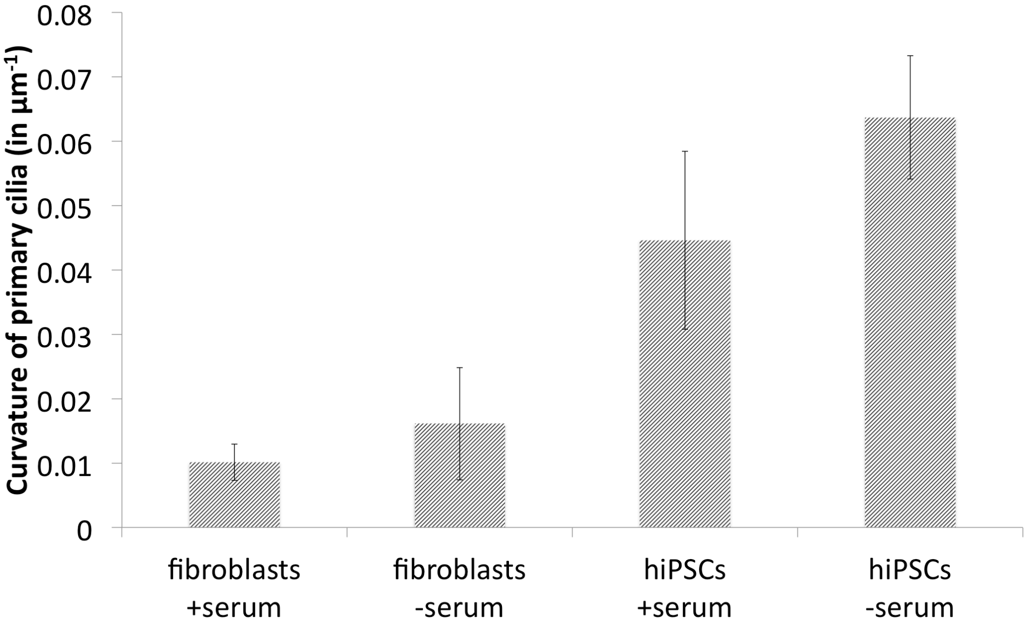

**Figure 4-7. Effect of reprogramming on the curvature of primary cilia. Morphometric analysis of primary cilia on reprogrammed cells demonstrated an increase in the curvature of primary cilia as a result of reprogramming. Serum deprivation in culture further accentuated this difference ($p<0.001$).**

## Discussion

In this study, we have demonstrated the presence of primary cilia on reprogrammed hiPSCs. Through multi-color high-resolution immunofluorescence imaging, we performed a comparative study of primary cilia on parental somatic cell line and corresponding pluripotent reprogrammed cells. Data from these comparative studies show a decrease in percentage of cells containing primary cilia as a result of reprogramming. To validate the functional status of these primary cilia, we conducted qRT-PCR assays to check for expression levels of molecules participating in hedgehog signaling. Hedgehog signaling has previously been shown to occur at the site of, and be dependent on the optimal functioning of, primary cilia[15]. We demonstrate higher expression levels for almost all the molecules, with the exception of Shh, participating in hedgehog signaling as a result of reprogramming. The important roles of mechanosensing of primary cilia led us to conduct comparative mechanical analyses of primary cilia on parental and reprogrammed cells lines. Our data show a decrease in length of primary cilia resulting from reprogramming. Morphometric analyses of primary cilia structures further indicate a significant increase in curvature of primary cilia resulting from reprogramming. While reprogramming resulted in a decrease in punctations on primary cilia surface, culturing reprogrammed cells in serum-starved conditions for 24 hours recovered the percentage of primary cilia displaying punctation geometry on their surface to levels statistically similar to those found on parental fibroblast cell lines. A reduction in percentage of primary cilia displaying kink geometries resulting from reprogramming could not be recovered by manipulation of culture conditions.

Under normal culture conditions, we have found that the percentage of reprogrammed hiPSCs displaying primary cilia morphology was ~19%. Previous studies have shown that H1 hESCs cultured in serum enriched conditions displayed primary cilia morphology on ~33% of cells[4]. 24 hour serum starved culture conditions resulted in ~32% of hiPSCs developing primary cilia morphology, while under comparable culture conditions, ~50% of H1 hESCs displayed primary cilia morphology[4]. One of the possibilities for the differences in primary cilia population in the hESCs and hiPSCs may be the differences in culture conditions utilized by the two studies. Whereas the H1 cells were cultured for 5 days, this study studied hiPSCs cultured for 2 days.

To compare the primary cilia population on reprogrammed cells with their parental fibroblast cell line, we performed immunofluorescence imaging studies on fibroblasts. Under two comparable culture conditions, i.e. serum enriched and serum starved for 24 hours, population percentages of primary cilia on fibroblasts were ~23% and ~53% respectively. A possible explanation is different populations of cells in the $G_0$ phase between pluripotent cells and differentiated cells, and further studies will be needed to test this statement. A 48 hour serum starvation experiment on fibroblasts did result in a high ~80% cells displaying primary cilia morphology (data not shown). However, anticipating potential negative effects of prolonged serum starvation on pluripotency of reprogrammed cells, we did not implement this condition on hiPSCs.

To establish the functional status of primary cilia on reprogrammed cells, we conducted RT-PCR studies. Our data indicate higher expression levels of Smo, Ptch1, Gli1, and Gli2 in reprogrammed cells when compared to their parental fibroblast lines. These expression levels of hiPSCs are in agreement with the expression levels reported on hESCs[4]. The importance of the hedgehog signaling pathway in stem cell differentiation and pattern formation has been extensively studied earlier[12,13,16-18]. These roles of hedgehog signaling in stem cells and development imply potentially active functions of this signaling pathway in hiPSCs. Consistently, we observed the upregulation of several downstream effectors of sonic hedgehog including Smo, Ptch1, Gli1 and Gli2. The one exception we found was that the level of Shh did not significantly alter as a result of reprogramming. This is actually consistent with the finding of a low expression level of Shh in hESCs, indicating the possible roles of Shh in differentiation[19]. Studies have shown changes in mechanosensory landscape occurring on the site of primary cilia to be influenced by the morphology of primary cilia, in particular by the length of primary cilia[20-22]. This motivated us to study the effect of reprogramming on the length of primary cilia. Our data suggests a systematic decrease in the length of primary cilia resulting from reprogramming. Specifically, under conventional culture conditions, the length decreased from ~2.15 microns to ~1.1 microns; and under serum starved culture conditions, it decreased from ~2.38 microns to ~1.45 microns. Chemo-mechanical sensory landscape of reprogrammed cells may be influenced by this decrease in primary cilia length. For example, recent studies have demonstrated a decrease in length of primary cilia to correlate with a decrease in sensitivity to $Na^+$ signaling[20-22]. A high density of cells in hiPSC colonies growing in 3D geometries may compound this effect. To undertake chemo-induced differentiation, de-differentiation or transverse reprogramming, physical access to primary cilia would be important. The short length of primary cilia combined with low percentage of cells containing primary cilia and the underlying 3D growth of hiPSCs together highlight a significant challenge to such endeavors. Detailed structural and morphological measurements of primary cilia may provide with an avenue to address this challenge.

Morphometric analyses of primary cilia geometries revealed a decrease in primary cilia displaying kink geometries from ~55% to ~41% as a result of reprogramming. The reason behind= this difference remains to be explored. It would be interesting to investigate any structural differences between kinks and the rest of the primary cilium. While the size of such kinks was beyond the resolution limit of the microscope used for these studies, recent developments in the field of superresolution imaging may make exploring such questions possible. An analysis of punctations found on primary cilia revealed them to be almost immune to the process of reprogramming. While the percentage of primary cilia with punctations on their surface decreased from ~57% to ~50%, ~52% to ~48% after serum deprivation, these differences were not statistically significant. While the structural variations of the primary cilia structure resulting in punctations are not clear, it is of interest to note that despite all the other morphometric differences reported here, surface punctations remain immune to reprogramming, perhaps underlying the significance of this structural peculiarity. Reprogramming resulted in increase in curvature of primary cilia, ~4.4-fold increase under serum enriched culture conditions and ~4-fold under serum starved culture condition for 24 hours. This increase in curvature may indicate an underlying difference in the rigidities of primary cilia occurring on the two cell lines. A possible implication of higher rigidities of primary cilia on reprogrammed cells may be molecular differences in the structure of primary cilia occurring as a result of reprogramming. Studies have shown that binding of microtubule associated proteins (MAP) correlate with an increase in flexural rigidity of primary cilia[14,23], although it is unclear what molecule plays similar roles in affecting the rigidity of primary cilia in hiPSCs. Another possible explanation for the difference in rigidities may be a difference in $Ca^{2+}$ binding, a mechanism previously demonstrated to have a significant impact on stiffness of stereocilia[24]. The size of the primary cilia coupled with the diffraction-limited resolution of our microscope implies fewer pixels per cilia of measurement. Performing circular fits with three points might have resulted in an over-estimation of the curvature of primary cilia. Future studies using so-called super-resolution microscopes may be able to offer most accurate estimates of curvature.

## Reference:

1. Veland, I. R., Awan, A., Pedersen, L. B., Yoder, B. K. & Christensen, S. O. R. T. Primary Cilia and Signaling Pathways in Mammalian Development, Health and Disease. *Cell Physiol Biochem* **111**, p39–p53 (2009).
2. Han, Y. *et al.* Hedgehog signaling and primary cilia are required for the formation of adult neural stem cells. *Nat Neurosci* **11**, 277–284 (2008).
3. Li, W. *et al.* Generation of rat and human induced pluripotent stem cells by combining genetic reprogramming and chemical inhibitors. *Cell Stem Cell* **4**, 16–19 (2009).
4. Kiprilov, E. *et al.* Human embryonic stem cells in culture possess primary cilia with hedgehog signaling machinery. *The Journal of Cell Biology* **180**, 897 (2008).

5. Takahashi, K. & Yamanaka, S. Induction of pluripotent stem cells from mouse embryonic and adult fibroblast cultures by defined factors. *Cell* **126**, 663–676 (2006).

6. Takahashi, K. *et al.* Induction of pluripotent stem cells from adult human fibroblasts by defined factors. *Cell* **131**, 861–872 (2007).

7. Wernig, M. *et al.* In vitro reprogramming of fibroblasts into a pluripotent ES-cell-like state. *Nature* **448**, 318–324 (2007).

8. Lister, R. *et al.* Hotspots of aberrant epigenomic reprogramming in human induced pluripotent stem cells. *Nature* **471**, 68–73 (2011).

9. Zhao, X.-Y., Lv, Z., Li, W., Zeng, F. & Zhou, Q. Production of mice using iPS cells and tetraploid complementation. *Nat Protoc* **5**, 963–971 (2010).

10. Noggle, S. *et al.* Human oocytes reprogram somatic cells to a pluripotent state. *Nature Cell Biology* **478**, 70–75 (2011).

11. MCMAHON, A., INGHAM, P. & TABIN, C. *Current Topics in Developmental Biology*. **53**, 1–114 (Elsevier: 2003).

12. Li, X.-J. *et al.* Coordination of sonic hedgehog and Wnt signaling determines ventral and dorsal telencephalic neuron types from human embryonic stem cells. *Development* **136**, 4055–4063 (2009).

13. Cai, C., Thorne, J. & Grabel, L. Hedgehog serves as a mitogen and survival factor during embryonic stem cell neurogenesis. *Stem Cells* **26**, 1097–1108 (2008).

14. Felgner, H., Frank, R. & Schliwa, M. Flexural rigidity of microtubules measured with the use of optical tweezers. *J. Cell. Sci.* **109 ( Pt 2)**, 509–

516 (1996).

15. Singla, V. & Reiter, J. The primary cilium as the cell's antenna: signaling at a sensory organelle. *Science* **313**, 629 (2006).

16. McMahon, A. P., Ingham, P. W. & Tabin, C. J. *Current Topics in Developmental Biology*. *Current topics in developmental …* **53**, 1–114 (Elsevier: 2003).

17. Elisabeth H Villavicencio, D. O. W. P. M. I. The Sonic Hedgehog–Patched–Gli Pathway in Human Development and Disease. *American Journal of Human Genetics* **67**, 1047 (2000).

18. Bai, L.-Y. *et al.* Differential expression of Sonic hedgehog and Gli1 in hematological malignancies. *Leukemia* **22**, 226–228 (2008).

19. Rho, J.-Y. *et al.* Transcriptional profiling of the developmentally important signalling pathways in human embryonic stem cells. *Hum. Reprod.* **21**, 405–412 (2006).

20. Resnick, A. ScienceDirect - Biophysical Journal : Force-Response Considerations in Ciliary Mechanosensation. *Biophys J* (2007).

21. Besschetnova, T. Y. *et al.* Identification of signaling pathways regulating primary cilium length and flow-mediated adaptation. *Curr. Biol.* **20**, 182–187 (2010).

22. Gardner, K., Arnoczky, S. P. & Lavagnino, M. Effect of in vitro stress-deprivation and cyclic loading on the length of tendon cell cilia in situ. *J. Orthop. Res.* **29**, 582–587 (2011).

23. Takemura, R., Okabe, S. & Umeyama, T. Increased microtubule stability

and alpha tubulin acetylation in cells transfected with microtubule-associated proteins MAP1B, MAP2 or tau. *Journal of Cell …* (1992).

24. Pae, S. Intra- and extracellular calcium modulates stereocilia stiffness on chick cochlear hair cells. (1994).

# 5 apSTED imaging of primary cilia

## 5.1 Primary cilia – need for super-resolution

The primary cilium has been shown to mediate these pathways not only through perceiving chemical changes but also by responding to mechanical stimuli. Specifically, recent work has suggested that changes in available mechanical stimuli to primary cilia result in a change in their length, thereby resulting in reduction in sodium currents. Binding of microtubule-associated protein (MAP) has been shown to correlate with an increase in flexural rigidity of primary cilia[1]. As discussed in chapter 3, several such morphological parameters of primary cilia play an important role in modulating its homeostatic function. However, resolution limit of conventional microscopes inhibit a detailed study of primary cilia morphology through direct visualization. Therefore, to circumvent this problem we implemented super-resolution apSTED nanoscopy. We wanted to utilize the power of apSTED to directly visualize structural detail of primary cilia morphology, previously unattainable by any other far-field optical imaging technique. In particular, we focused on imaging structural aspects of two different regions of primary cilia, i.e. members of transition zone of primary cilia and the ciliary component (axoneme) of primary cilia.

## 5.2 apSTED imaging of the ciliary component of primary cilia

To image primary cilia using apSTED, we prepared cell culture samples and immunostained Hff1 cells against Ac-Tub and Hoechst using the protocol described in chapter 3.

## 5.3 Validation of primary cilia immunostaining

Samples were first imaged under the Olympus microscope to confirm the presence of and optimal labeling of primary cilia before transferring them to the main scope for apSTED imaging. As shown in Figure 5-1, we were able to identify primary cilia on Hff-1 cells. While our STED system was not equipped to image Hoechst, to avoid any background noise, after establishing our ability to identify primary cilia, all subsequent samples for apSTED imaging were labeled only for Ac-Tub.

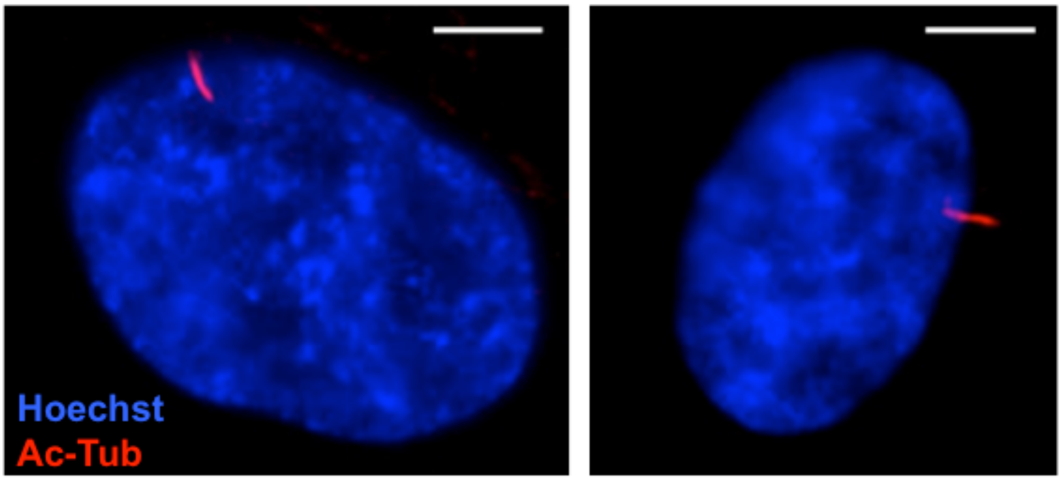

**Figure 5-1. Epi-fluorescence images of primary cilia on Hff1 cells. Hoechst staining was utilized the identify the location of nuclei. Ac-Tub was used to identify the location of primary cilia axoneme. Scale bar: 5 μm**

### 5.3.1 apSTED imaging

Once the sample was placed on the apSTED system, confocal microscopy was performed to find a region of interest before switching to the STED mode to collect apSTED data. For each region of interest, confocal and STED frames were collected side by side with identical parameters to compare the resolution enhancement achieved by STED.

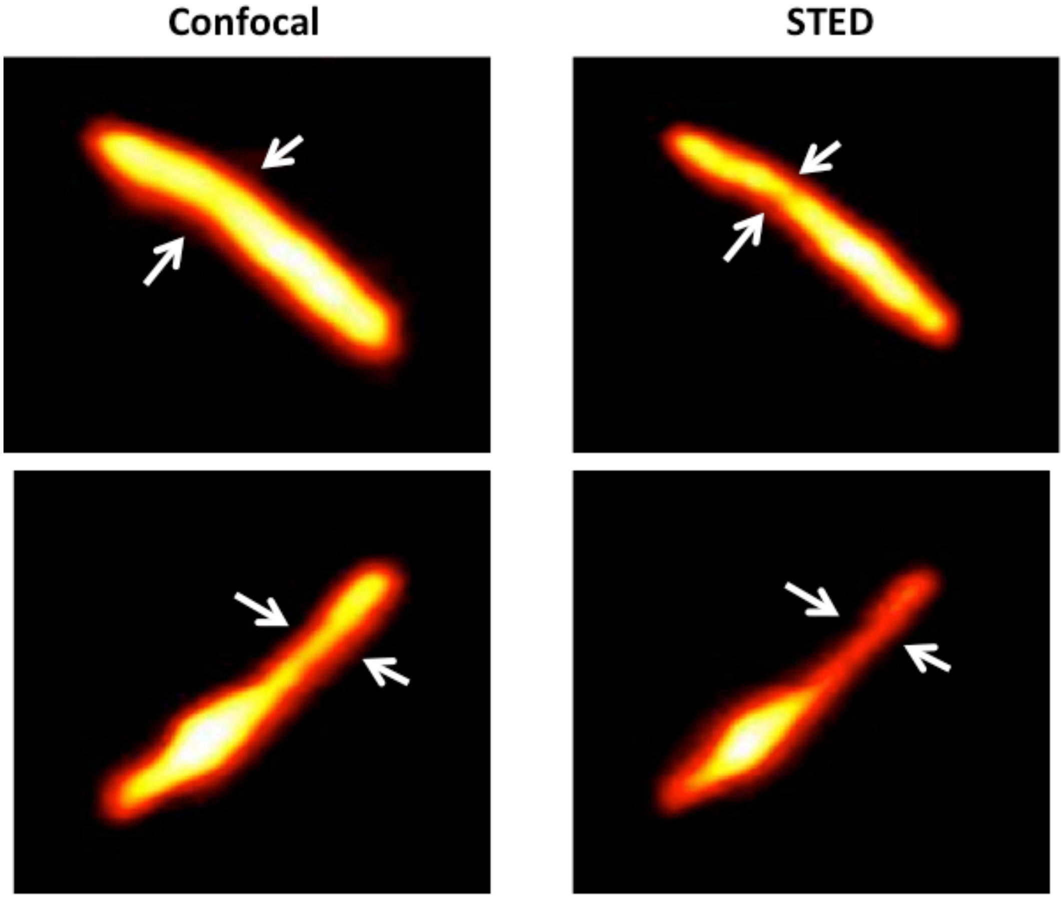

**Figure 5-2. Side by side comparison of confocal and apSTED imaging data of primary cilia found on Hff-1 cells. The image sequence particularly stresses the improvement in resolution that translates into an improvement in estimates of morphological parameters of primary cilia structures. Arrows show regions of interest with significant improvement in resolution.**

One of the primary goals of this study was to establish the advantages of imaging primary cilia using STED. In particular, we aimed to demonstrate the ability of apSTED to improve estimates of various morphological characteristics of primary cilia. An improved estimate of morphological parameters would in turn enable more accurate mechanical models of primary cilia.

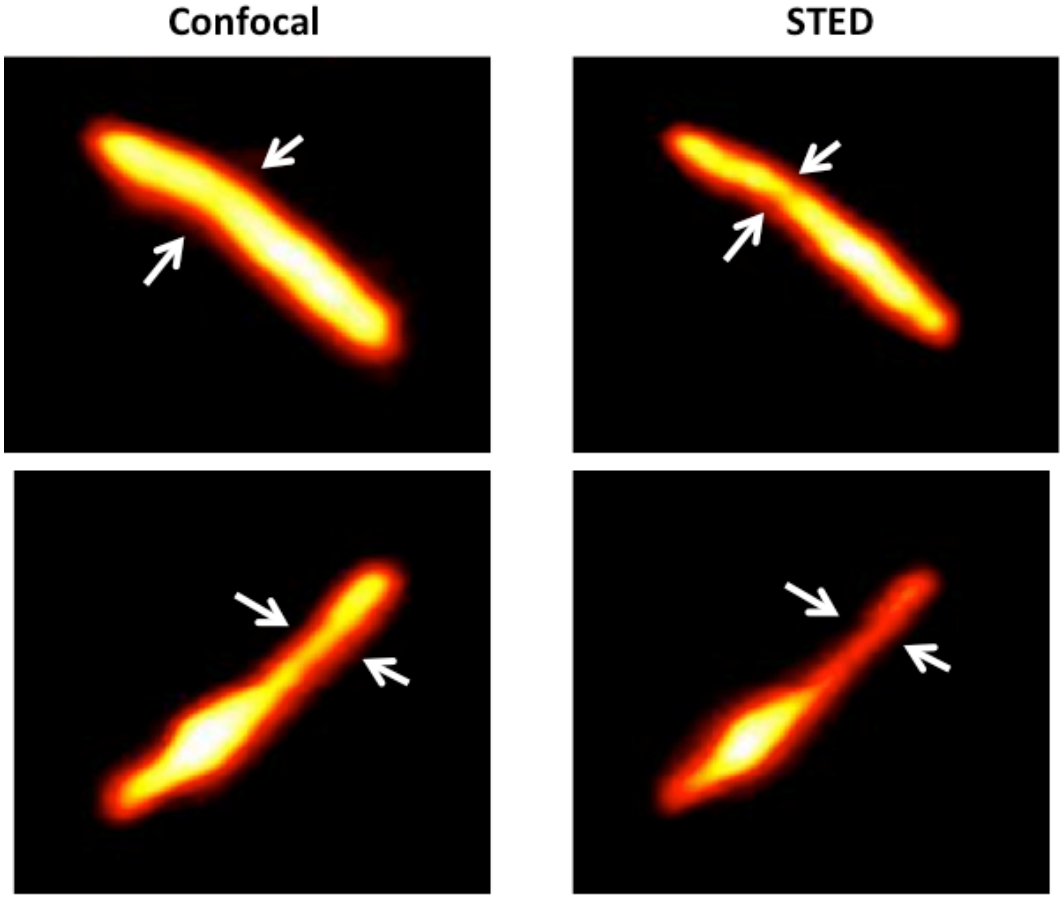

**Figure 5-2** shows a couple of representative images of Ac-Tub stained primary cilia on Hff-1 cells. We did a side by side comparison of confocal and apSTED frames of these structures to underscore the improvement in resolution. In particular, the white arrows show the regions of highest improvement in resolution.

### 5.3.2 Morphometric feature extraction

In order to quantify these image datasets, we developed a custom-built software library in MATLAB. Following is a brief description of the protocol that we followed in developing the software library:

1. Read in confocal-STED image pairs
2. Clean and filter images for first order improvement in signal to noise ratio
3. Implement appropriate thresholding i.e. pixels with 5% intensity levels compared to the highest intensity pixels in a given image were thresholded to ground level.
4. Crop primary cilia sections out of each image in the image pair
5. Find the maximum intensity pixels from each scan line on both images
6. Interpolate the maximum intensity pixels found on primary cilia. The central maximum intensity pixel would correspond to the midpoint of primary cilia from the perspective of a given scan line
7. Spline fit the centerline to generate a line with $10^6$ pixels.
8. For each pixel found in step 6, find a orthogonal vector using two adjacent pixels found in step 7. These orthogonal vectors would provide cross sections that are locally orthogonal to primary cilia.
9. Calculate the length of the orthogonal vector covered by primary cilia structure.
10. Plot the calculated lengths on the y axis with the coordinates of the given scan line as the x axis of a graph.

**Figure 5-3** shows the various stages of the implementation of the algorithm explained earlier. Comparing data from confocal and STED images, we found the mean cross section of primary cilia as determined from apSTED images was consistently lower than confocal reported cross sections. As shown in **Figure 5-4**, mean cross sections determined from confocal data was ~290 nm as opposed to a mean size determined from apSTED to be ~175 nm. Furthermore, the cross sections reported from apSTED data was found to be closer to those reported in the literature using electron microscopy, further supporting the idea that apSTED estimated morphological dimensions were tighter than those determined from confocal microscopy alone.

**Figure 5-3. Sketch representing details of the development of image processing module that enabled extraction of morphometric features of primary cilia. (A) Extraction of primary cilia from the large scan area, cleaning and thresholding to enhance contrast (B) Determination of highest intensity pixel across each scan line. Highest intensity pixels**

**corresponded to the central maximum of primary cilia structures. (C) Spline fitting the central pixels to generate closely spaced pixels. These pixels were subsequently used to calculate orthogonal vectors, which in turn enabled calculation of cross sectional areas of primary cilia**

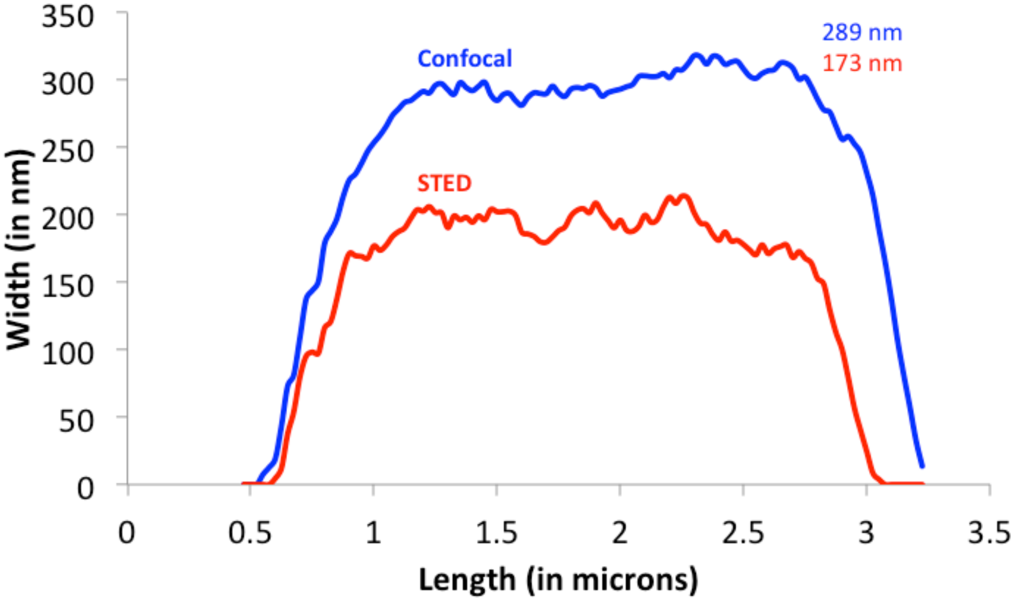

**Figure 5-4. Comparison of cross section areas of primary cilia as calculated by confocal microscopy and apSTED microscopy. apSTED systematically reported a lower estimate of these cross sections in close agreement to data reported by electron microscopy studies.**

We also quantified local structural variations in primary cilia using apSTED. Like the determination of cross sections, confocal image data was compared with STED data. We aimed to calculate local curvature on primary cilia on structural defects called local “kinks”. We determined the border of primary cilia and picked 3 points locally on the border. We developed a custom built script in Matlab to undertake a circular fit through 3 arbitrarily assigned spatial coordinates. Radii of these circle fits were estimated using Newton-Pratt least squares. Subsequently, we utilized this script to fit a circle through the points determined on the local “kinks” of primary cilia. The inverse of the radius of these circle fits provided an estimate for the local curvature of primary cilia “kinks”. As shown in **Figure 5-5**, there was a significant difference between "kink" curvatures calculated using the two modalities further underscoring the usefulness of the superresolution approach.

## 5.4 apSTED imaging of transition zone components of primary cilia

Structurally, transition zone is one of the most important components of primary cilia. Not only does it provide the necessary physical anchoring to the ciliary component but it also provides the necessary barrier differentiating the internal environment of primary cilia from the rest of the cytosolic materials in the cell. Various biochemical and electron microscopy studies have demonstrated the transition zone to be composed of myriad structural and functional protein complexes. Some of these complexes have been shown to be necessary structurally i.e. if they are knocked down, ciliogenesis is disrupted altogether. Other complexes play a more functional role, such as Tctn-2, disruption of which contributes to ciliopathies, such as MKS. We focused our attention on studying functional complexes such as Tctn-2 and Cep290.

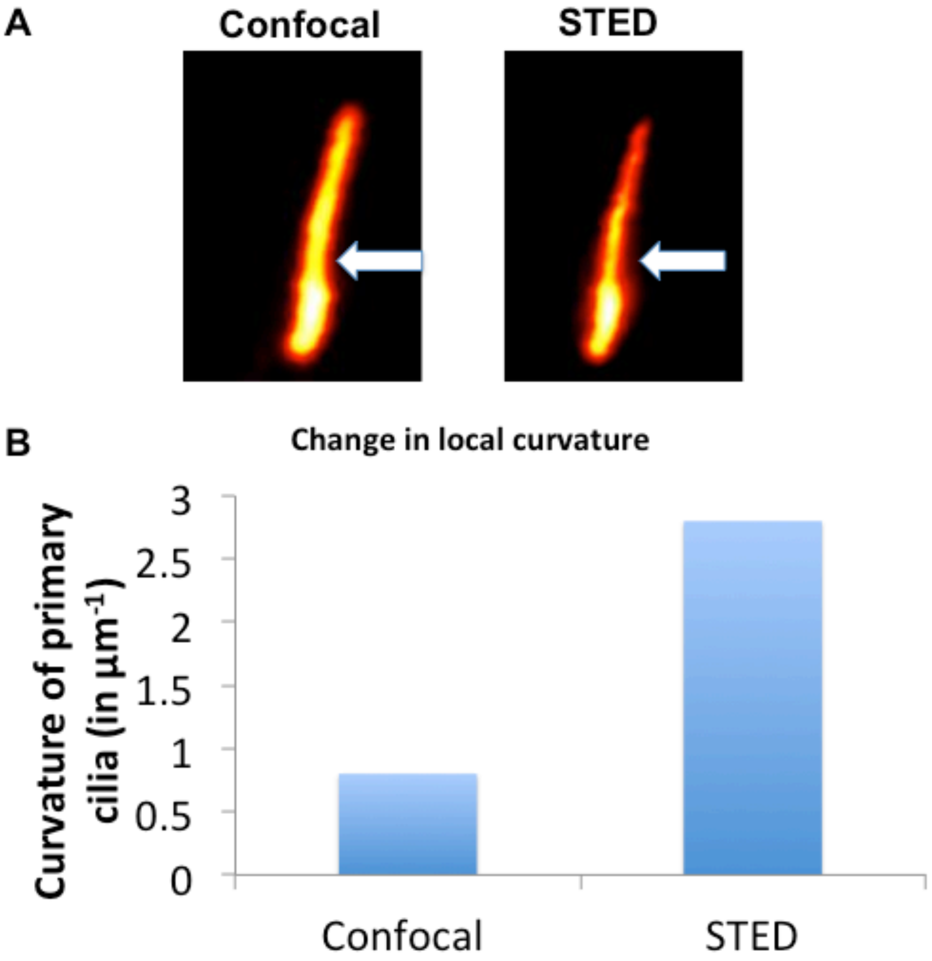

**Figure 5-5. (A) Image data set comparing confocal and STED images of local curvature of primary cilia. (B) Quantification of these images reveals significant differences in curvature as measured by the two techniques underscoring the advantages of using apSTED to quantify morphometric parameters of primary cilia.**

The existence of a family of transmembrane proteins, Tectonic, was identified in 2006[2]. Several members of the family have been identified, such as Tctn-1, Tctn-2, and Tctn-3, to play significant roles in maintenance of structural integrity of primary cilia, as a part of the machinery that transduces Hh signaling pathway, and also contributing to ciliopathies, such as MKS. In particular, we focused on studying Tctn-2.

### 5.4.1 apSTED imaging

Sample coverslips were mounted on microscope slides using PBS as mounting media. Proper positioning of the cover slips on the slide was assured by sticking them using nail polish. Samples were briefly imaged using epi-fluorescence, following the protocol described in chapter 3, to validate adequate labeling of Tctn-2. Subsequently, the sample was placed on the apSTED sample holder.

Large area confocal scans were performed to identify the location of Tctn-2 on samples before switching to apSTED mode. As shown in **Figure 5-6**, STED reveals a two-dot distribution of Tctn-2. Because a thin z-section of the image, the two-dot distribution represents a cross-section of the Tctn-2 proteins in a thin slice of the z-focal plane. That is, it is likely a projection view of a ring-shaped structure in this plane. This supports the hypothesis of cylindrical distribution of Tctn-2, as a transmembrane protein located on the transition zone membrane.

We collected line scan profiles of Tctn-2 particles imaged using both the confocal and apSTED modes. As shown in **Figure 5-7**, the line profile allowed quantification of the distance between specific intensity peaks corresponding to the center of Tctn-2 particle. Such line scans provided two important pieces of information. The first and the most important piece of information was the elucidation of the underlying structure of Tctn-2. This is the first set of unequivocal far-field fluorescence based images that allow us to visualize Tctn-2 structure to this level of detail. The ~150 nm inter-peak distribution provides first order clues about the spatial distribution of Tctn-2 within the transition zone. Tctn-2 is a transmembrane protein. Therefore, in conjunction with the diameter of the Tctn-2 distribution, the inter-peak distance provides upper bound for the size scale of transition zone. The second piece of information is the fact that it underscores the applicability of apSTED not only in studying primary cilia components but, more broadly, to study myriad problems in macromolecular structural biology, heretofore not amenable to prevailing imaging tools.

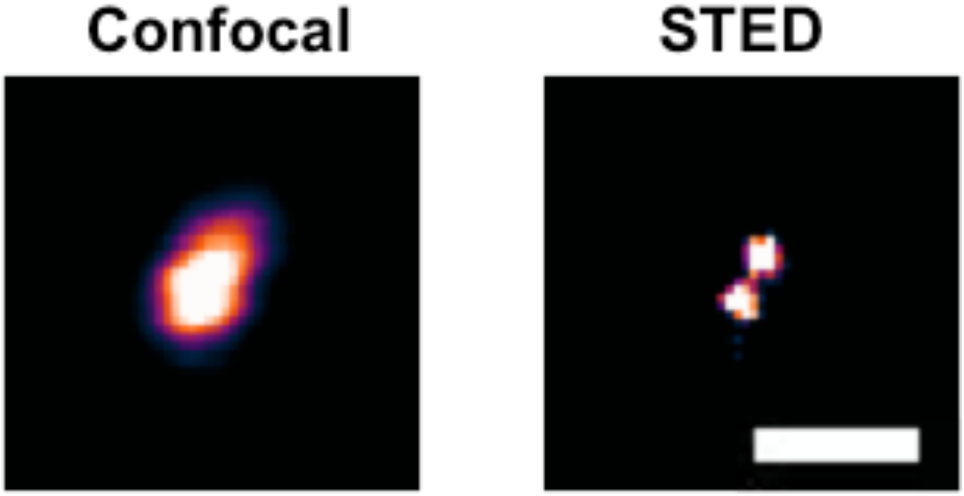

**Figure 5-6. Side by side comparison of confocal and STED images for Tctn-2 on Hff1 cells. The two-dot distribution of Tctn-2 supports the hypothesized amorphous cylindrical distribution of Tctn-2 within the transition zone. Scale bar: 500 nm.**

Next, we focused our attention on Cep290. Cep290 plays an important structural and functional role in mammalian primary cilia. In particular, its role has been highlighted in complex disorders, such as NPHP, MKS, and JBTS. It has also been highlighted as a part of the MKS-JBTS complex. In terms of structural role, in Chlymidomonas reinhardtii, it has been shown to be necessary for the formation of Y-links. Y-links are structural elements that hold the axonemal micro-tubule doublets in place by anchoring them to the pericilliary membrane.

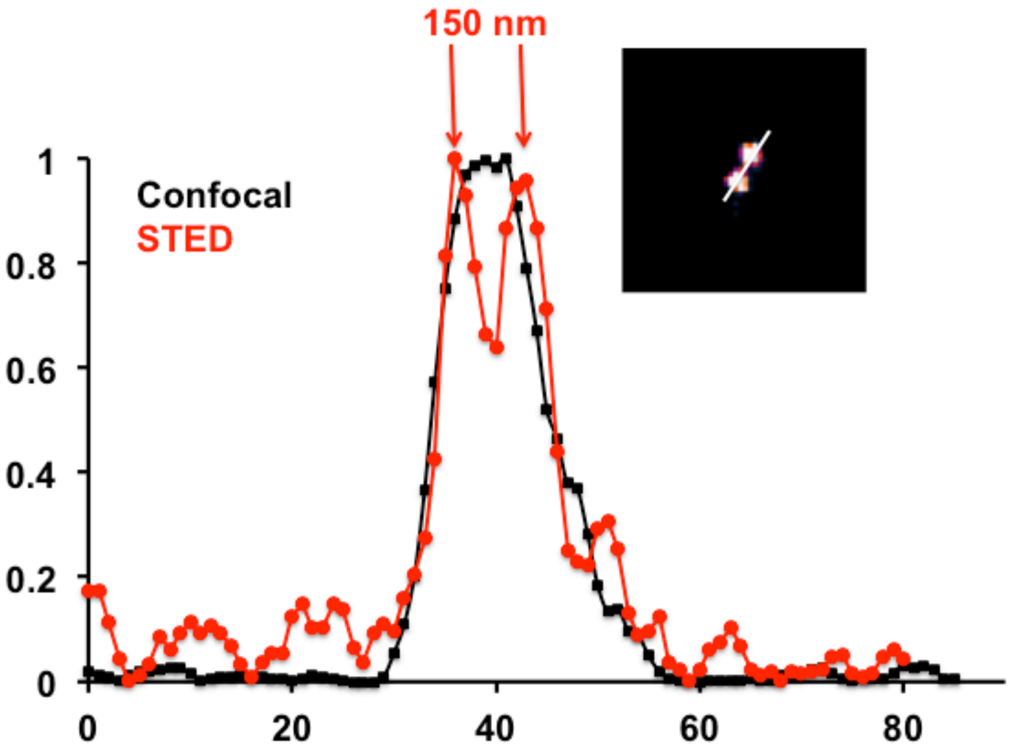

**Figure 5-7. Line scan profile of a representative confocal and STED scan of Tctn-2 on Hff1 cells. As the confocal profile in black indicates, it could not decipher the underlying structure of Tctn-2. On the other hand, as the STED profile in red indicates, it could clearly elucidate two independent peaks, a level of detail completely beyond the scope of conventional confocal microscopy.**

In order to study Cep290, cell cultures were prepared as explained in the previous section. However, the fixation/immunostaining protocol was modified. The following is the protocol that was used for Cep290:

#### ***5.4.1.1 Fixation/immunostaining protocol***

1. After serum deprivation either for 24 or 48 hours, cells were fixed using methanol chilled at -20 C for 5 minutes.

2. Samples were then washed thrice with Phosphate Buffer Saline (PBS)

3. Cells were incubated in -20°C methanol for 5 minutes and subsequently washed with PBS (3x)

4. PBS washes were followed up with permeabilization with 0.2% PBS-Triton (PBST) for 10 min.

5. After permeabilization, samples were blocked using PBST containing 2% Bovine Serum Albumin (BSA) and 1% normal donkey serum, at room temperature for 1 hour.

6. Cells were incubated with primary antibody; mouse monoclonal antibody to Tctn2 (ab119091, Abcam), in the blocking solution overnight at 4 C

7. Next day, cover slips were washed with PBST (3x) before being incubated with donkey anti-rabbit Alexa Fluor 488 antibody diluted 1:2000 in the same blocking solution at room temperature for an hour

8. Post secondary antibody incubation, the samples were washed with PBST

(3x)

As shown in **Figure 5-8**, similar to the approach with Tctn-2 and Ac-Tub imaging previously, we did side-by-side comparisons of confocal and STED image data for Cep290. apSTED provided better resolution and a tighter estimate of the size of Cep290 distribution. Given the finite resolution of our apSTED system, ~50 nm, we believe any structural variation in Cep290 distribution to be at a length scale smaller than that figure.

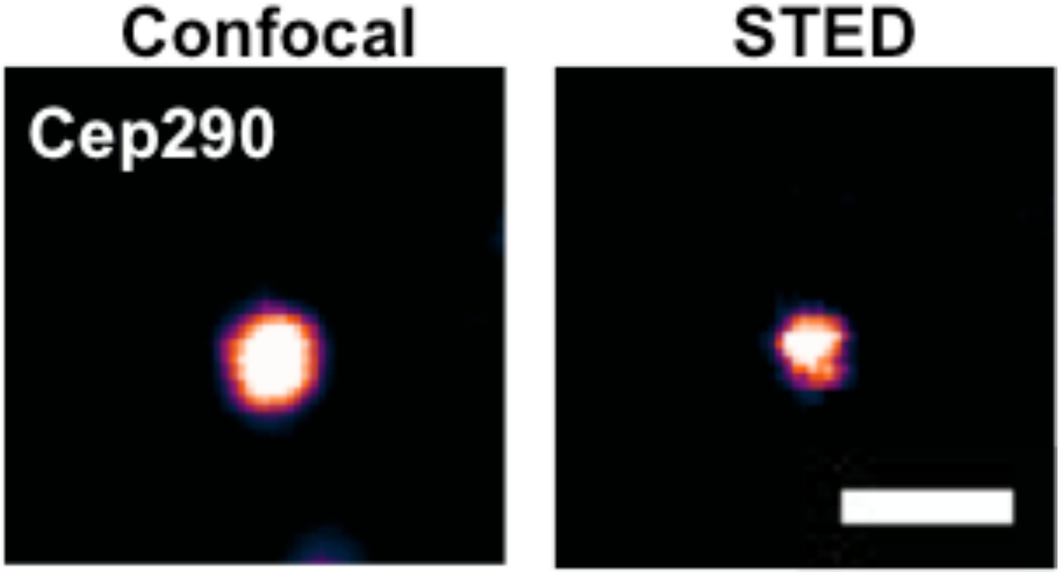

**Figure 5-8. apSTED imaging of Cep290 in the transition zone of primary cilia. A comparison with confocal underscores the tighter estimate that one gets imaging Cep290 using apSTED. Scale bar: 500 nm.**

Next, we quantified both the Cep290 and Tctn-2 data collected using apSTED. In particular we measured the diameter of the distribution of both the macromolecular complexes. We did a circular fit to the boundary of each

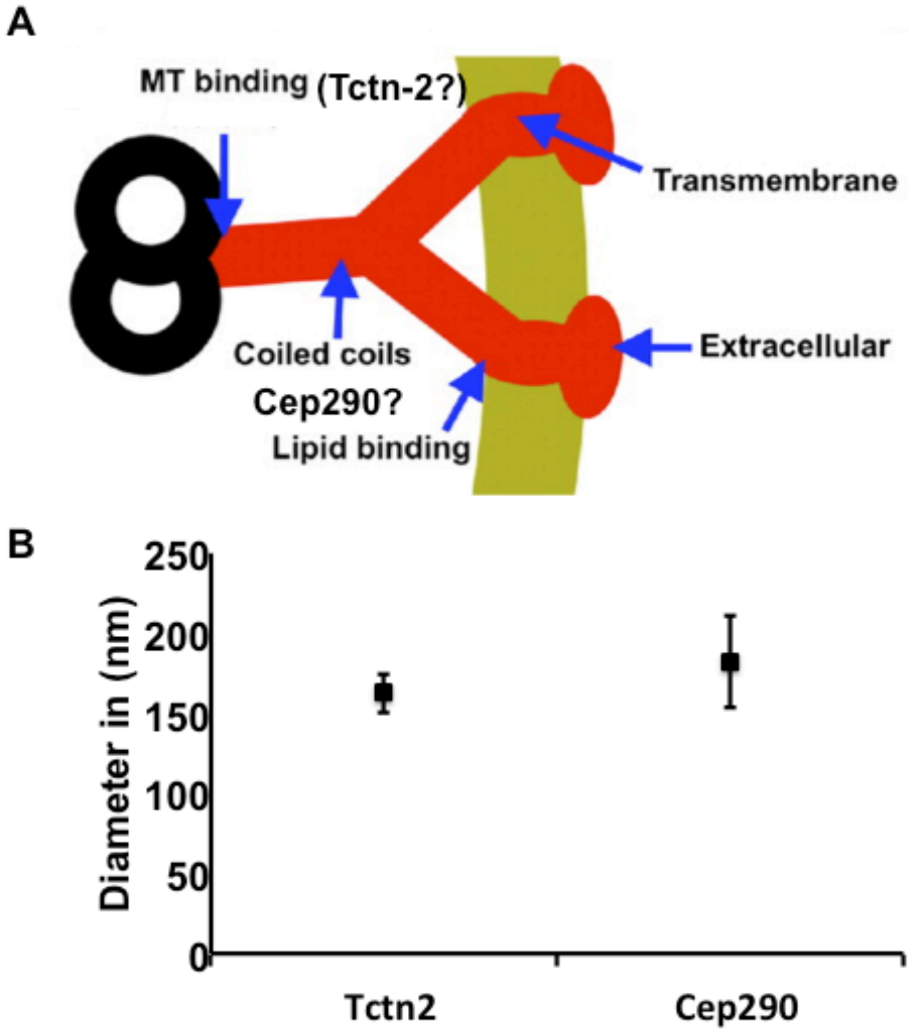

**Figure 5-9. (A) Schematic of a model proposing the structural composition of Y-links on primary cilia. The model schematic was originally published in this study[3]. (B) Quantification of diameters of Tctn-2 and Cep290 estimated using apSTED images. It provides the first set of visual evidence to study the model proposed in (A).**

structure and estimated the diameter of the fit. Our data suggests the diameter of Tctn-2 distribution, ~160 nm, to be smaller ($p<0.05$) than that of Cep290, ~180 nm. Taken together, our data helps verify a recent model of Y-link structure proposed by the Reiter group[3]. According to the proposed model, shown in **Figure 5-9**, Cep290 and Tctn-2 were hypothesized to be a part of the Y-link at the transition zone of primary cilia. Given the larger diameter of Cep290, as estimated from our data, as compared to Tctn-2, we believe this is the first set of visual evidence that indicates that Cep290 may be structurally present to the "outside" of Tctn-2.

In summary, we demonstrate the resolution enhancement achieved on biologically relevant samples using apSTED nanoscopy. We developed image-processing tools enabling high-fidelity quantification of apSTED data, enabling us to tease out structural information of axonemal structure of primary cilia. Furthermore, we studied components of the transition zone, namely, Tctn-2 and Cep290, and verified a model of structural composition of Y-links of primary cilia using our imaging based assay.

## Reference:

1. Felgner, H., Frank, R. & Schliwa, M. Flexural rigidity of microtubules measured with the use of optical tweezers. *J. Cell. Sci.* **109 ( Pt 2)**, 509–516 (1996).
2. Reiter, J. F. Tectonic, a novel regulator of the Hedgehog pathway required for both activation and inhibition. *Genes & Development* **20**, 22–27 (2006).
3. Garcia-Gonzalo, F. R. F. & Reiter, J. F. J. Scoring a backstage pass: Mechanisms of ciliogenesis and ciliary access. *The Journal of Cell Biology* **197**, 697–709 (2012).

# 6 Summary and future work

This project benefited largely from development of a superresolution apSTED nanoscopy system. During our development of the system, we faced many vexing challenges, which while affect optical systems in general get amplified at the resolution scale afforded by STED. For example, in order to keep the two lasers aligned over appreciable lengths of time, we had to reverse engineer the design of our lab to include extra air-conditioning to maintain the temperature with minimal to no fluctuations in temperature. Given the resolution regime at which we were operating, ~1°C variations in temperature resulted in misalignment of the lasers, hampering rapid progress on the system.

Our first major achievement was overcoming this and several other subtle challenges in order to successfully implement a STED system. We were able to develop STED nanoscopy system affording a resolution of ~50 nm on biological samples. We were able to implement apSTED enhancements that enabled circumventing challenges of photobleaching reducing photobleaching levels from ~80% to ~10%. We engineered several optical alignment fine-tuning strategies for high-speed alignment of a STED system. All software used for control, data collection, image processing, and quantification, along with data analyses were custom-built by our lab. Note: In a few exceptional cases, ImageJ was used for image visualization and processing.

The biological system of interest to us was primary cilia, a hair-like appendage emanating from most mammalian cell types. As described in chapter 3, we developed a series of imaging based assays to study primary cilia on Hff1 cells from myriad different perspectives. Specifically, we looked at mesoscale aspects of primary cilia through imaging Ac-Tub and pericentrin, providing us with a tool to probe morphological parameters of primary cilia. We studied the molecular components of primary cilia structure, such as NPHP4, Tctn2, and Cep290. We probed molecular components of the cilium that participate in transduction and activation of Hh signaling pathway, such as Ptch1 and Smo. Undertaking perturbation study using a Smo agonist, SAG, we validated the functional status of primary cilia.

In chapter 4, following up on recent work highlighting the role of primary cilia on embryonic stem cells, we studied primary cilia on hiPSCs. Using a combination of imaging based assays and biochemical analysis, our group was the first to systematically study and report the presence of primary cilia on hiPSCs. Our data confirmed not only structural presence of primary cilia on hiPSCs but also their functional status. We highlight several morphological differences between primary cilia occurring on hiPSCs as opposed to those on somatic cells, such as, a decrease in length and an increase in curvature of primary cilia occurring as a resulting of cellular reprogramming. These differences may be indicative of differences in modulation and perception of external signals by hiPSCs.

The applicability of apSTED imaging in studying morphological details of primary cilia structure was detailed in chapter 5. We reported subtle differences in primary cilia structure that were deciphered based on apSTED imaging, which were beyond the ability of any diffraction limited imaging system. Our data indicate estimates of morphological parameters of primary cilia using apSTED system to be closer to estimates offered by electron microscopy. Features such as local curvatures on primary cilia, which sometimes misrepresented by confocal microscopy, were amenable to quantification using apSTED imaging. Furthermore, we probed the structural detail of Tctn2 distribution within the transition zone. Our data support the hypothesis of a ring shaped distribution of Tctn2 at the transition zone.

## 6.1 Potential future work

The tighter estimate of morphological parameters of primary cilia afforded by STED makes it possible to model primary cilia behavior with a much higher accuracy. Primary cilia models, proposed thus far, have relied on data from EM and have not been successful at capturing dynamics of variations in primary cilia morphology. This technique provides a tool to enable this research.

Furthermore, here we have looked at components of transition zone from a structural perspective. apSTED could also be used to undertake imaging assays to study the dynamics of intraflagellar transport, the mechanism that carries material in and out of the ciliary component. In particular, one could knock down transition zone components studied here to study dynamics of corresponding changes resulting on intraflagellar transport.

Another avenue worth exploring is to expand the current apSTED system to two colors. This would enable (co)localization based studies. Coupled with the superior resolution, being able to do multi-color imaging would make apSTED universally appealing to any biology lab.

The STED system described here could also benefit if implemented in a multi-focal configuration. The parallelization achieved by using, for instance, 4 beamlets instead of a single beam would increase the imaging speed even further enabling studies of biological systems with faster dynamics.